HYBRID AND SMART GRID WIRELESS NETWORKS: CAPACITY AND OPTIMIZATION

by

XIN WANG

Presented to the Faculty of the Graduate School of
The University of Texas at Arlington in Partial Fulfillment
of the Requirements
for the Degree of

DOCTOR OF PHILOSOPHY

THE UNIVERSITY OF TEXAS AT ARLINGTON

May 2014

To my dear family

Acknowledgements

Firstmost, my deepest gratitude goes to my supervising professor Dr. Qilian Liang, who is invaluable for constantly motivating me to explore my capability of doing research, inspiring me to provide innovative solutions, and training me to possess cooperation skills. Dr. Qilian Liang is such a self-disciplined, diligent and excellent researcher who was and will always lead my way through my life. His mentorship is paramount in providing a well rounded experience consistent my long-term career goals. I could not have imagined a better supervisor and mentor for my Ph.D study.

Besides my supervisor, I would like to extend my appreciation to the rest of the thesis defense committee: Dr. Jonathan Bredow, Dr. Wei-Jen Lee, Dr. Ioannis D. Schizas, Dr. Saibun Tjuatja and Dr. David A. Wetz for their interests in my research and for taking time to serve in my thesis defense committee.

I also thank my group members from the Wireless Communications and Networking (WCN) Laboratory. I learned a lot from this group about life, research, how to tackle new problems and how to develop techniques to solve them.

Meanwhile, this work was supported in part by U.S. National Science Foundation under Grants CNS-1247848, CNS-1116749, CNS-0964713, and U.S. Office of Naval Research under Grants N00014-13-1-0043, N00014-11-1-0865, N00014-11-1-0071.

Last but not least, I would like to thank my family who have been extremely understanding and supportive of my studies. I feel very luck to have a family that share my enthusiasm for academic pursuits.

April 14, 2014

Abstract

HYBRID AND SMART GRID WIRELESS NETWORKS:
CAPACITY AND OPTIMIZATION

Xin Wang, Ph.D.

The University of Texas at Arlington, 2014

Supervising Professor: Qilian Liang

Hybrid wireless network is a combination of ad hoc network and cellular network. A key question arising in such hybrid wireless networks is what is the per-node data transmission limit of the hybrid wireless network over general fading channels and how the throughput capacity varies with different network setup. To our best knowledge, our research is the first piece of work in literature to take up this challenge. To achieve the maximum per-node throughput, an opportunistic communication strategy together with successive interference cancelation (SIC) technique is proposed in this dissertation. The scaling laws for the throughput capacity over both slow fading channels and fast fading channel are derived, and the closed-form analytical expressions for the outage throughput capacity and ergodic throughput capacity are provided. Our research applies an information theoretic approach to determine the threshold of the data transmission rate in hybrid wireless network.

Wireless sensor and actuator networks (WSANs) are applied into microgrid to stabilize the power supply in smart grid. In this dissertation, several sensor selection schemes are heuristically proposed to improve the voltage measurement performance

and prolong the sensor network lifetime. First, aiming to accurately monitor the real-time voltage level, we propose an opportunistic sensor selection scheme under equal power allocation and investigate the asymptotic behaviors of the voltage measurement performance. We further address the sensor selection scheme under optimal power allocation. Besides, we present the studies on improving the power efficiency with the aid of voltage sensor selection.

As a paradigm of the incoming smart grid, vehicle-to-grid (V2G) has been proposed as a solution to increase the adoption rate of plug-in hybrid electric vehicles (PHEVs). In this dissertation, we investigate the energy management strategies for PHEVs via bidirectional V2G. We first follow a cost-conscious approach from the PHEV owner point of view. We prove that a state-independent four-threshold feedback policy is optimal for PHEV battery charging/discharging based on stochastic inventory theory. Further, from the distribution system operator point view, we aim to shave the peak load and flatten the overall load profile. To this end, we propose an optimal PHEV charging scheme and derive a reminiscent of "water-filling" solution.

Finally, based on the present researches on the capacity and optimization of hybrid and smart grid wireless networks, we propose two future research directions. First, we propose the future works about the throughput capacity of hybrid wireless networks with hexagon cell structure and Poisson Point Process (PPP) distributed base station. Second, we discuss the future research topic on the throughput capacity of cooperative-diversity networks over fading channels.

Table of Contents

List of Illustrations

List of Tables

Chapter 1

Introduction

1.1 Introduction to the Hybrid Wireless Networks

Radio waves do have a limited range, no matter which technologies are adopted. In terms of network topology, two basic types of wireless network are available: infrastructure-based *cellular network* and infrastructureless *ad hoc network*. Cellular networks are probably the most common way of overcoming the limited range problem. The user equipments (UEs) communicate directly with the base stations. The base stations themselves are again connected to a network which can also be connected to other networks like the internet. Wireless networks without support from the fixed infrastructure are known as ad hoc networks. Since ad hoc networks are linking devices like computers or mobile phones directly without a base station or access point, the data is forwarded from the source to the destination via a multi-hop fashion. To overcome the limited range problem, devices can not only do their own communication but also serve as a relay-station and forward other messages.

Hybrid wireless networks combine these above two technologies, as shown in Figure 1.1. Within hybrid wireless network, a cellular network can be extended into regions where no base station is reachable; meanwhile, the base stations can provide access to other networks like the internet. Therefore, the hybrid wireless network takes advantage of both the long distance communication property of the cellular network and the peer-to-peer communication property of the ad hoc network.

In wireless networks, the nodes exchange information over a common wireless channel. Under different traffic scenarios and different constraints, e.g., bandwidth

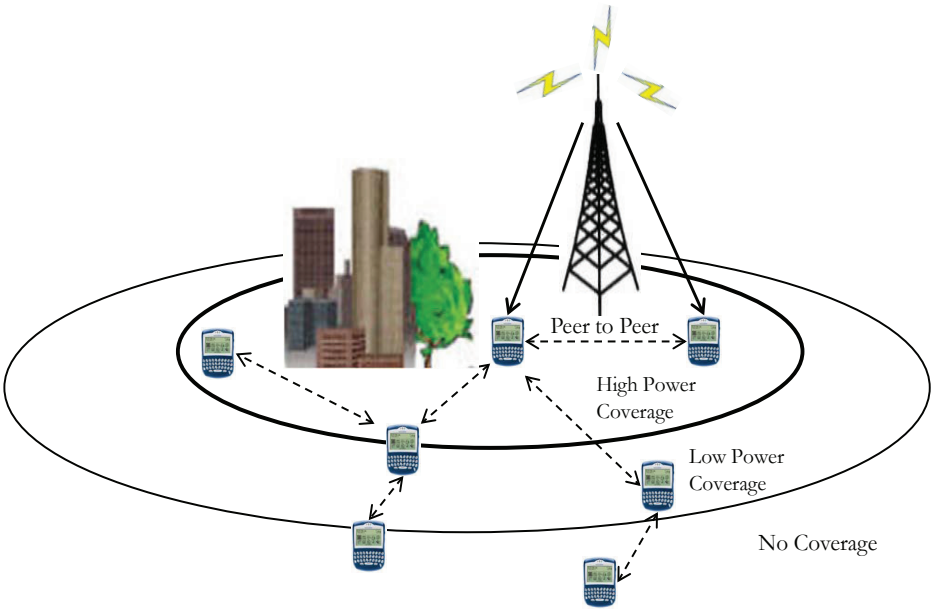

Figure 1.1. Hybrid wireless networks.

and power, the amount of data exchanged among these nodes may vary. A key question that arises in such hybrid wireless networks is what is the per-node data transmission limit of the hybrid wireless network over general fading channels and how the throughput capacity varies with different network setup. In the literature, the seminal paper by Gupta and Kumar [2] initiated the study of the scaling laws in large ad-hoc wireless networks. Their by-now-new model has illustrated that, if the nodes are placed optimally, the per-node capacity decreases at $\Theta(1/\sqrt{n})$ as n tends to infinity. On the other hand, if the nodes are randomly located, the per-node capacity decreases at $\Theta(1/\sqrt{n \log n})$. Nevertheless, with a more general information theory setting, it was later proved in [3] that a rate higher than $\Theta(1/\sqrt{n})$ is potentially achievable. Subsequently, in [4], the authors have applied the percolation theory and provided a lower bound of $1/\sqrt{n}$ for the per-node capacity of a network with randomly placed nodes, hence closing the gap in the capacity of wireless networks. Note that [5] has proved the per-node throughput of mobile ad-hoc networks is bounded

by a constant even as the number of nodes n increases. The capacity of a hybrid wireless network has also been widely studied in the literature, for example [6]-[15] and references therein. In [6], the benefit of the infrastructure is shown to be dependent on the number of base station relative to the number of wireless nodes and, for a two-dimensional hybrid network with b stations, the maximum per-node capacity scales as $\Theta(b/n)$ if the number of base stations increases faster than $\sqrt{n}$. Similarly, in [7], it has been proved that, if $b = \omega(\sqrt{n})$, the maximum per-node capacity of $\Omega(min(b/n, 1/\log b))$ is achievable by delivering data through the wired infrastructure. Otherwise, the percolation highway [4] must be used in order to achieve the maximum capacity. Kozat and Tassiulas [8] further study the throughput capacity of hybrid wireless networks where both the ad-hoc nodes and the base stations are randomly distributed. They prove that the per-node throughput capacity is $\Theta(1/\log n)$ if the number of base stations linearly scales with the number of nodes, which means the network cannot scale. Similar results are also presented in [9]. The authors of [10] focus on the throughput capacity of hybrid wireless networks where the nodes are randomly distributed and the base stations are arbitrarily placed. Their researches demonstrate that the per-node throughput capacity depends on the number of base stations, but the network still cannot scale.

It is worth mentioning that a very important issue in practical wireless networks, and unmodeled in [6]-[15], is the presence of multi-path fading. In a wireless network, due to the physical environment, the electromagnetic waves travel to the receivers along a multitude of paths, encountering delays and suffering gains which vary with time [16] [103]. *However, to our best knowledge, there have not been any studies on the data transmission limit of hybrid wireless networks over fading channels.* In this study, to analyze the effect of fading on the hybrid wireless network, one commonly used fading models, i.e., Nakagami-m fading, is specifically examined. Nakagami-m

distribution spans via the m parameter the widest range of amount of fading (AF) among all the multipath distributions. For instance, it includes one-sided Gaussian distribution ($m = 1/2$) and the Rayleigh distribution ($m = 1$) as special cases. In the limit, as m approaches infinity, the Nakagami-m fading channel converges to the non-fading additive white Gaussian noise (AWGN) channel. The Nakagami-m distribution can also closely approximate the Nakagami-n (Rician) distribution with the parameter mapping [18]. It is thus straightforward to extend our work to the general fading scenarios.

Further, unlike the previous studies, in this work we apply an optimal [1] multiple access technique to increase the network throughput. Specifically, when a node is scheduled for transmission, a set of nodes from the same cell are selected to transmit simultaneously with the scheduled source, as long as such transmissions do not impair the achievable transmission rate of the scheduled source. These nodes are referred to as opportunistic sources. All these sources share the entire bandwidth. However, rather than treating the interference from other nodes as noise, the receiver deploys a successive interference cancelation (SIC) technique, as detailed in [19] [20]. That is, after one node is decoded, its signal is stripped away from the aggregate received signal before the next node is decoded. Similar to [21] [22] [23], our key idea behind this decoding scheme is that we believe the previous physical model used by many literatures, for example [2] [6], is somewhat strict. In particular, these models treat the signals received from the nodes other than the transmitter as interferences. Based on this assumption, long range point-to-point communication between nodes is not preferable. The reasonable strategy is then to resort to the multi-hop scheme to confine the communications to nearest neighbors and rely on a spatial reuse to maximize

[1] The "optimality" is mainly defined from the sum-rate perspective. The fairness and efficiency of such strategy go beyond the scope of this dissertation.

the number of simultaneous transmission. However, we take a weak restriction allowing the nodes to transmit data directly to their destinations. We schedule a set of opportunistic nodes to transmit simultaneously and, with the aid of SIC decoding technique, the interference from these nodes becomes valuable information [24]-[26].

1.2 Introduction to Sensor Selection Schemes in Smart Grid

The past few years have witnessed a revolutionary change from ordinary electrical grid to smart grid [31]. Currently, supplying isolated locations with electricity comes with an increased cost to the distributed network operators (DNOs) since the majority of the energy that is destined for customers is wasted in the form of heat before any useful energy reaches the consumer [32]. In smart grid, distributed energy resources (DERs), such as wind turbines and solar panels, provide a cheaper and more efficient solution that can deliver the energy from points closer to the consumer than DNO's centralized power grid [33]. To introduce DER technology, the distribution networks are divided into *microgrids*, which are managed by the autonomous intelligent control center (ICC), instead of DNO control center (See Figure 1.2).

Maintaining adequate operating voltage at all the customer delivery points is very critical to the microgrid system. Voltage regulation in traditional distribution system is mainly provided by onload tap changer (OLTC), line regulators and switched shunt capacitors at the substations and feeders, on the assumption that the current always flows from the transmission to high voltage/middle voltage (HV/MV) substations and then to the MV feeders. However, the introduction of DERs makes this assumption no longer valid [34]. DERs alters the flows which, in turn, alters feeder voltage profiles and affects the voltage regulation in distributed systems [35].

In literature, there have been some studies on coordinating the DERs and regulating the voltage level in smart grid [36]-[41]. For instance, to coordinate multiple

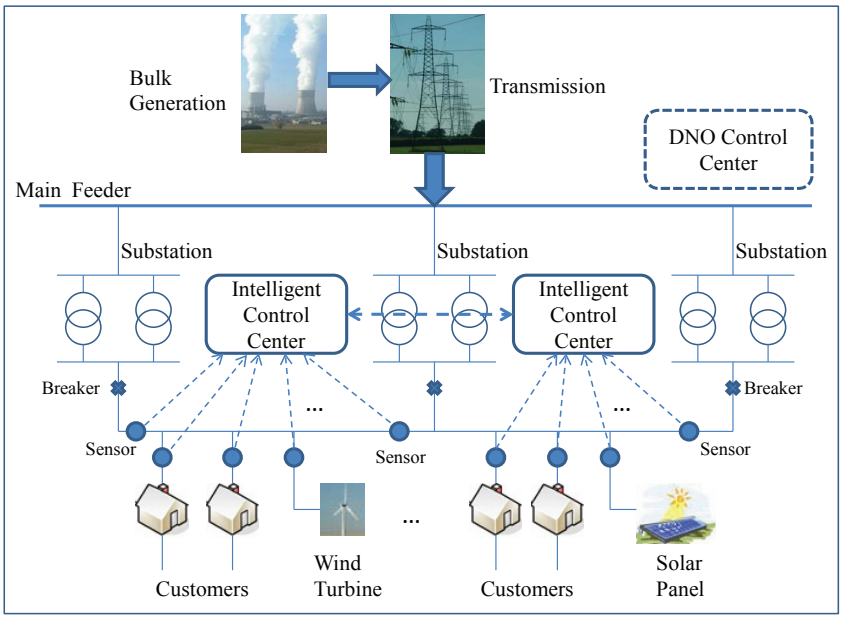

Figure 1.2. Distributed energy resources (DERs) introduced to microgrid.

DERs in voltage control, [36] considered the sparseness of the voltage deviation and proposed a sample-contention mechanism using WiMAX to prioritize the voltage state reports. Note that in [37], the communication topology is designed for distributed voltage control, where the communication delay is ignored. Also, to stabilize the voltage of DERs in microgrid, the application of cyber physics systems (CPSs) is introduced and the decentralized scheduling in the MAC layer is investigated in [38]-[40]. Unlike these previous studies, to accurately monitor the real-time voltage level and coordinate DERs with the traditional voltage regulators, we focus on the communication system design from the physical layer perspective. In terms of the communication system design, the wired communication based on power line communication (PLC) is apparently a suitable candidate (the nature of the power grid); however, in microgrid, wireless communication is more preferred by many application scenarios [42], such as: 1) when many parameters in DERs need to be monitored,

PLC can result in a costly and complicated system architecture; 2) PLC cannot easily bypass transformers in a power distribution network; 3) wired communications cannot provide peer-to-peer communications among electric devices in a flexible manner. Wireless sensor and actuator networks (WSANs), characterized by monitoring, automatic control and two way communications, could effectively monitor the real-time voltage statement, detect load fluctuation and track power flow [43] [44]. Each voltage sensor deployed in the microgrid processes its individual voltage measurement and transmits the result to the ICC, which could immediately respond to the voltage fluctuation by turning on/off the related DERs and voltage regulators to stabilize the power supply and thus avoid significant voltage perturbations.[2]

Note that one important property of the voltage sensors is their stringent power constraint. Such voltage sensors have only small-size batteries whose replacement can be costly if not impossible. If a sensor remains active continuously, its energy will be depleted quickly leading to its death [45]. Therefore, to prolong the network lifetime, the voltage sensors need to alternate between being active and sleeping. The sensor selection problem has already arisen in various applications, including sensor placement for structures [46], sequential estimation [47], target tracking [48], single mission sensor selection scheme [49] [50] and multiple mission sensor selection schemes [51]. The study of [52] investigated the full sensing coverage of the field by identifying the appropriate sensors and turning off the redundant sensors. A survey of sensor selection schemes in wireless sensor network is summarized in [45]. *However, to our best knowledge, there have not been any specific studies employing the sensor*

[2]A general recommendation for voltage regulation is a minimum time delay of 15 sec. This time-delay setting covers the vast majority of temporary voltage swings due to equipment starting, cold-load pickup, etc. It also has another important benefit when attempting to coordinate two or more voltage regulators in series along the line.

selection schemes in microgrid to regulate the voltage level and stabilize the power supply. To achieve proper voltage regulation, in this dissertation, several heuristic sensor selection schemes are proposed in the context of voltage regulation and the following three fundamental issues serve as the criteria for sensor selection.

- *Voltage Estimation Accuracy*: Voltage estimation accuracy determines if the control center can perform reasonable operations to regulate the voltage, based on the real-time voltage level information collected from the monitoring sensors;
- *Power Efficiency*: To prolong the lifetime the WSANs, the power consumption should be minimized;
- *Transmission Rate*: The wireless communication link should transmit the voltage measurements to the control center with negligible error in a real-time manner.

1.3 Introduction to Energy Management for Plug-in Hybrid Electric Vehicles

With recent concerns about global warming and petroleum-based energy shortages, the number of hybrid electric vehicles (PHEVs) and fully electrical vehicles (EVs) is expected to rapidly increase in the coming years [65]. The energy consumed by EVs comes entirely from the electricity grid while for PHEVs the energy can come both from the electricity grid and other sources. Both PHEVs and EVs [3] can assist in shifting the personal transportation sector away from fossil fuels, and become an integral part of the overall smart grid concept.

On the one hand, the mass adoption of PHEVs in the future is not without its challenges: the PHEV charging is a relatively large load in the electricity grid, and unmanaged PHEV charging can increase the electricity load, inevitably amplifying the peak load [66]. It has been estimated that the total charging load of the PHEVs

[3]PHEVs and EVs will both be referred to as PHEVs in the remainder of this dissertation.

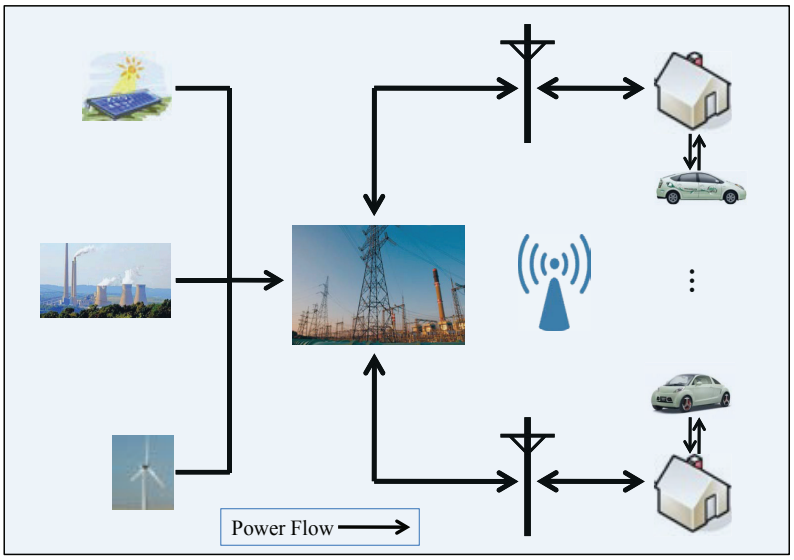

Figure 1.3. A schematic illustration of bidirectional V2G energy flow.

in U.S. can reach 18% of the U.S. summer peak at the PHEV penetration level of 30% [67]. Further, the PHEVs may increase the load uncertainties, overload the distribution circuits elements, e.g., transformers [68], and lead to voltage regulation violations [69]. On the other hand, the PHEVs can provide energy back to the power grid by discharging the battery, which is known as vehicle-to-grid (V2G) [70]. Various V2G concepts have been studied in [70]-[73], where the significant profits can be made by offering V2G services. Basically, the power flow in V2G can be both unidirectional and bidirectional. Although it is anticipated that the unidirectional V2G will be implemented first, the unidirectional V2G is limited to participation in regulation and reserves markets and it has been shown to have lower capacities in those markets [73]. Therefore, the focus of this section lies on optimizing the *bidirectional* V2G energy flow: from the grid to the PHEV battery and from the PHEV battery to the grid, as schematically shown in the Figure 1.3.

As is known, an intelligent energy management scheme can optimally schedule the PHEV charging and discharging patterns such that the load profile of the electrical grid can be effectively shaped. The essential principle in intelligent energy scheduling is to reshape the load profile by charging the PHEV from the grid when the demand is low and discharging the PHEV when the demand is high. In literature, there have been some existing studies on the PHEV energy management [74]-[87]. For instance, [74] introduced the PHEV charging model based on real-time price information; while, [75] proposed an optimal store-carry-and-deliver energy management strategy for PHEV and further integrated the time-of-use (TOU) pricing policy. Sortomme *et al.* proposed an unidirectional regulation at the aggregator, in which several smart charging algorithms are employed to set the point about which the rate of charge varies [66]. The comparison between centralized charging strategy and local charging strategy is discussed in [76]. The authors of [77] proposed a decentralized algorithm for optimally scheduling PHEV charging, which is distributed and thus requires low computation capacity. Some mathematical optimization approaches are also considered in the literature. The study of [79] employs the linear programming model to respond to the real-time pricing policy. A mathematical optimization approach based on quadratic programming is presented in [80], of which the aim is to minimize the energy losses and maximize the grid load factor. Distributed algorithms based on dual decomposition theory are proposed in [81] [82]. Note that [83] introduced the tool of game theory to solve the decentralized charging control problems in terms of large-population of PHEVs. It proved that, under certain mild conditions, the large-population charging game converges to a unique Nash equilibrium which is either globally optimal or nearly globally optimal. The control schemes for charging PHEV based on queuing theory are considered in [85] [86]. A comparison of the intelligent charging algorithms for PHEVs to reduce the peak load and demand variability

is summarized in [87]. However, the implementation of these above-mentioned intelligent energy management techniques remains relatively complicated and expensive. *Furthermore, to the best of the authors' knowledge, it is still a significant open question considering the bidirectional energy flow, real-time electricity price and realistic PHEV battery models.*

Motivated by this, in this study, we propose an optimal energy management strategy for PHEV charging and discharging. Our contributions are as follows.

- We formulate a realistic PHEV battery model which integrates the battery charging and discharging capacity, the battery charging and discharging efficiency, the battery aging/wear cost and the battery self-discharging effect.
- From the PHEV owner point of view, we propose a cost-conscious approach based on dynamic programming. In order to minimize the daily energy cost, we formulate the PHEV energy management problem through dynamic programming. Further, in order to reduce the computational complexity, we prove that a state-independent four-threshold (*s, S, s', S'*) feedback policy is optimal for PHEV energy management.
- From the distribution system operator point of view, we present an optimal PHEV charging scheme to shave the peak load and flatten the overall load profile. A reminiscent of "water-filling" solution is derived for the PHEV energy management in this scenario.

The remainder of this dissertation is organized as follows. In Chapter 2, we investigate the theoretical per-node transmission limit of hybrid wireless networks over fading channels. The voltage regulation issue in microgrid is studies in Chapter 3, in which we apply the wireless sensor and actuator networks (WSANs) to accurately monitor the real-time voltage level and coordinate the distributed energy resources (DERs) with the traditional voltage regulators. In Chapter 4, we explore the energy

management strategies for plug-in hybrid electric vehicles (PHEVs) via bidirectional vehicle-to-grid (V2G). Finally, we propose some future research topics in Chapter 5.

Chapter 2

On the Throughput Capacity and Performance Analysis of Hybrid Wireless Networks over Fading Channels

In this chapter, we investigate the theoretical per-node transmission limit of hybrid wireless networks over fading channels. The remainder of this chapter is organized as follows. In Section 2.1, we formulate the hybrid wireless network model. The principle of opportunistic communication and frequency reuse are introduced in Section 2.2. The outage throughput capacity and ergodic throughput capacity are explored in Section 2.3 and Section 2.4, respectively. The QoS performance analysis of the AEP is further provided in Section 2.5. In Section 2.6, we present some concluding remarks.

2.1 Hybrid Wireless Network Modeling

2.1.1 Hybrid Wireless Network Model

We make the following assumptions for the hybrid wireless network model [4] [7] [11] [111].

1. We construct a network consisting of n nodes, which are uniformly placed over a square area of $[0, \sqrt{n}] \times [0, \sqrt{n}]$.
2. Placing b base stations regularly as in Figure 2.1, the network is thus partitioned into b square cells with side length $c = \sqrt{n/b}$. Each cell contains only one base station and these base stations are linked together by a wired network to form

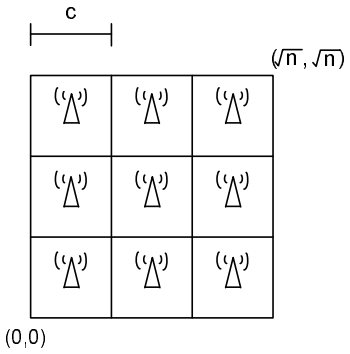

Figure 2.1. The square network of size $\sqrt{n} \times \sqrt{n}$ is partitioned into b cells of size $\sqrt{\frac{n}{b}} \times \sqrt{\frac{n}{b}}$.

an infrastructure.[1] Further, we assume $b = o(\frac{n}{\log n})$ to make sure that the base station number b tends to infinity as $n \to \infty$, but at a *much slower* rate.

3. The baseband model for the communications between node i and node j (or between node i and base station) at time slot t is described as:

$$Y_t^j = \alpha_{ij} X_t^i + Z_t^j. \tag{2.1}$$

• X_t^i is the complex baseband signal node i transmits, Y_t^j is the complex baseband signal node j receives, and Z_t^j is a Gaussian independent and identically distributed (*i.i.d.*) random variable with zero mean and variance σ_z^2.

• α_{ij} characterizes both the large-scale attenuation and small-scale fading of the channel.

• Node i transmits with power P and the signal is received at node j with power $P \cdot l(|X_i - X_j|) \cdot |h_{ij}|^2$. Here, $l(|X_i - X_j|) = \min(1, \frac{e^{-\gamma \rho_{ij}}}{\rho_{ij}^{\alpha}})$ represents the large-scale radio attenuation function, in which α and γ (normally $\alpha > 2$ and $\gamma > 0$) are the path-loss exponent and absorption constant of the attenuation,

[1] In this work, we assume the base stations are connected by high bandwidth long range links and thus there is no capacity constraint within the infrastructure [7]. These base stations neither generate nor consume data. They serve purely as relays for traffic of nodes.

respectively. Besides, ρ_{ij} is the distance between node i and j, and h_{ij} denotes the small-scale fading property of the channel.

2.1.2 Transmission Modes

There are two types of transmission mode employed in the hybrid wireless network: the *intra-cell* mode and the *infrastructure* mode. When the source node chooses a destination located within the same cell, the intra-cell transmission mode is in effect. The data is transmitted directly from the source to the destination through a single hop, without the aid of infrastructure. On the other hand, if the two nodes are located in different cells, the infrastructure transmission mode is implemented instead, as specified later in Section 2.3.

We partition the total channel bandwidth of W Hz into two orthogonal sub-channels with W_1 Hz and W_2 Hz. The W_1 Hz sub-channel is assigned for data transmission from the source to destination (intra-cell mode or the uplink phase of infrastructure mode), while the W_2 Hz bandwidth is allocated for transmitting the data from the base station to the destination (the downlink phase of infrastructure mode).

2.2 Preliminaries

2.2.1 The Number of Nodes Per Cell

The following lemma proves that there are $\Theta(\frac{n}{b})$ nodes within each cell.

Lemma 2.2.1 *For $b = o(\frac{n}{\log n})$ and $n \to \infty$, the number of nodes, n_c, in each cell of side length $c = \sqrt{n/b}$ is bounded by $\Theta(\frac{n}{b})$.*

Proof. Let event A denote a *Bernoulli* event that a particular node i, $1 \leq i \leq n$, falls into a particular cell of area c^2. Because the nodes are placed uniformly on the

network, it is clear that the probability of event A is $P_A = \frac{n/b}{n} = \frac{1}{b}$. Therefore, the number of nodes, n_c, has a *binomial* distribution with parameters (P_A, n). Using the *Chernoff* bound, we have

$$Pr\left(n_c > k_1\frac{n}{b}\right) \leq \frac{E\{\exp(n_c)\}}{\exp(\frac{k_1 n}{b})}$$

where k_1 is a constant. Since $E\{\exp(n_c)\} = \big(1+(e-1)P_A\big)^n \leq \exp\big[(e-1)\frac{n}{b}\big]$ (because $1 + x \leq exp(x)\big)$, we obtain

$$Pr\left(n_c > k_1\frac{n}{b}\right) \leq \exp\left\{-\frac{n}{b}[k_1 - (e-1)]\right\}. \tag{2.2}$$

As long as $k_1 > e - 1$, we know from the union bound that Pr(some cells have more than $\frac{k_1 n}{b}$ nodes) converges to zero as n tends to infinity.

Similarly, we have

$$Pr\left(n_c < k_2\frac{n}{b}\right) \leq \frac{E\{\exp(-n_c)\}}{\exp(\frac{-k_2 n}{b})}$$

where k_2 is also a constant. Since $E\{\exp(-n_c)\} = \big(1 + (e^{-1} - 1)P_A\big)^n \leq \exp\big[(e^{-1} - 1)\frac{n}{b}\big]$, we obtain

$$Pr\left(n_c < k_2\frac{n}{b}\right) \leq \exp\left\{-\frac{n}{b}[(1 - e^{-1}) - k_2]\right\}. \tag{2.3}$$

As long as $k_2 < 1 - e^{-1}$, we know from the union bound that Pr(some cells have less than $\frac{k_2 n}{b}$ nodes) converges to zero as n tends to infinity. Hence, it is concluded that each cell contains $\Theta(\frac{n}{b})$ nodes and we complete the proof. □

2.2.2 Opportunistic Communication

In a particular cell, assume that these n_c nodes are time-sharing and transmit in a round robin fashion. When being slotted, the scheduled source node i is assigned

$\mu W_1 = W_1/n_c$ Hz bandwidth for transmission. From the information theory point of view, the maximum achievable rate of reliable communication is

$$\log\left(1 + \frac{P \cdot l(|X_i - X_j|) \cdot |h_{ij}|^2}{\mu W_1 N_0}\right) \quad bit/s/Hz. \tag{2.4}$$

To describe if a transmission is received successfully by its intended recipient, in most literatures, two possible models, the so called protocol model and physical model, are adopted. Therefore, it is meaningful to explore the following question: what is the ultimate limit of information rate of the whole network if any transmission strategy is allowed? If we ignore the protocol model and physical model, the upper bound of the information rate is given by Theorem 1 and the detailed proof is given by Appendix A.

Theorem 1. *Consider a wireless network M consisting of m nodes. Dynamically, at time instants $k = 1, 2, \cdots, n$, node i from the source set S transmits the signal X_k^i to node j within the destination set D. If the information rates $\{R^{ij}\}$ are achievable, then for any subset S of M, we have*

$$R^{SD} \leq \sum_{j \in D} \left[\frac{1}{2}\log(1 + \frac{E|\sum_{i \in S} \alpha_{ij} X_k^i|^2}{\sigma_z^2})\right] + \varepsilon_n, \tag{2.5}$$

where $R^{SD} = \sum_{i \in S, j \in D} R^{ij}$, and $\varepsilon_n \to 0$ as $n \to \infty$.

As is known, there is a conceptual difference between the AWGN channel and fading channel in terms of the throughput capacity. In the former, one can send data at a positive rate while keeping the error probability as small as desired. This, nevertheless, cannot be done for the fading channel as long as the probability that the channel is in deep fade is non-zero [62] [18]. Specifically, if the signal duration is short compared to the channel coherent time, we have a slow fading fading channel; otherwise, if the signal duration is much longer than the channel coherent time, the signal will be subject to different fading effects and thus we have a fast fading channel.

Therefore, we introduce the following alternative criteria for throughput performance based on the different fading scenarios: ϵ-*outage capacity* C_ϵ (slow fading), which is the largest rate of transmission such that the outage probability P_{out} is less than ϵ, and *ergodic capacity* $\bar{C}$ (fast fading), which is defined as the ensemble average of channel capacity over all possible channel realizations.

Suppose the transmitter encodes the data at the rate of R bit/sec/Hz, then the system is said to be in outage if $\log\left(1+\frac{P\cdot l(|X_i-X_j|)\cdot|h_{ij}|^2}{\mu W_1 N_0}\right) < R$. The related outage probability is

$$P_{out} = Pr\left\{\log(1+\frac{P\cdot l(|X_i-X_j|)\cdot|h_{ij}|^2}{\mu W_1 N_0}) < R\right\}. \tag{2.6}$$

Solving $P_{out}=\epsilon$ yields the following outage capacity

$$C_\epsilon = \log\left(1+F^{-1}(\epsilon)\frac{P\cdot l(|X_i-X_j|)}{\mu W_1 N_0}\right) bit/s/Hz, \tag{2.7}$$

where $F(\cdot)$ is the *cumulative distribution function* of $|h_{ij}|^2$.

Can we do better?

Assume, for any scheduled source, that there are κ nodes within the same cell, whose Euclidean distance away from destination node j is greater than ρ_{ij}. [2] To overcome the fading impairments, we allow these κ nodes to be opportunistic sources and transmit data simultaneously to the destination node j. The channel thus becomes a multiple-access fading channel and the optimal multiple access strategy is for all these sources to spread their signal across the entire bandwidth. However, rather than decoding every node treating the *intra-cell* interference from other nodes as noise, a successive interference cancelation (SIC) technique is employed at the receiver. That is, after one node is decoded, its signal is deducted from the aggregate

[2] In this work, we only focus on the case where the Euclidean distance information is known by all the users. One possible justification is that the base station can collect the distance information (base station coordination) and broadcast it to all the users via control channels.

received signal before the next node's information is decoded, which significantly reduces the intra-cell interference. It is worth mentioning the motivation that we choose these farther nodes as opportunistic nodes is to make sure the transmissions from the opportunistic sources do not impair the achievable transmission rate of the scheduled source [2]. According to the interference model given in [2], the transmission is successful if the positions of other transmitters X_κ simultaneously transmitting over the same channel satisfy $|X_\kappa - X_j| \geq (1+\Delta)|X_i - X_j|$, where $\Delta > 0$ models the guard zone.

Let ρ_{id} $(i = 0, 1, ..., \kappa)$ denote the distance of these sources away from the destination node j, where ρ_{od} is the distance of scheduled node away from the destination and $\rho_{id}(i \neq 0)$ represents the distance of the opportunistic source away from the destination. Without loss of generality, we have $\rho_{0d} \leq \rho_{1d} \leq \cdots \leq \rho_{\kappa d}$. The SIC strategy maximizes the sum rate and achieves a set of sum rate satisfying

$$\begin{aligned} R_0 &\leq \log\left(1 + \frac{P \cdot l(|X_0 - X_j|) \cdot |h_{0j}|^2}{\eta W_1 N_0}\right) \\ &\vdots \\ \sum_{i=0}^{\kappa} R_i &\leq \log\left(1 + \frac{\sum_{i=0}^{\kappa} P \cdot l(|X_i - X_j|) \cdot |h_{ij}|^2}{\eta W_1 N_0}\right) \end{aligned} \tag{2.8}$$

where R_i denotes the ith node's achievable rate. Since each opportunistic source can spread its signal over the entire bandwidth assigned to these $\kappa + 1$ nodes, μ in (3.24) is replaced with η in the achieved rate (2.8), as further specified later.

Lemma 2.2.2 *For a given source and destination pair in any cell, there are $\kappa = \Theta(\frac{n}{b})$ nodes within the same cell that have greater distances from the destination than the source node.*

Proof. For a scheduled source node i and a destination node j with the distance d away from each other, we construct a disk (radius d) centered at node j, as shown in

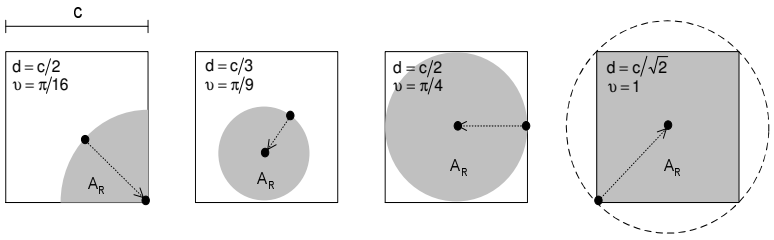

Figure 2.2. For a given source with distance d from its intended receiver, the opportunistic sources should be located outside (white area) the disk of radius d centered at the receiver.

Figure 2.2. Apparently, any random node located within the disk is closer to node j than node i. Hence, the opportunistic sources of node i must be located outside of the disk. Our goal is to estimate how many nodes are located in the remaining cell area outside of the disk.

Based on the locations of node i and j, a portion of the disk may fall outside the cell boundary. We will not take this portion (including the boundary) into account, since in this study the opportunistic sources are only chosen from the same cell region. Let A_R denote the area of the disk with radius d, then we can always represent A_R with υc^2, $\upsilon \in (0, 1)$.[3] Besides, υ is only determined by the random locations of node i and j and thus is irrelevant of n.

Further, assume that node q, $(1 \leq q \leq n_c - 2)$ is any node in the cell other than the node i and j, and let random variable Z_q denote whether node q is located outside of A_R. Clearly, the random variable Z_q is expressed as

$$Z_q = \begin{cases} 1\,, & \textit{node } q \textit{ is outside of } A_R \\ 0\,, & \textit{otherwise} \end{cases} \tag{2.9}$$

[3]We need to point out that $\upsilon = 0$ and $\upsilon = 1$ stand for the special case of $d = 0$ (self transmission) and $d = c/\sqrt{2}$ (boundary transmission), respectively. To avoid possible ambiguity, in this study we assume $\upsilon \in (0, 1)$.

Since the probability that a random node q is located outside of A_R is $1-\upsilon$, we have $E[Z_q] = 1-\upsilon$. Note that $\kappa = \sum_{q=1}^{n_c-2} Z_q$ is the total number of nodes in the cell, excluding the transmitter i and receiver j, that are located outside of A_R. According to *Strong Law of Large Numbers*, with probability equal to 1,

$$\frac{\kappa}{n_c-2} = \frac{1}{n_c-2}\sum_{q=1}^{n_c-2} Z_q \to 1-\upsilon \tag{2.10}$$

As $n \to \infty$ (and thus n_c), κ is approximately $(1-\upsilon)n_c$. Since $\upsilon \in (0,1)$ is irrelevant of n and $n_c = \Theta(\frac{n}{b})$, $\kappa = (1-\upsilon)n_c = k_1 n_c$ where $0 < k_1 < 1$. Therefore, the proof is complete. □

Lemma 2.2.2 proves that for a given source and destination pair, there exist *at most* $\kappa = \Theta(\frac{n}{b})$ nodes within the same cell that can serve as opportunistic sources.

To practically apply the proposed opportunistic transmission strategy, we split τ, the transmission time allocated to the scheduled source τ, into two parts. The first part $\theta\tau$ is used for the scheduled source to inform every opportunistic node about its destination and set up the transmission cooperation. The second part $(1-\theta)\tau$ is for the scheduled source and opportunistic sources to transmit the data to the common destination. In this study, we assume that θ $(0 < \theta < 1)$ remains constant, irrespective of the transmission rate.

2.2.3 Frequency Reuse

Since the traffics of the uplink phase and the downlink phase are assigned with orthogonal sub-channels, there is no interference between these two types of traffics. However, the interference still exists between the same type of traffic within different cells, which is referred to as the *inter-cell* interference. Fortunately, such interference could be minimized by employing the frequency reuse concept as illustrated in [30]. Specifically, we first group the cells together to form a certain number

of clusters. Then, we assign different frequency bands to the cells within the same cluster; whereas, among different clusters, these frequency bands are reused as shown in Figure 2.3. Hence, the transmissions in the cells (in different clusters) with the same frequency can be carried out simultaneously without causing excessive inter-cell interference, as long as the distance between these cells is large enough.

Lemma 2.2.3 *For any integer $a > 0$, there exists a reuse policy with M^2 (*reuse factor*) frequency bands where $M = 2(a+1)$, such that all cells in the network can transmit simultaneously with bounded interferences.*

Proof. As illustrated in Figure 2.3, we assign a reuse set of M^2 frequency bands, $\{f_1, f_2, \cdots, f_{M^2}\}$ to M^2 cell of each cluster. Note that for a given cell o, there is always one cell in every cluster that occupy the same frequency. We can consider the maximum interference by observing that the first-tier ($i = 1$) interferers are transmitters in eight closest cells located at the distance of at least $[2(a+1)-1]c$ away from the receivers in cell o.

Extending the sum of interferences of the entire plane and taking into account that there are possibly $\kappa + 1 \approx \kappa$ transmitters in each cell, the upper bound of this sum is

$$\begin{aligned} I(c,d) &\leq \sum_{i=1}^{\infty} 8i\kappa P[2ci(a+1)-c]^{-\alpha} e^{-\gamma(2ci(a+1)-c)} \\ &\overset{(a)}{\leq} 8\kappa P[2c(a+\frac{1}{2})]^{-\alpha} \sum_{i=1}^{\infty} i^{-\alpha+1} e^{-2\gamma ci(a+\frac{1}{2})} \end{aligned}$$

where (a) is due to $2ci(a+1) - c \geq 2ci(a+1/2)$. [4]

[4]In this proof, we mainly consider the large-scale attenuation, since the large-scale attenuation will dominate in the long distance transmission.

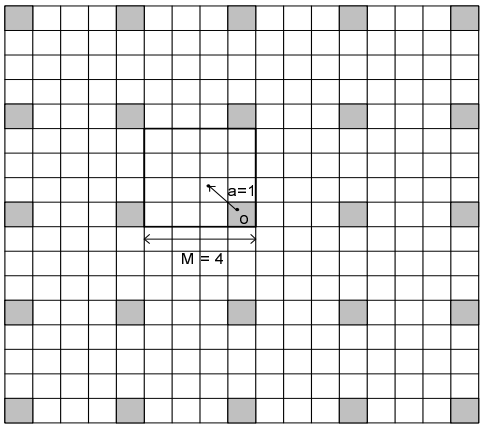

Figure 2.3. Frequency reuse scheme for a=1. The shaded squares share the same frequency.

Next, in terms of the minimum interference, we observe that the first-tier interferers are at the distance of at most $[2(a+1)+1]\sqrt{2}c$ cells away. So we can express the lower bound of the interference as

$$\begin{aligned} I(c,d) &\geq \sum_{i=1}^{\infty} 8i\kappa P[2\sqrt{2}ci(a+1)+\sqrt{2}c]^{-\alpha} e^{-\gamma(2\sqrt{2}ci(a+1)+\sqrt{2}c)} \\ &\overset{\text{(b)}}{\geq} 8\kappa P[2\sqrt{2}c(a+\frac{3}{2})]^{-\alpha} \sum_{i=1}^{\infty} i^{-\alpha+1} e^{-2\sqrt{2}\gamma ci(a+\frac{3}{2})} \end{aligned}$$

where (b) follows from $2\sqrt{2}ci(a+1)+\sqrt{2}c \leq 2\sqrt{2}ci(a+\frac{3}{2})$. Evidently, if $\alpha > 2$ and $\gamma > 0$, the summation terms in the upper bound and lower bound converge and the values of the bounds are defined by $\kappa e^{-\alpha}$. Since $\kappa = \Theta(\frac{n}{b})$ and $c = \sqrt{n/b}$, as $n \to \infty$, the interference decreases at the rate of $\Theta((\frac{n}{b})^{1-\frac{\alpha}{2}})$.

Similarly, for the interference for the downlink $I'(c,d)$ (a special case when $\kappa = 0$) deceases at the rate $\Theta((\frac{n}{b})^{-\frac{\alpha}{2}})$. The proof is complete. [5] □

Lemma 2.2.3 proves that inter-cell interference I is limited with the introduction of frequency reuse strategy. Therefore, we treat the inter-cell interference I as additive colored Gaussian noise throughout this chapter, unless otherwise stated.

[5] A similar proof method is adopted in [4].

2.3 Outage Throughput Capacity of Hybrid Wireless Networks

In this section, we focus on the theoretical per-node transmission limit of hybrid wireless networks over slow fading channels. Before we embark on this, it is noted that in many previous studies the throughput capacity is specified from the transmitter perspective as the average rate at which each node could transmit data to its destination. However, in this chapter, we schedule the opportunistic sources to transmit simultaneously with the scheduled source. Therefore, to illustrate the advantage of multiple access technique and explore the slow fading property of the channel, we define the feasible *ϵ-outage throughput capacity* as follows.

Definition 1. *For a hybrid wireless network of n nodes and b base stations, a ϵ-outage throughput capacity of $T_\epsilon(n,b)$ bit/s for each node is feasible if under the intra-cell mode or infrastructure mode, there is a spatial and temporal scheme for scheduling transmissions such that every node can receive $T_\epsilon(n,b)$ bit/s with the outage probability less than ϵ.*

2.3.1 Outage Throughput Capacity under Intra-cell Mode

First, we discuss the outage throughput capacity under intra-cell transmission mode. Taking into account the benefits of opportunistic sources and SIC decoding strategy, we find the bandwidth allocated to the scheduled source under intra-cell mode is $\eta W_1 = \frac{\kappa+1}{n_c}\frac{W_1}{M^2} = \Theta(W_1)$ Hz, where M^2 is the frequency reuse factor. Actually, ηW_1 denotes the entire bandwidth assigned to these $\kappa+1$ scheduled and opportunistic sources.[6] Clearly, the above bandwidth allocation is continuous. This

[6]To understand this, in this work, our approach is first to assign orthogonal bandwidth between the $\kappa+1$ sources and the remaining $n_c-\kappa-1$ nodes, aiming to eliminate the intra-cell interferences. Since at the receiver, we employ the SIC strategy to reduce the interferences within these $\kappa+1$ sources, these $\kappa+1$ sources will share the ηW_1 Hz bandwidth.

is a reasonable assumption if the subcarrier bandwidth spacing is narrow compared to the total bandwidth. An example system is LTE which can operate with 15K Hz spacing and 2048 subcarriers. The sum of the transmission rates for the scheduled and opportunistic sources is given in Lemma 2.3.1.

Lemma 2.3.1 *For source node i and destination node j under* intra-cell *transmission mode, as $n \to \infty$, the transmission rate over Nakagami-m fading is*

$$R_{intra} = O\bigg(\log[(\epsilon^{\frac{1}{m}})^{\frac{b}{n}} \frac{n}{b}] \bigg) \, bit/s/Hz. \tag{2.11}$$

Proof. Assume that the scheduled source and opportunistic sources encode the data at the rate of R bit/s/Hz. With the introduction of opportunistic sources and SIC decoding strategy, the outage performance is

$$\begin{aligned} \widetilde{P}_{out} &= Pr\bigg\{ \log(1 + \frac{\sum_{i=0}^{\kappa} P \cdot l(|X_i - X_j|) \cdot |h_{ij}|^2}{\eta W_1 N_0 + I}) < R \bigg\} \\ &\overset{(a)}{\simeq} Pr\bigg\{ \log(1 + \frac{\sum_{i=0}^{\kappa} P \cdot min(1, \rho_{0d}^{-\alpha} e^{-\gamma \rho_{0d}}) \cdot |h_{ij}|^2}{\eta W_1 N_0 + I}) < R \bigg\} \\ &= Pr\bigg\{ ||\mathbf{h}||^2 < \frac{(2^R - 1)(\eta W_1 N_0 + I)}{P \cdot min(1, \rho_{0d}^{-\alpha} e^{-\gamma \rho_{0d}})} \bigg\}, \end{aligned} \tag{2.12}$$

where $||\mathbf{h}||^2 = \sum_{i=0}^{\kappa} |h_{ij}|^2$. At step (a) we use ρ_{0d} to approximately represent the distance of opportunistic nodes away from the destination for analysis simplicity; the outage throughput capacity we derive later is thus the upper bound.

As is known, the pdf of a Nakagami-m random variable $|h_{ij}|$ (magnitude) is

$$f(h) = \frac{2}{\Gamma(m)} (\frac{m}{\Omega})^m h^{2m-1} e^{-mh^2/\Omega}, \quad h \geq 0 \tag{2.13}$$

where $\Gamma(\cdot)$ is the Gamma function, $m = \frac{E^2[h^2]}{Var[h^2]}$ is the shape parameter[7]. $\Omega = E[h^2]$ stands for the controlling spread and $\Omega = 1$ for Nakagami-m fading.

[7]In this study, we assume m is an integer for analysis clarity.

Note that a Gamma-distributed random variable with shape k and scale θ is distributed as

$$\Gamma(k,\theta) = \frac{1}{\theta^k}\frac{1}{\Gamma(k)}x^{k-1}e^{-\frac{x}{\theta}}, \quad x \geq 0.$$

Therefore, we conclude that $|h_{ij}|^2$ is Gamma-distributed $|h_{ij}|^2 \sim \Gamma(m, \frac{1}{m})$, since the pdf of $|h_{ij}|^2$ is

$$f(x) = \frac{m^m}{\Gamma(m)}x^{m-1}e^{-mx}, \quad x \geq 0. \tag{2.14}$$

In addition, it has been proved in Lemma 2.3.1.1 (Appendix B) that $||\mathbf{h}||^2 = \sum_{i=0}^{\kappa}|h_{ij}|^2$ is also Gamma-distributed $\Gamma\big((\kappa+1)m, \frac{1}{m}\big)$ as follows

$$f(x) \;=\; \frac{m^{(\kappa+1)m}}{\Gamma[(\kappa+1)m]}x^{(\kappa+1)m-1}e^{-mx}. \tag{2.15}$$

Applying the pdf of $||\mathbf{h}||^2$ into the outage performance (2.12) with T denoting the right-hand side, we have

$$\begin{aligned} Pr\{||\mathbf{h}||^2 < T\} &= \frac{m^{(\kappa+1)m}}{\Gamma[(\kappa+1)m]}\int_0^T x^{(\kappa+1)m-1}e^{-mx}dx \\ &\overset{\text{(a)}}{=} \frac{m^{(\kappa+1)m}}{\Gamma[(\kappa+1)m]}\cdot m^{-(\kappa+1)m}\cdot\gamma\Big((\kappa+1)m, mT\Big) \\ &\overset{\text{(b)}}{=} 1 - e^{-mT}\sum_{i=0}^{(\kappa+1)m-1}\frac{(mT)^i}{i!} \end{aligned}$$

where (a) follows the definition of incomplete gamma function; (b) follows that for integer n, $\gamma(n,x) = (n-1)!\big[1 - e^{-x}\sum_{i=0}^{n-1}\frac{x^i}{i!}\big]$ and $\Gamma(n) = (n-1)!$.

Then the resulting outage capacity over Nakagami-m fading is obtained by solving[8]

$$1 - e^{-\frac{m(2^R-1)}{sinr}}\sum_{i=0}^{(\kappa+1)m-1}\frac{\big[\frac{m(2^R-1)}{sinr}\big]^i}{i!} = \epsilon, \tag{2.16}$$

with $sinr = \frac{P\cdot min(1,\rho_{0d}^{-\alpha}e^{-\gamma\rho_{0d}})}{\eta W_1 N_0 + I}$.

[8]In (2.16), the *sinr* is introduced for brevity of notation, rather than the abbreviation for signal-to-interference-plus-noise ratio (SINR).

Clearly, no closed-form solution exists for arbitrary κ and m. Further, approximating e^{-x} by 1 for small x, we have the following outage performance at the regime of high SINR

$$\widetilde{P}_{out} = \frac{m^{(\kappa+1)m}}{[(\kappa+1)m]!}\big[\frac{(2^R-1)}{sinr}\big]^{(\kappa+1)m} \tag{2.17}$$

since according to (2.12), when T is small (high SINR)

$$\begin{aligned} Pr\{||\mathbf{h}||^2 < T\} &= \int_0^T \frac{m^{(\kappa+1)m}}{\Gamma[(\kappa+1)m]} x^{(\kappa+1)m-1} dx \\ &= \frac{m^{(\kappa+1)m}}{[(\kappa+1)m]!} T^{(\kappa+1)m}. \end{aligned}$$

Solving $\widetilde{P}_{out} = \epsilon$, we obtain the following outage capacity

$$C_\epsilon = \log\left\{1 + \frac{1}{m} \cdot \epsilon^{\frac{1}{(\kappa+1)m}} [(\kappa+1)m]!^{\frac{1}{(\kappa+1)m}} \cdot sinr\right\}. \tag{2.18}$$

Finally, we explore the scaling laws for outage throughput capacity under intra-cell transmission mode. Employing Stirling's approximation,

$$n! = \sqrt{2\pi n}\big(\frac{n}{e}\big)^n e^{\alpha_n}$$

with $\frac{1}{12n+1} < \alpha_n < \frac{1}{12n}$, we have $\frac{1}{m}[(\kappa+1)m]!^{\frac{1}{(\kappa+1)m}} = \Theta(\frac{n}{b})$. Together with $\kappa = \Theta(\frac{n}{b})$ (Lemma 2.2.2) and $I = \Theta\big((\frac{n}{b})^{1-\frac{\alpha}{2}}\big)$ (Lemma 2.2.3), the transmission rate is upper bounded by $\Theta\big(\log[(\epsilon^{\frac{1}{m}})^{\frac{b}{n}}\frac{n}{b}]\big)$. Therefore, the transmission rate for the scheduled and opportunistic sources R_{intra} over Nakagami-m fading is $O\big(\log[(\epsilon^{\frac{1}{m}})^{\frac{b}{n}}\frac{n}{b}]\big)$ $bit/s/Hz$. We complete the proof. □

Taking into account the temporal occupation $1-\theta$ and bandwidth allocation ηW_1, we conclude the per-node outage throughput capacity under intra-cell transmission mode $T_{\text{intra}}(n,b)$, which is determined by the product between the allocated bandwidth and the sum of the transmission rate, i.e., $(1-\theta)\cdot\eta W_1 \cdot R_{\text{intra}}$, is $O\big(\log[(\epsilon^{\frac{1}{m}})^{\frac{b}{n}}\frac{n}{b}]\, W_1\big)$ bit/s.

2.3.2 Outage Throughput Capacity Under Infrastructure Mode

Another scenario is that the sources transmit the data to the destination located in a different cell via the infrastructure transmission mode. Specifically, during the *uplink phase*, the source and the opportunistic sources first transmit all traffic to the base station within the cell. Then, in the *transport phase*, the base station decodes the received data from each source and send them through the wired network to the base station located in the destination cell. Subsequently, the data is retransmitted to the destination during the *downlink phase*.

Lemma 2.3.2 *For source node i and destination node j under* infrastructure *transmission mode, as $n \to \infty$, the transmission rate over Nakagami-m fading is*

$$R_{infra} = \Theta\left(\log(\epsilon^{\frac{1}{m}} \frac{n}{b}) \right) \quad bit/s/Hz. \tag{2.19}$$

Proof. The proof is mainly based on the fact that the uplink throughput and downlink throughput are equal. Apparently, the uplink traffics are very similar to the intra-cell transmission mode, with the destination node replaced with the base station. During the downlink phase, neither the base station cooperation (one base station within each cell) nor the interference cancellation strategy is allowed, which results in a suboptimal throughput performance. [9] The outage throughput performance for the downlink phase is

$$\begin{aligned} \widetilde{P}'_{out} &= Pr\left\{ \log(1 + \frac{P \cdot l(|X_b - X_j|) \cdot |h_{bj}|^2}{\lambda W_2 N_0 + I'}) < R \right\} \\ &= Pr\left\{ |h_{bj}|^2 < \frac{(2^R - 1)(\lambda W_2 N_0 + I')}{P \cdot min(1, \rho_{0d}^{-\alpha} e^{-\gamma \rho_{0d}})} \right\}, \end{aligned} \tag{2.20}$$

[9] This assumption is motivated in many practical scenarios. During the uplink phase, the base station is capable of adapting the data rate and harnessing multiuser diversity; whereas during the downlink, additional limitations such as decoding complexity and delay constraints, etc., preclude the application of the multiuser technique (superposition coding) for each node as the receiver.

where h_{bj} characterizes the channel from the base station to the receive node j, λ is the fraction of bandwidth W_2 assigned to the receive node j, and I' represents the inter-cell interference.

Similarly, applying the pdf of $|h_{bj}|^2$ (5.4) into (2.20), we derive the outage performance at high SINR as,

$$\widetilde{P}'_{out} = \frac{m^m}{m!}\big[\frac{(2^R-1)}{sinr'}\big]^m, \tag{2.21}$$

with $sinr' = \frac{P \cdot min(1, \rho_{0d}^{-\alpha} e^{-\gamma \rho_{0d}})}{\lambda W_2 N_0 + I'}$.

Solving $\widetilde{P}'_{out} = \epsilon$, we obtain the downlink outage capacity

$$C'_\epsilon = \log\left\{1 + \frac{1}{m}(m!)^{\frac{1}{m}} \cdot \epsilon^{\frac{1}{m}} \cdot sinr'\right\}. \tag{2.22}$$

During the downlink phase, each base station allocates the bandwidth W_2/M^2 equally to serve every node within the cell. Therefore, the bandwidth assigned to each node is limited to $\lambda W_2 = \frac{W_2}{M^2 n_c} = \Theta(\frac{b}{n} W_2)$, compared to the uplink bandwidth $\eta W_1 = \frac{\kappa+1}{n_c}\frac{W_1}{M^2} = \Theta(W_1)$. Besides, from Lemma 2.2.3, the downlink interference is $I' = \Theta\big((\frac{n}{b})^{-\frac{\alpha}{2}}\big)$. Hence, the downlink transmission rate over Nakagami-m fading is straightforward: $\Theta\big(\log(\epsilon^{\frac{1}{m}}\frac{n}{b})\big)$.

Let us compare the derived downlink transmission rate with the uplink transmission rate (2.11). Clearly, as the nodes increase ($\kappa \gg 1$), the uplink transmission rate is much larger than downlink transmission rate. This is due to the fact that the negative influence of the outage probability ϵ is mitigated by the exponent $\frac{1}{\kappa+1}$ during the uplink phase. Therefore, the transmission rate under the infrastructure transmission mode R_{infra}, which is limited by the downlink phase, is $\Theta\big(\log(\epsilon^{\frac{1}{m}}\frac{n}{b})\big)$. The proof is complete. □

Further, taking into consideration the bandwidth limitation of downlink phase $\left(\Theta(\frac{b}{n}W_2)\right)$, the per-node outage throughput capacity under the infrastructure transmission mode, is thus $T_{\text{infra}}(n,b) = \Theta\left(\frac{b}{n}\log(\epsilon^{\frac{1}{m}}\frac{n}{b})\,W_2\right)$ *bit/s*.

Now we summarize the scaling laws for outage throughput capacity with the following theorem.

Theorem 2. *For a hybrid wireless network of n nodes and b base stations over Nakagami-m fading channels, if* $b = o(\frac{n}{\log n})$*, the per-node outage throughput capacity under the intra-cell transmission mode is*

$$T_{intra}(n,b) = O\left(\log[(\epsilon^{\frac{1}{m}})^{\frac{b}{n}}\frac{n}{b}]\,W_1\right)\ bit/s. \tag{2.23}$$

The related per-node outage throughput capacity under the infrastructure transmission mode is

$$T_{infra}(n,b) = \Theta\left(\frac{b}{n}\log(\epsilon^{\frac{1}{m}}\frac{n}{b})\,W_2\right)\ bit/s. \tag{2.24}$$

Finally, we provide the Monte Carlo simulations to demonstrate the validity of the derived theoretical bounds. Figure 2.4 depicts the outage capacity (R_{intra} and R_{infra}) with κ opportunistic nodes ($m = 1$, $\epsilon = 0.01$). It is shown that every simulated curve is in agreement with the corresponding theoretical curve. One can attribute the gap to the fact that during the derivation of the closed-form solution (2.17), we replaced e^{-x} with 1. Clearly, with opportunistic nodes, the uplink outage capacity exceed the downlink scenario. However, the advantage of opportunistic nodes is not obvious as κ increases. The reasonable explanation is that, in our formulated scenario, we adopt "equal" power allocation among the scheduled and opportunistic sources for simplicity.

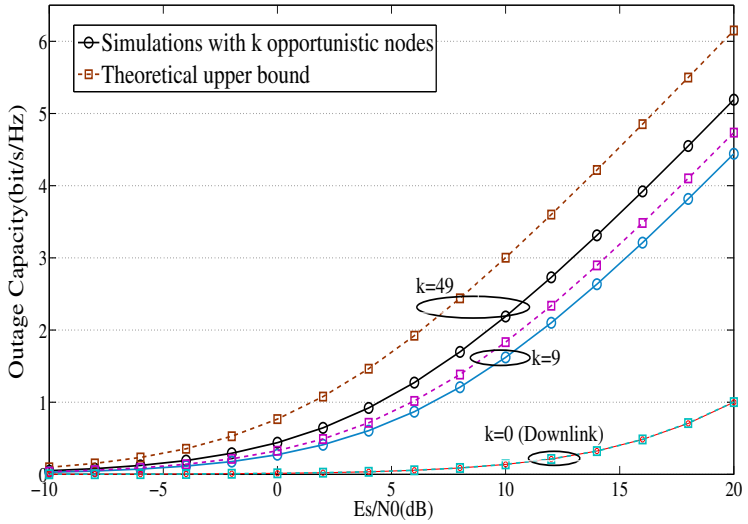

Figure 2.4. Outage capacity over Nakagami-m fading channel ($\epsilon = 0.01$).

To intuitively illustrate the scaling laws of the derived outage throughput capacity (T_{intra} and T_{infra}), in Figure 2.5 we compare the uplink outage throughput capacity with the downlink scenario under the infrastructure mode (SINR=10 dB). Aiming to practically apply the opportunistic transmission strategy, we thereby assume the temporal occupation $\theta = 1/2$. Clearly, as the total number of nodes n_c increases, more nodes within the same cell could be chosen as the opportunistic sources ($\kappa \uparrow$), and thus the uplink throughput capacity (2.23) exceeds the downlink scenario (2.24). It is worth mentioning the fading impairment ϵ of both the uplink and downlink phase is weakened by Nakagami-m shape parameter m. Therefore, large m closes the gap between the the uplink throughput and downlink throughput as shown in Figure 2.5.

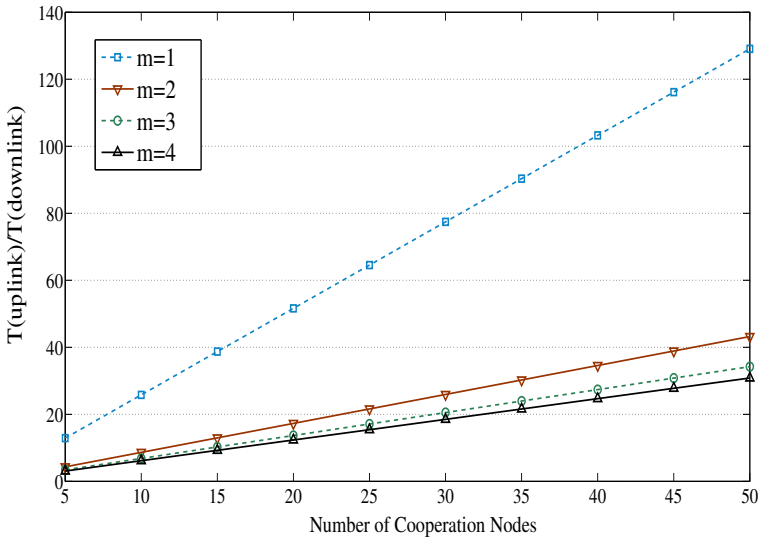

Figure 2.5. Ratio between uplink throughput capacity and downlink throughput capacity under infrastructure mode over Nakagami-m fading ($\epsilon = 0.001$).

2.4 Ergodic Throughput Capacity of Hybrid Wireless Networks

In this section, we turn our attention to the per-node throughput capacity of hybrid wireless networks over fast fading channels. Similarly, we define the feasible *ergodic throughput capacity* of the hybrid wireless network as follows.

Definition 2. *For a hybrid wireless network of n nodes and b base stations, an ergodic throughput capacity of $\bar{T}(n,b)$ bit/s for each node is feasible if under the intra-cell mode or infrastructure mode, there is a spatial and temporal scheme for scheduling transmissions such that every node can averagely receive $\bar{T}(n,b)$ bit/s over all possible channel realizations.*

2.4.1 Ergodic Throughput Capacity under Intra-cell Mode

First, let us discuss the ergodic throughput capacity under intra-cell transmission mode. In the fast fading scenario, the ergodic capacity $\bar{R}$ is defined as the ensemble average of channel capacity over all possible channel realizations [62]

$$\bar{R} = \mathbf{E}\big[\log(1 + \frac{P \cdot l(|X_i - X_j|) \cdot |h_{ij}|^2}{W_1 N_0})\big] bit/s/Hz. \tag{2.25}$$

where h_{ij} characterizes the fast fading property of the channel.

Then with the introduction of opportunistic sources and SIC decoding strategy, the sum of the transmission rates for the scheduled and opportunistic sources is

$$\begin{aligned}
\sum_{i=0}^{\kappa} \bar{R}_i &= \mathbf{E}\Big\{ \log\big(1 + \frac{\sum_{i=0}^{\kappa} P \cdot l(|X_i - X_j|) \cdot |h_{ij}|^2}{\eta W_1 N_0 + I}\big) \Big\} \\
&\overset{(a)}{\simeq} \mathbf{E}\Big\{ \log(1 + \frac{\sum_{i=0}^{\kappa} P \cdot min(1, \rho_{0d}^{-\alpha} e^{-\gamma \rho_{0d}}) \cdot |h_{ij}|^2}{\eta W_1 N_0 + I}) \Big\} \\
&= \mathbf{E}\Big\{ \log\big(1 + ||\mathbf{h}||^2 \cdot sinr\big) \Big\},
\end{aligned} \tag{2.26}$$

where $||\mathbf{h}||^2 = \sum_{i=0}^{\kappa} |h_{ij}|^2$ and $sinr = \frac{P \cdot min(1, \rho_{0d}^{-\alpha} e^{-\gamma \rho_{0d}})}{\eta W_1 N_0 + I}$.

The above derivations are based on the following assumptions: 1) Lemma 2.2.3 tells us that inter-cell interference is limited with the introduction of frequency reuse strategy. Therefore, we can treat the inter-cell interference I as additive colored Gaussian noise; 2) at step (a) we use ρ_{0d} to approximately represent the distance of opportunistic nodes away from the destination for analysis simplicity.

With the pdf of $||\mathbf{h}||^2$ (2.15), the analytical expression for the sum transmission rate over fast fading channel is presented by (2.27). In (2.27), (a) follows the variable replacement $mx = t$; (b) is derived from

$$\int_0^{\infty} \ln(1 + ax) \cdot x^{\beta} \cdot e^{-x} dx = \sum_{\mu=0}^{\beta} \frac{\beta!}{(\beta - \mu)!} \Big[\frac{(-1)^{\beta-\mu-1}}{a^{\beta-\mu}} \cdot e^{\frac{1}{a}} \cdot Ei(-\frac{1}{a}) + \sum_{k=1}^{\beta-\mu} (k-1)! \cdot (-\frac{1}{a})^{\beta-\mu-k} \Big],$$

with the *exponential integral function*

$$Ei(x) = -\int_{-x}^{\infty} \frac{e^{-t}}{t} dt = \int_{-\infty}^{x} \frac{e^{t}}{t} dt, \quad x < 0.$$

Further, we explore the implication of (2.27) in both low SINR and high SINR scenarios. At low SINR, we employ the approximation $\ln(1+x) \approx x$ and obtain

$$\begin{aligned}
\bar{R} &\approx \int_0^\infty \frac{sinr}{\ln 2} x \cdot \frac{m^{(\kappa+1)m}}{\Gamma[(\kappa+1)m]} \cdot x^{(\kappa+1)m-1} e^{-mx} dx \\
&\overset{(a)}{=} \frac{sinr \cdot m^{(\kappa+1)m}}{\Gamma[(\kappa+1)m] \cdot \ln 2} \big[(\kappa+1)m\big]! \cdot m^{-\big[(\kappa+1)m+1\big]} \\
&\overset{(b)}{=} (\kappa+1) \cdot sinr \cdot \log_2^e
\end{aligned} \tag{2.28}$$

where (a) follows $\int_0^\infty x^n e^{-\mu x} dx = n! \cdot \mu^{-n-1}$ and (b) follows $\Gamma(n) = (n-1)!$.

Similarly, employing $\log(1+x) \approx \log(x)$ at the regime of high SINR, we reach

$$\begin{aligned}
\bar{R} &\approx \int_0^\infty \log\big(sinr \cdot x\big) \frac{m^{(\kappa+1)m}}{\Gamma[(\kappa+1)m]} x^{(\kappa+1)m-1} e^{-mx} dx \\
&= \log(sinr) \cdot \frac{m^{(\kappa+1)m}}{\Gamma[(\kappa+1)m]} \int_0^\infty x^{(\kappa+1)m-1} e^{-mx} dx + \\
&\quad \frac{m^{(\kappa+1)m}}{\Gamma[(\kappa+1)m] \cdot \ln 2} \int_0^\infty \ln x \cdot x^{(\kappa+1)m-1} e^{-mx} dx \\
&= \log(sinr) + \frac{1}{\Gamma[(\kappa+1)m] \cdot \ln 2} \Bigg[\int_0^\infty \ln x \cdot x^{(\kappa+1)m-1} e^{-x} dx - \\
&\quad \ln m \int_0^\infty x^{(\kappa+1)m-1} e^{-x} dx \Bigg] \\
&\overset{(a)}{=} \log\left(\frac{sinr}{m}\right) + \log_2^e \cdot \left[\big(1 + \frac{1}{2} + \cdots + \frac{1}{(\kappa+1)m-1}\big) - \mathbb{C} \right]
\end{aligned} \tag{2.29}$$

$$\begin{aligned}
\bar{R} &= \int_0^\infty \log(1 + x \cdot sinr\big) \cdot \frac{m^{(\kappa+1)m}}{\Gamma[(\kappa+1)m]} \cdot x^{(\kappa+1)m-1} e^{-mx} dx \\
&\overset{(a)}{=} \frac{1}{\Gamma[(\kappa+1)m] \cdot \ln 2} \int_0^\infty \ln(1 + x \cdot \frac{sinr}{m}\big) \cdot x^{(\kappa+1)m-1} e^{-x} dx \\
&\overset{(b)}{=} \frac{1}{\Gamma[(\kappa+1)m] \cdot \ln 2} \sum_{\mu=0}^{(\kappa+1)m-1} \frac{[(\kappa+1)m-1]!}{[(\kappa+1)m-\mu-1]!} \Bigg[\frac{(-1)^{(\kappa+1)m-\mu-2}}{(\frac{sinr}{m})^{(\kappa+1)m-\mu-1}} \cdot e^{\frac{m}{sinr}} \cdot Ei(-\frac{m}{sinr}\big) + \\
&\qquad \sum_{i=1}^{(\kappa+1)m-\mu-1} (i-1)! \cdot (-\frac{m}{sinr})^{(\kappa+1)m-\mu-i-1} \Bigg].
\end{aligned} \tag{2.27}$$

where (a) follows when $\mu > 0$,

$$\int_0^\infty x^n e^{-\mu x} \ln x dx = \frac{n!}{\mu^{n+1}} \left[1 + \frac{1}{2} + \cdots + \frac{1}{n} - \mathbb{C} - \ln \mu \right],$$

with the *Euler-Mascheroni constant*

$$\mathbb{C} = \lim_{n \to \infty} \left(\sum_{k=1}^{n} \frac{1}{k} - \ln n \right) \approx 0.57721. \tag{2.30}$$

Finally, we examine the scaling laws for ergodic throughput capacity under intra-cell transmission mode. Because of $\kappa = \Theta(\frac{n}{b})$ (Lemma **??**) and $I = \Theta\big((\frac{n}{b})^{1-\frac{\alpha}{2}}\big)$ (Lemma 2.2.3), we have that, at low SINR the transmission rate is upper bounded by $\Theta(\frac{n}{b})$; similarly, from (2.29) we conclude that, at the regime of high SINR the transmission rate is upper bounded by $\Theta(\log(\frac{n}{b}))$. Here we utilize the alternative definition of *Euler-Mascheroni* constant,

$$\mathbb{C} = \lim_{\kappa \to \infty} \left(\sum_{i=1}^{(\kappa+1)m-1} \frac{1}{i} - \ln \big[(\kappa+1)m - 1 \big] \right). \tag{2.31}$$

Taking into account the temporal occupation $1 - \theta$ and bandwidth allocation ηW_1, the per-node ergodic throughput capacity $\bar{T}(n, b)$ is determined by the product between the allocated bandwidth and the transmission rate, i.e., $(1 - \theta) \cdot \eta W_1 \cdot \bar{R}$. Theorem 3 summarizes the scaling laws for the ergodic throughput capacity under intra-cell transmission mode $\bar{T}_{\text{intra}}(n, b)$ at low SINR and high SINR scenarios, respectively.

Theorem 3. *For a hybrid wireless network of n nodes and b base stations over Nakagami-m fading channels, if $b = o(\frac{n}{\log n})$, the per-node ergodic throughput capacity under the intra-cell transmission mode at low SINR is*

$$\bar{T}_{intra}^{low}(n, b) = O\left(\frac{n}{b} W_1 \right) \ bit/s. \tag{2.32}$$

The related per-node ergodic throughput capacity at high SINR is

$$\bar{T}_{intra}^{high}(n, b) = O\left(\log(\frac{n}{b}) W_1 \right) \ bit/s. \tag{2.33}$$

2.4.2 Ergodic Throughput Capacity under Infrastructure Mode

To investigate the ergodic throughput capacity under infrastructure mode, we mainly focus on the downlink phase. During the downlink phase, the interference cancellation strategy is not feasible, which results in the following ergodic throughput behavior:

$$\begin{aligned}
\bar{R}' &= \mathbf{E}\left\{ \log\left(1+\frac{P\cdot l(|X_b-X_j|)\cdot|h_{bj}|^2}{\lambda W_2 N_0+I'}\right)\right\} \\
&= \mathbf{E}\left\{ \log\left(1+|h_{bj}|^2\cdot sinr'\right)\right\} \\
&= \int_0^\infty \log(1+x\cdot sinr')\cdot\frac{m^m}{\Gamma(m)}x^{m-1}e^{-mx}dx \\
&= \frac{1}{\Gamma(m)\cdot\ln 2}\sum_{\mu=0}^{m-1}\frac{(m-1)!}{(m-\mu-1)!}\cdot\left[\frac{(-1)^{m-\mu-2}}{(\frac{sinr'}{m})^{m-\mu-1}}e^{\frac{m}{sinr'}}Ei(-\frac{m}{sinr'})+\right. \\
&\quad \left.\sum_{k=1}^{m-\mu-1}(k-1)!(-\frac{m}{sinr'})^{m-\mu-1-k}\right], \qquad (2.34)
\end{aligned}$$

where $sinr'=\frac{P\cdot min(1,\rho_{0d}^{-\alpha}e^{-\gamma\rho_{0d}})}{\lambda W_2 N_0+I'}$ and the pdf of $|h_{bj}|^2$ is given by (5.4).

Further, we explore the implication of (2.34) in both low SINR and high SINR scenarios. At low SINR, the transmission rate (2.34) is transformed into

$$\begin{aligned}
\bar{R}' &\approx \int_0^\infty \frac{sinr'}{\ln 2}x\cdot\frac{m^m}{\Gamma(m)}x^{m-1}e^{-mx}dx \\
&= sinr'\cdot\log_2^e; \qquad (2.35)
\end{aligned}$$

while, at the regime of high SINR, we obtain

$$\begin{aligned}
\bar{R}' &\approx \int_0^{\infty} \log\big(sinr' \cdot x\big) \frac{m^m}{\Gamma(m)} x^{m-1} e^{-mx} dx \\
&= \log(sinr') \cdot \frac{m^m}{\Gamma(m)} \int_0^{\infty} x^{m-1} e^{-mx} dx + \frac{m^m}{\Gamma(m) \cdot \ln 2} \int_0^{\infty} \ln x \cdot x^{m-1} e^{-mx} dx \\
&= \log(sinr') + \frac{1}{\Gamma(m) \cdot \ln 2} \left[\int_0^{\infty} \ln x \cdot x^{m-1} e^{-x} dx - \int_0^{\infty} \ln m \cdot x^{m-1} e^{-x} dx \right] \\
&= \log(\frac{sinr'}{m}) + \frac{1}{\Gamma(m) \cdot \ln 2} \int_0^{\infty} x^{m-1} e^{-x} \ln x dx \\
&= \log(\frac{sinr'}{m}) + \log_2^e \left[\big(1 + \cdots + \frac{1}{m-1}\big) - \mathbb{C} \right]. \qquad (2.36)
\end{aligned}$$

Clearly, at low SINR, the downlink transmission rate is $\Theta\big(\frac{n}{b}\big)$; while at high SINR, the downlink transmission rate is $\Theta(\log(\frac{1}{m} \cdot \frac{n}{b}))$. Taking into consideration the bandwidth limitation of downlink phase $\big(\Theta(\frac{b}{n} W_2)\big)$, the ergodic throughput capacity under the infrastructure transmission mode $\bar{T}_{\text{infra}}(n, b)$, which is bottlenecked by the downlink phase, is summarized as follows.

Theorem 4. *For a hybrid wireless network of n nodes and b base stations over Nakagami-m fading channels, if $b = o(\frac{n}{\log n})$, the per-node ergodic throughput capacity under the infrastructure transmission mode at low SINR is*

$$\bar{T}_{infra}^{low}(n, b) = \Theta\big(W_2\big) \ bit/s. \qquad (2.37)$$

The related per-node ergodic throughput capacity at high SINR is

$$\bar{T}_{infra}^{high}(n, b) = \Theta\left(\frac{b}{n} \log(\frac{1}{m} \cdot \frac{n}{b}) W_2 \right) \ bit/s. \qquad (2.38)$$

Finally, the Monte Carlo simulation is provided to verify the effectiveness of the derived theoretical bounds. Here we take the opportunistic nodes $\kappa = 49$ as an example. Figure 2.6 clearly illustrates the excellent agreement between the simulation result and the analytical results of the ergodic capacity at low SINR (2.28) and high SINR regions (2.29), respectively.

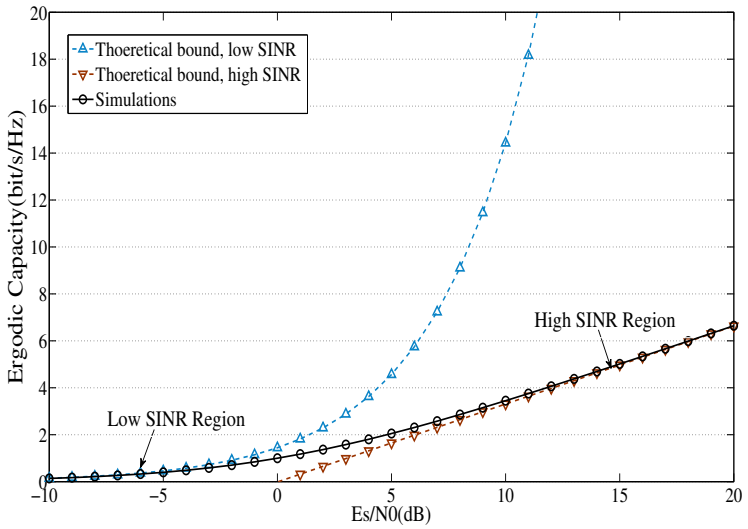

Figure 2.6. Ergodic capacity over Nakagami-m fading channel ($\kappa = 49$).

To further illustrate the asymptotic behaviors of the derived ergodic throughput capacity, in Figure 2.7 we compare the uplink ergodic throughput capacity with the downlink scenario under infrastructure mode. When the SINR is low (5 dB), the Nakagami-m shape parameter will not take effect, which is reduced to the AWGN scenario. However, the advantage of introducing opportunistic sources is very obvious. Similarly, at high SINR (15 dB), the uplink throughput overwhelmingly exceeds the downlink scenario as the opportunistic nodes κ increase. In particular, with m increasing, the *harmonic series* $\sum_{n=1}^{k} \frac{1}{n} \sim \ln^k + \mathbb{C}$. Therefore, large m closes the gap between the the uplink ergodic throughput capacity and downlink ergodic throughput capacity as shown in Figure 2.7.

2.5 QoS Performance Analysis for Hybrid Wireless Networks

The hybrid wireless networks are expected to provide the QoS guarantees [27] [28]. In this study, we define the QoS requirements in terms of the per-node average

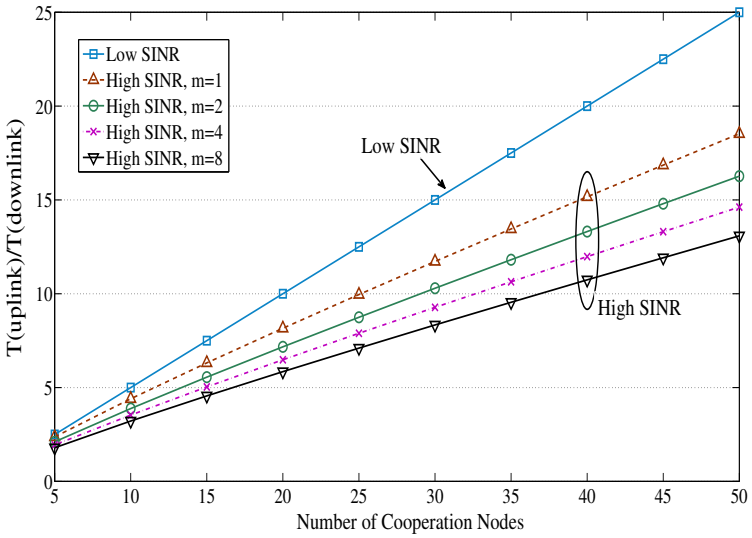

Figure 2.7. Ratio between uplink ergodic throughput capacity and downlink ergodic throughput capacity under infrastructure mode.

error probability (AEP). With AWGN channels, the instantaneous error probability (IEP) depends on the receiver SINR (or equivalently γ_s); while over fading channels, γ_s is a random variable with distribution $f(\gamma_s)$, and thus the instantaneous error probability $P(\gamma_s)$ is also random. Hence, in the fading scenario we introduce the AEP ($\bar{P}_s$) as the performance criterion, which is the average probability of symbol error over the distribution of γ_s:

$$\bar{P}_s = \int_0^\infty P(\gamma_s) f(\gamma_s) d\gamma_s. \tag{2.39}$$

2.5.1 AEP Performance under Intra-cell Transmission Mode

First, let us discuss the per-node AEP performance under intra-cell transmission mode. We take BPSK modulation as an example. As is known, the error probability for BPSK is $Q\left(\sqrt{2\gamma_b}\right)$ (for BPSK, $\gamma_b = \gamma_s$). Since $||\mathbf{h}||^2$ is Gamma-

distributed under intra-cell transmission mode (2.15), γ_b is also Gamma-distributed[10] $\gamma_b = \frac{P \cdot min(1, \rho_{0d}^{-\alpha} e^{-\gamma \rho_{0d}})}{W_1 N_0 + I} \cdot ||\mathbf{h}||^2$. Therefore, we obtain

$$f(\gamma_b) = \frac{m^{(\kappa+1)m}}{\Gamma[(\kappa+1)m] \cdot \bar{\gamma_b}^{(\kappa+1)m}} \gamma_b^{(\kappa+1)m-1} e^{-m\gamma_b/\bar{\gamma_b}}, \tag{2.40}$$

where $\bar{\gamma_b}$ is the average per-symbol SINR .

We develop the analytical expression for AEP under intra-cell transmission mode as

$$\begin{aligned}
\bar{P_b} &= \int_0^\infty Q\big(\sqrt{2\gamma_b}\big) \frac{m^{(\kappa+1)m}}{\Gamma[(\kappa+1)m] \cdot \bar{\gamma_b}^{(\kappa+1)m}} \cdot \gamma_b^{(\kappa+1)m-1} e^{-\frac{m\gamma_b}{\bar{\gamma_b}}} d\gamma_b \\
&\overset{(a)}{=} \int_0^\infty \frac{1}{\sqrt{2\pi}} e^{-\frac{t^2}{2}} \left[\int_0^{\frac{t^2}{2}} \frac{m^{(\kappa+1)m}}{\Gamma[(\kappa+1)m] \cdot \bar{\gamma_b}^{(\kappa+1)m}} \cdot x^{(\kappa+1)m-1} e^{-\frac{mx}{\bar{\gamma_b}}} dx \right] dt \\
&\overset{(b)}{=} \int_0^\infty \frac{1}{\sqrt{2\pi}} e^{-\frac{t^2}{2}} \cdot \frac{m^{(\kappa+1)m}}{\Gamma[(\kappa+1)m] \cdot \bar{\gamma_b}^{(\kappa+1)m}} \cdot \left(\frac{m}{\bar{\gamma_b}}\right)^{-(\kappa+1)m} \cdot \gamma\left((\kappa+1)m, \frac{m}{2\bar{\gamma_b}} t^2\right) dt \\
&\overset{(c)}{=} \int_0^\infty \frac{1}{\sqrt{2\pi}} e^{-\frac{t^2}{2}} \left[1 - e^{-\frac{m}{2\bar{\gamma_b}} t^2} \left(\sum_{i=0}^{(\kappa+1)m-1} \frac{(\frac{m}{2\bar{\gamma_b}} t^2)^i}{i!} \right) \right] dt \\
&\overset{(d)}{=} \frac{1}{2} - \sum_{i=0}^{(\kappa+1)m-1} \frac{(\frac{m}{2\bar{\gamma_b}})^i}{\sqrt{2\pi} \cdot i!} \cdot \frac{(2i-1)!!}{2(1+\frac{m}{\bar{\gamma_b}})^i} \cdot \sqrt{\frac{\pi}{\frac{1}{2}(1+\frac{m}{\bar{\gamma_b}})}} \\
&\overset{(e)}{=} \frac{1}{2} \left[1 - \sum_{i=0}^{(\kappa+1)m-1} \binom{2i}{i} \beta \left(\frac{1-\beta}{2}\right)^i \left(\frac{1+\beta}{2}\right)^i \right]
\end{aligned} \tag{2.41}$$

where at (a) we use the definition of Q-function and change the order of integration; (b) follows the definition of incomplete gamma function; (c) follows that for integer n, $\gamma(n,x) = (n-1)!\big[1 - e^{-x} \sum_{i=0}^{n-1} \frac{x^i}{i!}\big]$ and $\Gamma(n) = (n-1)!$; (d) follows $\int_0^\infty x^{2n} e^{-px^2} dx = \frac{(2n-1)!!}{2(2p)^n} \sqrt{\frac{\pi}{p}}$ and (e) is simplified by $(2n-1)!! = \frac{2n!}{2^n n!}$ and $\beta = \sqrt{\frac{\bar{\gamma_b}}{m+\bar{\gamma_b}}}$.

[10] Similar approximation is introduced in (2.12) and (2.26) for analysis simplicity.

Employing the *chernoff* bound $Q(x) \leq \frac{1}{2}e^{-\frac{x^2}{2}}$, we derive a relaxed upper bound for the above AEP performance

$$\begin{aligned} \bar{P}_b &\leq \int_0^{\infty} \frac{1}{2} e^{-\gamma_b} \frac{m^{(\kappa+1)m}}{\Gamma[(\kappa+1)m] \cdot \bar{\gamma_b}^{(\kappa+1)m}} \, d\gamma_b \\ &= \frac{1}{2}\left(1 + \frac{\bar{\gamma_b}}{m}\right)^{-(\kappa+1)m}. \end{aligned} \tag{2.42}$$

2.5.2 AEP Performance under Infrastructure Transmission Mode

Further, we investigate the AEP performance under infrastructure transmission mode. Apparently, the uplink traffics are similar to the traffics in the intra-cell transmission mode and thus the average error probability for uplink traffics under infrastructure transmission mode $\bar{P}_b^{Up} = \bar{P}_b$.

The AEP performance for the downlink phase is

$$\bar{P}_b^{Down} = \frac{1}{2}\left[1 - \sum_{i=0}^{m-1} \binom{2i}{i} \beta \left(\frac{1-\beta}{2}\right)^i \left(\frac{1+\beta}{2}\right)^i\right]. \tag{2.43}$$

Due to the space limitation, we omit the details of derivation, which is similar to the derivation of the AEP performance for the uplink phase.

With the uplink and downlink average error probability, we obtain the overall AEP performance for infrastructure transmission mode as follows:

$$\begin{aligned} \bar{P}_b' &= 1 - (1 - \bar{P}_b^{Up})(1 - \bar{P}_b^{Down}) \\ &= \bar{P}_b^{Up} + \bar{P}_b^{Down} - \bar{P}_b^{Up} \cdot \bar{P}_b^{Down}. \end{aligned} \tag{2.44}$$

Besides, to further illustrate the bottleneck of the infrastructure mode, we present the upper bound of AEP during the downlink phase as

$$\begin{aligned} \bar{P}_b^{Down} &\leq \int_0^{\infty} \frac{1}{2} e^{-\gamma_b} \cdot \frac{m^m}{\Gamma(m) \cdot \bar{\gamma_b}^m} \gamma_b^{m-1} e^{-m\gamma_b/\bar{\gamma_b}} \, d\gamma_b \\ &= \frac{1}{2}\left(1 + \frac{\bar{\gamma_b}}{m}\right)^{-m}. \end{aligned} \tag{2.45}$$

Clearly, comparing the upper bound of the uplink AEP (2.42) with the downlink scenario (2.45), as κ increases the uplink average probability of error overwhelming exceeds the downlink performance, which further verified the benefit of introducing opportunistic sources, and thus the downlink phase becomes the bottleneck of the infrastructure mode.

2.6 Conclusions

In this chapter, we study the theoretical data transmission limits for hybrid wireless networks over fading channels. To overcome fading impairments, we introduce an optimal multiple access technique allowing opportunistic sources to transmit concurrently with the scheduled source. We first define the outage throughput capacity as the performance criteria for slow fading scenario. We prove that under intra-cell mode, the per-node outage throughput capacity over Nakagami-m fading is $O\big(\log[(\epsilon^{\frac{1}{m}})^{\frac{b}{n}}\frac{n}{b}]\,W_1\big)$; while under infrastructure mode, the related outage throughput capacity is $\Theta\big(\frac{b}{n}\log(\epsilon^{\frac{1}{m}}\frac{n}{b})\,W_2\big)$.

Further we specified the ergodic throughput capacity as the performance measurement for fast fading situation. We show that under intra-cell transmission mode, the ergodic throughput capacity is $O\big(\frac{n}{b}W_1\big)$ at low SINR and $O\big(\log(\frac{n}{b})W_1\big)$ at high SINR; while, under infrastructure transmission mode, the ergodic throughput capacity is derived as $\Theta\big(W_2\big)$ at low SINR and $\Theta\big(\frac{b}{n}\log(\frac{1}{m}\cdot\frac{n}{b})\,W_2\big)$ at high SINR, respectively.

Finally presented is the QoS performance analysis in terms of the per-node AEP for hybrid wireless network. It is concluded that, with opportunistic sources, the intra-cell mode effectively combats fading as wireless nodes increases; however, the infrastructure mode is bottlenecked by the downlink transmission since base station is the only transmitter in the cell during the downlink phase.

Chapter 3

Analysis and Improvement of the Voltage Regulation in Microgrid Based on Sensor Selection

In this chapter, we study the voltage regulation issue in microgrid, and appy WSANs to accurately monitor the real-time voltage level and coordinate the distributed energy resources (DERs) with the traditional voltage regulators. The remainder of this chapter is organized as follows. The system model and problem formulation are given in Section 3.1. In Section 3.2, aiming to improve the voltage measurement performance, we propose two sensor selection schemes: sensor selection under equal power allocation and optimal power allocation, respectively. We first propose an opportunistic sensor selection scheme under equal power allocation. Then we address sensor selection scheme under optimal power allocation and derive a reminiscent of "water-filling" solution. Section 3.3 illustrates the improvement of power efficiency using sensor selection. The discussion of improving the transmission rate based on sensor selection is provided in Section 3.4. We present some concluding remarks in Section 3.5. The Proof omitted from the body of the chapter is presented in Appendix.

3.1 System Model and Problem Formulation

3.1.1 System Model

Integration of DERs into microgrid makes the power supply more reliable, whereas it also poses a challenge to voltage regulation (See Figure 3.1). Without reasonable coordinations, the voltage is not stable after introducing the DERs.

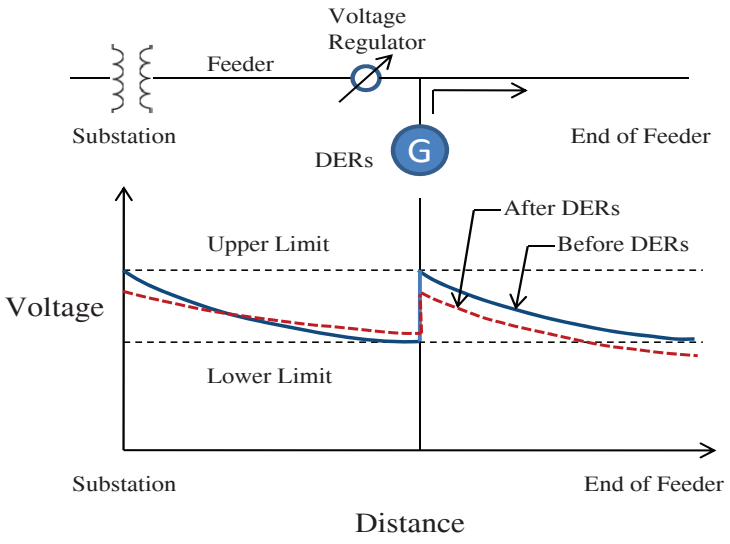

Figure 3.1. Impact of the DERs on voltage regulation.

To avoid significant voltage perturbations, control center need to keep the secondary bus voltage V constant within the range [34]

$$V_{LB} \leq V \leq V_{UB} \tag{3.1}$$

where

$$\begin{aligned} V_{LB} &= V_{set} - 0.5V_{DB} \\ V_{UB} &= V_{set} + 0.5V_{DB}. \end{aligned}$$

V_{set} is the set point voltage and V_{DB} is the dead band (the band where no actions occurs to prevent oscillations and repeated activation-deactivation cycle "hunting").

To maintain the voltage level and coordinate the DERs with the traditional voltage regulators in microgrid, a group of voltage sensors $\{S_1, S_2, \cdots, S_m\}$ is deployed to monitor the real-time voltage state and detect the load fluctuation. The system model is shown in Figure 4.1. Each voltage sensor S_i is able to periodically measure

the voltage level θ.[1] The measurement at each voltage sensor should be a noise-corrupted version of voltage source θ:

$$u_i = \theta + \nu_i, \tag{3.2}$$

where ν_i is the noise introduced at each sensor. We assume that the source θ is a random variable with mean m_θ and variance σ_θ^2. Since the voltage sensor are geographically distributed, we further assume that ν_i are independent and identically distributed (*i.i.d.*) random variables with zero mean and variance σ_i^2.

After collecting the information about the voltage, each sensor transmits the observation directly to the control center without any coding. This strategy is referred to as *analog amplify and forward* [53]. The analog amplify-and-forward strategy is motivated by the well-known results shown in [53] [54] that if sensor statistics are Gaussian, a simple uncoded (analog) amplify-and-forward technique dramatically outperforms the separate source-channel coding approach. Specifically, the analog amplify-and-forward technique was proved to be asymptotically optimal in [53], and exactly optimal in [54] for sensors communicating to a control center over a multi-access channel. Distributed estimation based on the analog amplify-and-forward has been extensively studied [55]-[59].

Therefore, at the voltage sensor i, the transmitter can be simply modeled by a power amplifying factor a_i and thus the average transmit power is given as

$$P_i = a_i P_{u_i} = a_i(\sigma_\theta^2 + \sigma_i^2), \tag{3.3}$$

where P_{u_i} denotes the power of observation u_i.

[1]The practical scenario we consider in this chapter is two or more DERs may need to monitor the voltage at one point in order to take control actions (increasing or deceasing their voltage) since their control actions are coupled in the voltage dynamics.

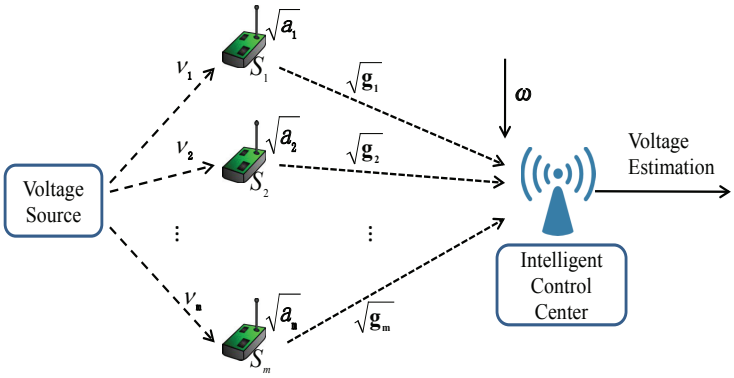

Figure 3.2. System model.

3.1.2 Multiple Access Scheme

In this study, instead of assuming a coherent multiple access scheme, we adopt the *orthogonal* access scheme as the multiple access scheme between the voltage sensors and the ICC. The main motivation for employing orthogonal multiple-access schemes, such as FDMA, is the removal of the requirement on the carrier-level synchronization among sensors. In this case, each voltage sensor transmits its measurement to the ICC via orthogonal channels, and the ICC receives

$$\begin{aligned} y_i &= \sqrt{g_i a_i}(\theta + \nu_i) + w_i \\ &= h_i \theta + n_i \qquad\qquad i = 1, 2, \ldots, m, \end{aligned} \tag{3.4}$$

where g_i is the power gain of the fading channel and w_i with variance ξ_i^2 denotes the noise introduced at ICC. For simplification, we use h_i to represent $\sqrt{g_i a_i}$ in (3.4).

We assume that both the transmitter and receiver have the fading channel state information. [2] Clearly, the received signal vector is

$$\mathbf{y} = \mathbf{h}\theta + \mathbf{n} \tag{3.5}$$

where $\mathbf{h} = [\sqrt{a_1 g_1}, \ldots, \sqrt{a_m g_m}]^T$ and $\mathbf{n}$ stands for AWGN with diagonal covariance matrix $\mathbf{R}$ given by $diag[\mathbf{R}] = [\sigma_1^2 a_1 g_1 + \xi_1^2, \ldots, \sigma_m^2 a_m g_m + \xi_m^2]^T$.

Finally, ICC fuses these local measurements to produce a global estimate of the voltage $\hat{\theta}$ to recover θ. In this work, we adopt the maximum likelihood (ML) estimator [60]

$$\begin{aligned} \hat{\theta} &= [\mathbf{h}^T \mathbf{R}^{-1} \mathbf{h}]^{-1} \mathbf{h}^T \mathbf{R}^{-1} \mathbf{y} \\ &= \left(\sum_{i=1}^{m} \frac{a_i g_i}{\sigma_i^2 a_i g_i + \xi_i^2} \right)^{-1} \sum_{i=1}^{m} \frac{\sqrt{a_i g_i} y_i}{\sigma_i^2 a_i g_i + \xi_i^2}. \end{aligned} \tag{3.6}$$

The related Mean Square Error (MSE) of this estimator is

$$D_{orth} = [\mathbf{h}^T \mathbf{R}^{-1} \mathbf{h}]^{-1} = \left(\sum_{i=1}^{m} \frac{a_i g_i}{\sigma_i^2 a_i g_i + \xi_i^2} \right)^{-1}. \tag{3.7}$$

According to the voltage estimation, ICC could turn on/off the related DERs and voltage regulators to stabilize the power supply and avoid significant voltage perturbations in microgrid. [3]

[2] This is a reasonable assumption in smart grid, in which the channel gain does not change dramatically, since the sensors and control center are relatively fixed and the channel gain in this case will change gradually and slowly.

[3] Due to the space limitation, we mainly discuss the orthogonal access scheme in this chapter. However, an extension is straightforward considering the coherent multiple access scheme, which requires perfect carrier-level synchronization among voltage sensors.

3.1.3 Lower Bound of MSE

If all voltage sensor measurements are directly available to the control center, we could get the following estimator

$$\theta_0 = \left(\sum_{i=1}^{m} \frac{1}{\sigma_i^2}\right)^{-1} \left(\sum_{i=1}^{m} \frac{x}{\sigma_i^2}\right), \tag{3.8}$$

which achieves the distortion

$$D_0 = \left(\sum_{i=1}^{m} \frac{1}{\sigma_i^2}\right)^{-1}. \tag{3.9}$$

This theoretical result could serve as the performance benchmark for later analysis.

3.1.4 Problem Formulation

Based on the above analysis, the power consumption of each voltage sensor is provided by (3.3) and the related voltage estimation distortion is given in (3.7). Now we have three objectives:

1. Minimize the estimation distortion to improve the voltage estimation accuracy;
2. Minimize the power consumption to prolong the voltage sensor lifetime;
3. Maximize the transmission rate to guarantee the real-time communication between the voltage sensors and the control center.

In the following sections, several sensor selection schemes are proposed to accomplish these goals.

3.2 Improving the Voltage Estimation Accuracy Using Sensor Selection

3.2.1 Sensor Selection Scheme under Equal Power Allocation

In this section, we aim to minimize the voltage estimation distortion using sensor selection. Our strategy is first to select K ($\leq m$) "*opportunistic*" sensors with the favorable channel conditions (without power consideration):

$$\begin{aligned} min \qquad & \left(\sum_{i=1}^{m} z_i \frac{g_i}{\sigma_i^2 g_i + \xi_i^2} \right)^{-1} \\ s.t. \qquad & \boldsymbol{1}^T \boldsymbol{z} = K \\ & z_i \in \{0, 1\}. \end{aligned} \tag{3.10}$$

where z_i is the variable to optimize. The vector $\boldsymbol{1}$ is a vector with all entries one and the element z_i of vector $\boldsymbol{z}$ can be chosen from 0 or 1, which determines whether the ith voltage sensor is selected or not. However, the above problem, which is an integer optimization problem, is nonconvex and hard to solve. Therefore, we relax the nonconvex constraint $z_i \in \{0, 1\}$ with the convex constraint $0 \leq z_i \leq 1$, and formulate the following *relaxed* sensor selection problem:

$$\begin{aligned} max \qquad & \sum_{i=1}^{m} z_i \frac{g_i}{\sigma_i^2 g_i + \xi_i^2} + \gamma \big(\log(z_i) + \log(1 - z_i) \big) \\ s.t. \qquad & \boldsymbol{1}^T \boldsymbol{z} = K, \end{aligned} \tag{3.11}$$

where γ is a positive parameter controlling the quality of approximation.

Next, solving the above convex optimization problem (3.11), we could obtain the target sensors. Here, our principle is to choose the K voltage sensors with largest z_i weightness, which means only "strong" sensors with the best channel conditions participate in the voltage estimation process.

Finally, the power need to be allocated in a reasonable way due to the total power constraint P_{tot}. In this subsection, we apply the equal power allocation strategy;

sensor selection under optimal power allocation will be discussed later. Clearly, the equal power allocation strategy is

$$a_i(\sigma_\theta^2 + \sigma_i^2) = \frac{P_{tot}}{K} \qquad 1 \leq i \leq K. \tag{3.12}$$

Further, applying the equal power allocation strategy (3.12) into (3.7), we could derive the analytical voltage estimation distortion under equal power allocation:

$$D_{orth} = \left(\sum_{i=1}^{m} t_i \frac{P_{tot} g_i}{\sigma_i^2 P_{tot} g_i + K \xi_i^2 (\sigma_\theta^2 + \sigma_i^2)} \right)^{-1}, \tag{3.13}$$

where t_i $\left(t_i \in \{0, 1\}\right)$ represents the final sensor selection decision. The proposed opportunistic sensor selection scheme under equal power allocation is summarized by Algorithm 1.

Algorithm 1 Opportunistic Sensor Selection Scheme

1: Formulate the relaxed sensor selection problem without power constraint (3.11);
2: Solve the optimization problem and obtain the target voltage sensors t_i;
3: Activate the K selected voltage sensors. Only active sensors participate in the voltage estimation process;
4: K active sensors adjust their transmit power according to (3.12) and send the voltage measurements to ICC;
5: ICC adopts ML estimator to recover the voltage level θ.

Let us discuss the following asymptotic behaviors.

Remark 3.1.1. $P_{tot} \to \infty$

Under equal power allocation, as the total power P_{tot} approaches infinity, we conclude $D_{orth} \to D_0$. This conclusion suggests that even if the power approaches infinity, the distortion only achieves the performance benchmark D_0, instead of approaching zero. One possible reason is that the observation noise ν_i could not be

eliminated even if the power approaches infinity. Once the collected signal is amplified at each transmitter, the observation noise ν_i is amplified inevitably as well.

Remark 3.2.1. $K \to \infty$

As the selected voltage sensor number K approaches infinity, we obtain the following asymptotic behavior:[4]

$$\begin{aligned} D_{orth} &\sim \Big[\frac{1}{K}\sum_{i=1}^{K}\frac{P_{tot}g_i}{\xi_i^2(\sigma_\theta^2+\sigma_i^2)}\Big]^{-1} \\ &= \frac{E\Big[\frac{\xi_i^2(\sigma_\theta^2+\sigma_i^2)}{g_i}\Big]}{P_{tot}}. \end{aligned} \tag{3.14}$$

Therefore, as K increases, the voltage estimation error could not decrease to zero either. One can attribute this limitation to the fact that, under *orthogonal* access scheme, K different channel noises can not be eliminated even if K approaches infinity.

3.2.2 Sensor Selection Scheme under Optimal Power Allocation

In this part, we investigate the sensor selection scheme under optimal power allocation. According to the Problem Formulation in Section 3.1, the sensor selection scheme under optimal power allocation is formulated as

$$\begin{aligned} max \quad & \sum_{i=1}^{m}\frac{a_i g_i}{\sigma_i^2 a_i g_i+\xi_i^2} \\ s.t. \quad & \sum_{i=1}^{m} a_i(\sigma_\theta^2+\sigma_i^2) \le P_{tot} \\ & a_i \ge 0. \end{aligned} \tag{3.15}$$

Unlike the preassigned sensor number K in equal power allocation scenario, under optimal power allocation, the number of active voltage sensors could not be

[4] A similar result could be found in [56].

fixed in advance. Obviously, this problem is convex and a_i is the power allocation variable to optimize. The Lagrangian G is given as

$$G = -\sum_{i=1}^{m} \frac{a_i g_i}{\sigma_i^2 a_i g_i + \xi_i^2} + \lambda \left[\sum_{i=1}^{m} a_i(\sigma_\theta^2 + \sigma_i^2) - P_{tot}\right] - \sum_{i=1}^{m} \mu_i a_i. \quad (3.16)$$

Traditionally, numerical optimization methods, such as subgradient and interior point algorithms could be employed to solve the above optimization problem. However, these traditional methods require iterative calculations and can only numerically achieve the optimal solution (i.e., no closed-form solution is achieved). Therefore, to derive the closed- form solutions, we develop the following Karush-Kuhn-Tucker (KKT) conditions [61]:

$$\begin{aligned}
\frac{\partial G}{\partial a_i} = -\frac{g_i \xi_i^2}{(\sigma_i^2 a_i g_i + \xi_i^2)^2} + \lambda(\sigma_\theta^2 + \sigma_i^2) - \mu_i &= 0 \\
\lambda \left(\sum_{i=1}^{m} a_i(\sigma_\theta^2 + \sigma_i^2) - P_{tot}\right) &= 0 \\
\mu_i a_i &= 0 \\
\lambda &\geq 0 \\
\mu_i &\geq 0 \\
a_i &\geq 0.
\end{aligned}$$

Solving the KKT conditions, we obtain the reminiscent "water-filling" solutions in wireless communications,

$$a_i = \frac{\xi_i^2}{\sigma_i^2 g_i}\left(\sqrt{\frac{g_i}{\lambda \xi_i^2(\sigma_\theta^2 + \sigma_i^2)}} - 1\right)^+, \quad (3.17)$$

where x^+ equals to 0 when x is less than zero, and otherwise equals to x. The solution is derived in Appendix C. For voltage sensor i with $\eta_i = \frac{g_i}{\xi_i^2(\sigma_\theta^2+\sigma_i^2)}$, if $\eta_i > \lambda$, the corresponding sensor will be active; otherwise the corresponding sensor will be switched off for power efficiency.

To practically implement the proposed sensor selection scheme, we need to split the transmission time τ into two sections. The first section consumes a fraction $\theta \in [0, 1]$ of τ and is used to select the target voltage sensors and inform every selected sensor. The second section of $(1 - \theta)\tau$ is for the selected voltage sensors to transmit the measurements to the control center.

3.2.3 Voltage Estimation Performance with Different Sensor Selection Schemes

The voltage estimation performance of our proposed sensor selection schemes is evaluated. In the following simulations, 100 voltage monitoring sensors are deployed in microgrid and the power of the voltage source is set as $\sigma_\theta^2 = 1mW$. To simulate the practical communication environment in microgrid, we assume the channel follows Rayleigh fading, a typical fading scenario. Figure 3.3 demonstrates the voltage estimation performance with different sensor selection schemes.

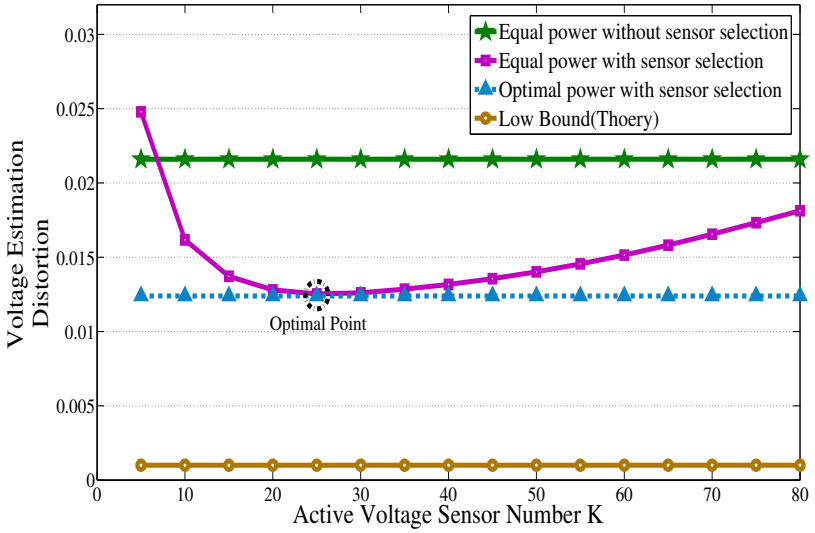

Figure 3.3. Voltage estimation performance with different sensor selection schemes.

First, let us examine the voltage estimation performance of our proposed opportunistic sensor selection scheme under equal power allocation. Note that the proposed sensor selection scheme is not valid unless at least 10 voltage sensors are selected from the whole 100 available sensors. This conclusion implies if too few sensors are selected per time, the information collected at the selected sensors is not enough for the control center to make an accurate voltage estimation. Besides, if too many sensors ($K \geq 40$ in this case) are selected, the voltage estimation performance also degrades. One intuitive explanation is that if too many sensors are selected, under equal power allocation, voltage sensors with good channel conditions could not be assigned with enough power, which definitely impairs the estimation performance. Therefore, selecting proper number of sensors could improve the voltage estimation performance. This conclusion is further illustrated in Figure 3.4. Meanwhile, Figure 3.4 shows that more power budget always brings better voltage estimation performance.

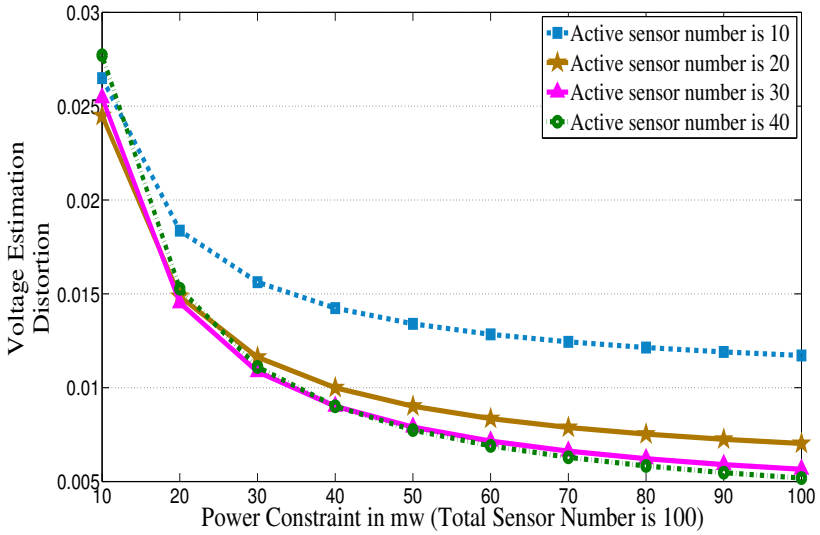

Figure 3.4. Voltage estimation performance with different power constraint.

Further, we compare the voltage estimation performance of our proposed sensor selection schemes under equal power allocation and optimal power allocation. As illustrated in Figure 3.3, sensor selection under optimal power allocation always outperforms the sensor selection scheme under equal power allocation. The improvement from the optimal power allocation scheme comes with the price of more complex computation. Quite interestingly, if proper number of voltage sensors ("optimal point") are selected, the equal power allocation scheme could even achieve the estimation performance of optimal power allocation scheme. This conclusion verifies the merit and validity of our proposed opportunistic sensor selection algorithm in Part A. However, due to the power constraint and limited available sensors, the voltage estimation performance could not approach the theoretical bound D_0.

3.3 Improving the power efficiency using sensor selection

In this section, we turn our attention to the second objective, namely, minimizing the power consumption using sensor selection. We first consider the power consumption of the proposed sensor selection under equal power allocation. Transforming the analytical distortion result (3.13), we derive

$$\sum_{i=1}^{m} \frac{K t_i \xi_i^2 (\sigma_\theta^2 + \sigma_i^2)/\sigma_i^2}{\sigma_i^2 P_{tot} g_i + K \xi_i^2 (\sigma_\theta^2 + \sigma_i^2)} = \sum_{i=1}^{m} \frac{t_i}{\sigma_i^2} - \frac{1}{D}, \tag{3.18}$$

where K represents the selected voltage sensor number and t_i is the sensor selection decision as explained in Part A of Section III. Solving the equation (3.18), the power consumption $Ptot$ could be obtained for the given voltage estimation distortion D.

Further, substituting $K = m$ and $t_i = 1$ in (3.18), we achieve the power consumption for the scenario of equal power allocation without sensor selection, which is actually a special case of the equal power allocation using sensor selection.

Finally, to optimally allocate the power, we formulate the following optimization problem to minimize the total power consumption subject to a given estimation distortion D.

$$\begin{aligned} min \qquad & \sum_{i=1}^{m} a_i'(\sigma_\theta^2 + \sigma_i^2) \\ s.t. \qquad & \Big(\sum_{i=1}^{m} \frac{a_i' g_i}{\sigma_i^2 a_i' g_i + \xi_i^2} \Big)^{-1} \leq D \\ & a_i' \geq 0. \end{aligned}$$

The first constraint is equivalent to

$$\sum_{i=1}^{m} \frac{\xi_i^2/\sigma_i^2}{\sigma_i^2 a_i' g_i + \xi_i^2} \leq \Big(\sum_{i=1}^{m} \frac{1}{\sigma_i^2} - \frac{1}{D} \Big). \tag{3.19}$$

For simplicity, let C denote the right-side part of (3.19) $\sum_{i=1}^{m} \frac{1}{\sigma_i^2} - \frac{1}{D}$. This problem is obviously convex and a_i' is the variable to optimize. The Lagrangian G' is given by

$$G' \;=\; \sum_{i=1}^{m} a_i'(\sigma_\theta^2 + \sigma_i^2) + \lambda' \big[\sum_{i=1}^{m} \frac{\xi_i^2/\sigma_i^2}{\sigma_i^2 a_i' g_i + \xi_i^2} - C \big] - \sum_{i=1}^{m} \mu_i' a_i'. \tag{3.20}$$

Implementing the KKT conditions, the optimal power allocation scheme for power efficiency is derived as

$$a_i' = \frac{\xi_i^2}{\sigma_i^2 g_i} \Bigg(\sqrt{\frac{\lambda' g_i}{\xi_i^2(\sigma_\theta^2 + \sigma_i^2)}} - 1 \Bigg)^+, \tag{3.21}$$

where λ' is

$$\sqrt{\lambda'} = \frac{\sum_{i=1}^{K''} \sqrt{\frac{\xi_i^2(\sigma_\theta^2 + \sigma_i^2)}{g_i \sigma_i^4}}}{\sum_{i=1}^{K''} \frac{1}{\sigma_i^2} - \frac{1}{D}}. \tag{3.22}$$

The number of active sensor number K'' can be solved if we substitute λ' back to (3.21). Now the optimal strategy is to activate the corresponding voltage sensor if the sensor index $1 \leq i \leq K''$, and switch off the sensor for all $i > K''$. Due to the space limitation, we omit the details about the solution of (3.21) which is similar to the derivation of (3.17).

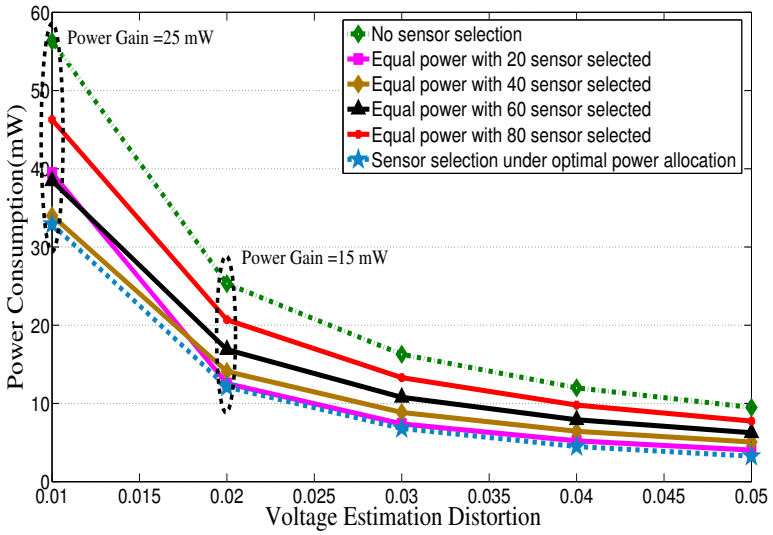

Figure 3.5. Power efficiency with different sensor selection schemes.

We provide the simulation to illustrate the power efficiency with different sensor selection schemes. We use the same simulation setup as Section III. Clearly from Figure 3.5, we conclude that the sensor selection scheme under optimal power allocation always comes with the minimum power consumption. When the voltage estimation distortion is required as 0.01, the optimal power allocation scheme saves nearly 25 mW compared to no-sensor-selection scheme; while the estimation distortion is set as 0.02, the optimal power allocation scheme saves more than 50% of power consumption (15 mW). Besides, we observe that if proper voltage sensors are selected, the sensor selection scheme under equal power allocation could approach the performance of optimal power allocation. This conclusion further verifies the advantage of our proposed opportunistic sensor selection scheme.

3.4 Improving the Throughput Transmission Rate Based on Sensor Selection

As is known, the channel capacity dictates the maximum data rates that can be transmitted over wireless channels with asymptotically small error probability. The wireless communication link should convey the voltage level information from the voltage sensors to the ICC with negligible error in a real-time manner. Therefore, in this section, we study the sensor selection schemes from the perspective of throughput transmission rate. We mainly investigate the joint power and spectrum allocation strategies to maximize the throughput transmission rate based on voltage sensor selection.

Therefore, our aim is to select the optimal [5] voltage sensors to maximize the transmission rate between the voltage sensors and the control center. From the information theory point of view, the maximum achievable rate of reliable communication is defined as [62]

$$C = B \cdot \log\left(1 + |h|^2 \cdot SNR\right) \quad bits/s, \tag{3.23}$$

where h characterizes the fading channel, SNR represents the signal-to-noise ratio and B denotes the assigned bandwidth.

Specifically, from the perspective of throughput transmission rate, the objective function to optimize is

$$x_i \cdot \log\left(1 + \frac{p_i \cdot g_i}{x_i \cdot N_0}\right) \quad bit/s, \tag{3.24}$$

where g_i is the channel gain, p_i denotes the power allocation variable and x_i represents the spectrum occupation variable.

[5] The "optimality" is mainly defined from the sum-rate perspective. The fairness and efficiency of such strategy go beyond the scope of this section.

3.4.1 Joint Power and Spectrum Allocation Strategy without Individual Power Constraint

First, we investigate the joint power and spectrum allocation without individual power constraint. We assume that there are totally m voltage sensors available. Therefore, with the spectrum constraint $\sum_{i=1}^{m} x_i \leq 1$ and the total power constraint $\sum_{i=1}^{m} p_i \leq P_{tot}$, the optimization problem can be formulated as follows.[6]

$$\begin{aligned} \max \quad & \sum_{i=1}^{m} x_i \cdot \ln\left(1+\frac{p_i \cdot g_i}{x_i \cdot N_0}\right) \\ s.t. \quad & x_i \geq 0 \\ & p_i \geq 0 \\ & \sum_{i=1}^{m} x_i - 1 = 0 \\ & \sum_{i=1}^{m} p_i - P_{tot} = 0 \end{aligned} \tag{3.25}$$

Further, the related Lagrangian function is given as

$$\begin{aligned} G''' \;=\; & -\sum_{i=1}^{m} x_i \ln\left(1+\frac{p_i \cdot g_i}{x_i \cdot N_0}\right) - \sum_{i=1}^{m} \beta_i x_i - \sum_{i=1}^{m} \lambda_i p_i \\ & +\mu\left(\sum_{i=1}^{m} x_i - 1\right) + \upsilon\left(\sum_{i=1}^{m} p_i - P_{tot}\right). \end{aligned} \tag{3.26}$$

From the Lagrangian function G''', we can derive the following Karush-Kuhn-Tucker (KKT) conditions:

$$-\ln\left(1+\frac{p_i \cdot g_i}{x_i \cdot N_0}\right) - x_i \cdot \frac{-\frac{p_i \cdot g_i}{x_i^2 \cdot N_0}}{1+\frac{p_i \cdot g_i}{x_i \cdot N_0}} - \beta_i^* + \mu^* = 0 \tag{3.27}$$

$$-x_i \cdot \frac{-\frac{g_i}{x_i \cdot N_0}}{1+\frac{p_i \cdot g_i}{x_i \cdot N_0}} - \lambda_i^* + \upsilon^* = 0 \tag{3.28}$$

$$\beta_i^* \cdot x_i = 0 \tag{3.29}$$

$$\lambda_i^* \cdot p_i = 0 \tag{3.30}$$

Lemma 3.4.1. *If A is the selected voltage sensor set, then we obtain $|A| = 1$.*

[6] In the sequel, we replace log with ln for simplicity.

Proof. We first simplify the KKT conditions with introducing $SNR_i = \frac{p_i \cdot g_i}{x_i \cdot N_0}$, and thus obtain

$$\ln(1 + SNR_i) - \frac{SNR_i}{1 + SNR_i} = \mu^*. \tag{3.31}$$

$$1 + SNR_i = \frac{g_i}{N_0 \cdot v^*}. \tag{3.32}$$

From the first SNR property (3.31), it is straightforward to prove that $f(x) = \ln(1 + x) + \frac{x}{1+x}$ is a monotonously increasing function. Therefore, the SNR of the signal received from all the voltage sensors should keep constant, since μ^* is a constant. Together with the second SNR property (3.32), we conclude that SNR_i is unique due to the fact that the channel g_i is randomly distributed. This conclusion means that only one voltage sensor should be selected per time to maximize the transmission rate. Therefore, $|A| = 1$ and we complete the proof. □

With $SNR_i = \frac{p_i \cdot g_i}{x_i \cdot N_0}$, it is obvious that large p_i yields large SNR_i. Therefore, in terms of the *power allocation strategy*, the selected voltage sensors should consume the whole power constraint P_{tot} to maximize the transmission rate.

Further, we investigate the *spectrum allocation strategy*. With the introduction of $\Gamma = \frac{P_{tot} \cdot g_i}{N_0}$, the transmission rate to maximize is thus

$$f(x) = x \cdot \ln\left(1 + \frac{\Gamma}{x}\right), \tag{3.33}$$

where x is the spectrum allocation variable. Obviously, we can obtain

$$f'(x) = \ln(1 + SNR) - \frac{SNR}{1 + SNR} \tag{3.34}$$

with $SNR = \frac{\Gamma}{x}$. From $f'(x) > 0$ with regard to $SNR > 0$, f(x) is also an increasing function. Therefore, the selected voltage sensor should occupy the whole spectrum.

3.4.2 Joint Power and Spectrum Allocation Strategy with Individual Power Constraint

In this part, we discuss the joint power and spectrum allocation with individual power constraint. The formulated problem is similar to (3.25), only with the introduction of individual power constraint $p_i \leq P_0$.

$$\begin{aligned} \max \quad & \sum_{i=1}^{m} x_i \cdot \ln\left(1 + \frac{p_i \cdot g_i}{x_i \cdot N_0}\right) \\ s.t. \quad & x_i \geq 0 \\ & p_i \geq 0 \\ & p_i \leq P_0 \\ & \sum_{i=1}^{m} x_i - 1 = 0 \\ & \sum_{i=1}^{m} p_i - P_{tot} = 0 \end{aligned} \tag{3.35}$$

From the Karush-Kuhn-Tucker (KKT) conditions, we obtain the following properties:

$$\ln(1 + SNR_i) - \frac{SNR_i}{1 + SNR_i} = \mu^* \tag{3.36}$$

$$1 + SNR_i = \frac{g_i}{N_0 \cdot (\alpha_i + v^*)} \tag{3.37}$$

$$\alpha_i \cdot (p_i - P_0) = 0 \tag{3.38}$$

Lemma 3.4.2 *With the individual and total power constraint, less than one voltage sensor is not assigned with full power.*

Proof. First, from the property (3.36), we conclude that the signal received from all the selected voltage sensors should keep constant SNR.

If the selected voltage sensor is not assigned with full power, $p_i < P_0$, we obtain $\alpha_i = 0$ from the KKT condition (3.38). Further, with the aid of property (3.37),

we conclude that SNR_i is unique, which means at most one voltage sensor is not assigned with full power. The proof is complete. □

With Lemma 3.4.2, in the following, Theorem 1 provides the joint power and spectrum allocation strategy for voltage sensors with individual power constraint.

Theorem 5. *The power allocation scheme for the selected voltage sensors follows a descending order according to the channel gain g_i; while for the selected voltage sensors with full power allocation, the spectrum allocation is proportional to the channel gain g_i.*

Proof. First of all, the signal received from all the selected voltage sensors should keep constant SNR, i.e.,

$$\frac{g_i}{N_0(\alpha_i + v^*)} = \frac{g_j}{N_0(\alpha_j + v^*)}. \tag{3.39}$$

Clearly, if $g_i > g_j$, we have $\alpha_i > \alpha_j$. Meanwhile, from Lemma 3.4.2, we have proved that at most one voltage sensor is not assigned with full power ($\alpha = 0$). Therefore, the voltage sensor with better channel condition, i.e., large g_i, should be assigned with full power.

In terms of the spectrum allocation strategy, we know that $SNR_i = \frac{P_0 \cdot g_i}{N_0 \cdot x_i}$ for the voltage sensor with full power allocation. With the fact that all selected voltage sensors keep constant SNR and $\sum_{i=1}^{m} x_i = 1$, we thus obtain

$$x_i = \frac{g_i}{\sum_{i=1}^{m} g_i}. \tag{3.40}$$

Therefore, the spectrum allocation is proportional to the channel gain g_i and we complete the proof. □

Finally, we evaluate the throughput performance of our proposed joint power and spectrum allocation strategy based on sensor selection. In this simulation, we

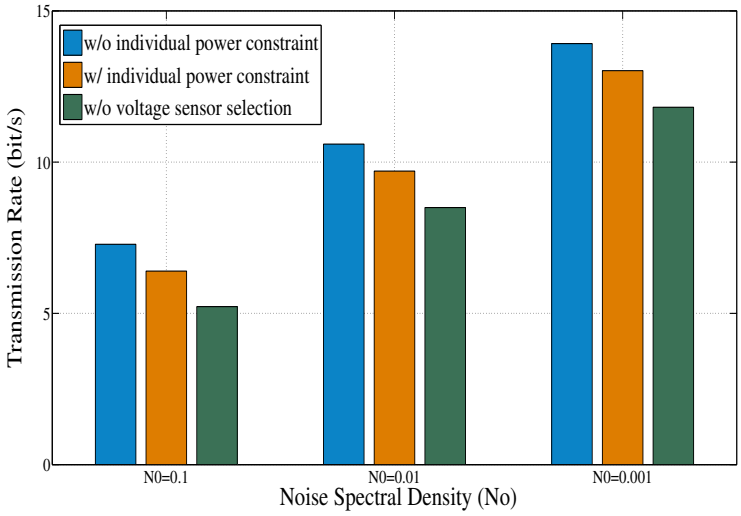

Figure 3.6. Transmission rate (bit/s) with different power and spectrum allocation strategies.

assume that there are 10 voltage sensors available. The total power constraint P_{tot} is 50 mW and the individual power constraint P_0 is set as 10 mW. To simulate the practical wireless communication environment, we also assume that the wireless channel follows Rayleigh fading. Clearly from Figure 3.6, we conclude that the joint power and spectrum allocation strategy without individual power constraint always provides the best transmission rate performance, since the individual power constraint (10 mW in this case) add one more constraint to the formulated optimization problem. To sum up, the proposed joint power and spectrum allocation strategy based on sensor selection outperforms the scenario without voltage sensor selection, which further demonstrates the validity and merits of sensor selection in improving the throughput transmission rate between the voltage sensors and the control center.

3.5 Conclusion

In this chapter, we have studied the voltage regulation issue in microgrid, and applied the WSANs to accurately monitor the real-time voltage level and coordinate DERs with the traditional voltage regulators. To achieve proper voltage regulation, several sensor selection schemes are proposed to improve the voltage measurement accuracy and power efficiency. An opportunistic sensor selection scheme under equal power allocation is first proposed to improve the voltage estimation performance. The asymptotic behaviors with the power constraint and the voltage sensor number approaching infinity are investigated. We have further addressed sensor selection scheme under optimal power allocation and derived a reminiscent of "water-filling" solution for this scenario. Besides, we illustrate the improvements on power efficiency employing the proposed sensor selection strategies. Finally, aiming to maximize the transmission rate between the voltage sensors and the control center, we heuristically proposed the joint power and spectrum allocation strategy based on voltage sensor selection. Numerical simulation results have demonstrated that our proposed sensor selection algorithms can efficiently regulate the voltage level and stabilize the power supply.

Chapter 4

Energy Management Strategy for Plug-in Hybrid Electric Vehicles Via Bidirectional Vehicle-to-Grid

In this chapter, we investigate the energy management strategies for plug-in hybrid electric vehicles (PHEVs) via bidirectional vehicle-to-grid (V2G). The remainder of this chapter is organized as follows. The system model is given in Section 4.1. We present an optimal energy management strategy to optimize the daily energy cost in Section 4.2. In Section 4.3, an optimal PHEV charging scheme is proposed to minimize the peak load and flatten the overall load profile. We provide some concluding remarks in Section 4.4. The proofs omitted from the body of the chapter are presented in Appendix.

4.1 System Model

4.1.1 Household Load Model

We characterize the local residential load with two components: a household base load (e.g. home electric appliances) and the load resulting from charging the PHEVs, as shown in Figure 4.1. In this work, we assume that those household appliances have no flexibility in usage time or power consumption, and thus the base load profile can not be changed.

We denote the household energy demand at the period k by ξ_k based on the smart meter readings. Assume that p_k is the total power drawn from the grid, out of which r_k is used to charge the battery and d_k denotes the total power discharged from the battery. As illustrated in Figure 4.1, other than supporting the household

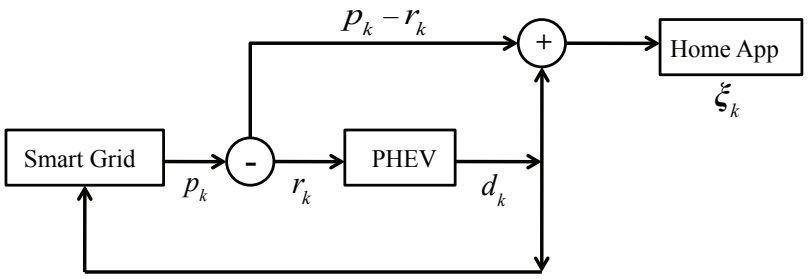

Figure 4.1. System model.

demand, the extra energy discharged from the PHEV battery can be sold back to the market via bidirectional V2G. Therefore, in the basic model, the following constraint must be satisfied:

$$p_k = \xi_k + r_k - d_k. \tag{4.1}$$

Within each time slot, the battery can be either charged or discharged or do neither, but not both. This means that, for the k^{th} period, we have $r_k \cdot d_k = 0$. To eliminate the number of variables, we denote u_k the charging/discharging decisions (charging/discharging amount). The basic model (4.1) is then transformed into

$$p_k = \xi_k + u_k, \tag{4.2}$$

where $u_k > 0$ and $u_k < 0$ means the battery is charged or discharged, respectively; while $u_k = 0$ represents the battery's idle state.

4.1.2 PHEV Battery Model

Lead-acid, lithium-ion and nickel-metal (NiMH) have been the top three contending technologies for PHEV batteries due to a combination of performance capacity, safety, life and cost [88]. In this chapter, we incorporate the following idiosyncrasies of battery operation into the PHEV model.

First, the battery lifetime is shorten with each charging/discharging cycle since the capacity of the battery slowly decreases with high depth-of-discharge (DoD) - percentage of maximum energy removed during a discharge cycle. Therefore, in order to prolong the battery life, the energy level of the battery should not drop below certain state-of-charge (SoC). The relationship between the useful battery lifetime is expressed via battery lifetime charts [89]. To maximize the life of the battery pack, in our study, we limit the state of charging up to x_{max} and never deplete the battery below x_{min}, respectively.

Further, to model the effect of repeated charging and discharging on battery's lifetime, we assume that, within each charging or discharging operation, a fixed cost (in dollars) of C_{rc} and C_{dc} is incurred [90]. Specifically, suppose that a new PHEV battery costs C dollars[1] and it can sustain N charge/discharge cycles, then the loss of the battery value can be set as $C_{rc} = C_{dc} = \frac{C}{N}$.

Besides, with each battery charging and discharging operation, the batteries have conversion loss whereby a portion of the stored energy is lost.[2] In this work, we use the round-trip efficiency η of 85% as our base case. The charging and discharging efficiency are assumed equally the square root of 0.85, which results in the 85% round-trip efficiency [91].

Finally, the energy storage itself is "leaky" due to the self-discharging, so that the stored energy decreases over time, even in the absence of any discharging. Here, we will assume the battery is not leaky, so that the stored energy level decreases only when they are discharged. This is a reasonable assumption when the time scale over which the loss take place is much larger than that of interest to us.

[1] A typical 16-kWh lithium-ion battery costs about $500/kWh (or $250/kWh if manufactured in high volume).

[2] About 10-15% energy is lost for lithium-ion battery charging/ discharging.

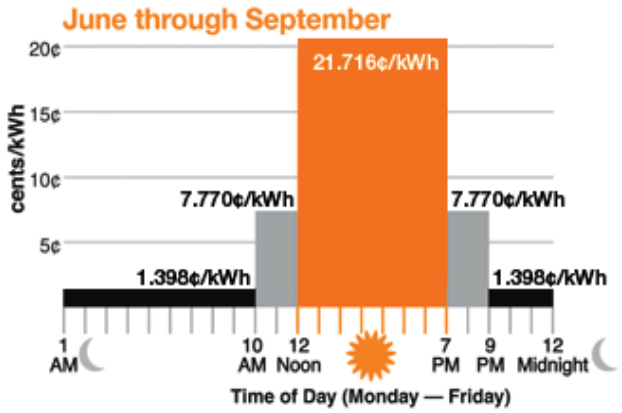

Figure 4.2. O&R electricity TOU pricing [92].

4.1.3 Time-Of-Use (TOU) Electricity Pricing

In this study, we investigate the daily energy cost minimization of vehicle users under the time-of-use (TOU) electricity pricing. TOU electricity pricing rate, whereby the electricity price is set for a specific time period on an advance or forward basis, will typically not change more often than twice a year. Therefore, TOU pricing allows consumers to vary their energy usage in response to such prices and manage their energy costs by shifting usage to a lower cost period or reducing their consumption overall. TOU pricing rate from Orange & Rockland is shown in Figure 4.2.

4.1.4 Bidirectional Vehicle-to-Grid (V2G)

As we have discussed, the basic concept of V2G is that PHEVs provide the energy back to grid. Each PHEV is supposed to have the following three required elements for V2G [73]: (a) a power connection to the grid for electric energy flow; (b) control or logical connection necessary for grid operators, and (c) precision metering on-board the vehicle. Based on the communication functionality of V2G, the information such as household demands, PHEV battery energy level and TOU elec-

tricity pricing could be exchanged between the smart meter and PHEV controller via wired/wireless links. Specifically, once a "regulation up" signal is received, the vehicle provide the energy to the grid (discharging mode); while a "regulation down" signal would cause a decrease in the power output or even draw power from the grid (charging mode).

4.2 Energy Management via Minimizing the Daily Energy Cost

4.2.1 Problem Formulation

In this section, from the PHEV owner point of view, we follow a cost-conscious approach. To this end, we investigate the optimal PHEV energy management strategy to minimize the daily energy cost, and propose to employ the dynamic programming (DP) technique to realize the optimal coordination of PHEV charging and discharging. DP is a numerical technique that can be applied to any problem that requires the decisions to be made in stages with the objective of finding a minimal cost pathway [93]. The DP technique decomposes the original optimization problem into a sequence of subproblems which are solved backward over each stage.

First, we assume that there exist $N+1$ periods within the time span we are interested in, i.e., $n \in 0, 1, \cdots, N$. The decision variables are given by $U := (u_0, u_1, \cdots, u_N)$, where u_k is the charging/discharging decision at the k^{th} period. Denoting x_k the energy level at the beginning of the k^{th} period and y_k the energy level at the end of the k^{th} period, the battery energy balance is

$$y_k = x_k + u_k, \quad k = 0, \cdots, N. \tag{4.3}$$

Further, we specify the energy cost at the k^{th} period as

$$C_k(u_k) \;=\; (K + \frac{r_k}{\eta} \cdot u_k)\Pi_{u_k>0} + (K + r_k\eta \cdot u_k)\Pi_{u_k<0} + r_k \cdot \xi_k, \tag{4.4}$$

where r_k denotes the electricity real-time price, ξ_k is the household energy demand (base household load), and $K = \frac{C}{N}$ represents the loss of the battery value for each charging or discharging, as we have discussed. Note that the *indication function* $\Pi_{u_k>0}$ equals to 1 when $u_k > 0$ and, equals to 0 otherwise.

As we assume that the household appliances have no flexibility in usage time or power consumption, the base household load profile ξ_k cannot be changed. Therefore, the energy cost to optimize is actually

$$c_k(u_k, x_k) \quad = \quad (K + \frac{r_k}{\eta} \cdot u_k)\Pi_{u_k>0} + (K + r_k\eta \cdot u_k)\Pi_{u_k<0}. \tag{4.5}$$

We add the variable x_k in (4.5), since the charging/discharging decision u_k depends on the current battery level x_k, i.e.,

$$x_{min} \leq x_k + u_k \leq x_{max}, \tag{4.6}$$

$$-u_{max} \leq u_k \leq u_{max}. \tag{4.7}$$

In (4.7), the maximum charging amount $u_{max} = CR \cdot T$, where CR is the PHEV battery charging rate and T is the per time slot duration. Clearly, $-u_{max}$ is the maximum discharging value.

Therefore, the *objective function* to minimize is the sum of all the costs incurred during the interval $< 0, N >$ as follows

$$\boldsymbol{J}_0(x; U) = \sum_{k=0}^{N-1} c_k(u_k, x_k) + c_N(u_N, x_N). \tag{4.8}$$

We define the *value function* for the above optimization problem as

$$v_0(x) = \underset{U\in\Phi}{inf}\ \boldsymbol{J}_0(x; U), \tag{4.9}$$

where Φ denotes the class of all admissible charging/discharging decisions.[3]

[3]Once the existence is established, the "*inf*" in (4.9) can be replaced with "*min*".

Note that, at the end of period N, the PHEV battery should be fully charged to serve the daily driving demand at the daytime. Therefore, the end-of-day cost function is given by

$$\begin{aligned} c_N(u_N, x_N) &= (K + \frac{r_N}{\eta} \cdot u_N)\Pi_{u_N>0} \\ &= K \cdot \Pi_{x_{max}>x_N} + \frac{r_N}{\eta}(x_{max} - x_N). \end{aligned} \tag{4.10}$$

Similarly, $\Pi_{x_{max}>x_N}$ equals to 1 when $x_{max} > x_N$ and, equals to 0 otherwise.

Employing the principle of optimality, we develop the following dynamic programming equations:

$$\begin{cases} v_k(x_k) = \underset{u_k}{inf}\big\{c_k(u_k, x_k) + v_{k+1}(x_k + u_k)\big\}, \quad k \in [0, N-1] \\ v_N(x_N) = c_N(u_N, x_N) \end{cases} \tag{4.11}$$

We provide the following lemma to prove that the dynamic programming equations (4.11) provide the optimal PHEV battery charging/discharging decision.

Lemma 4.2.1. *The PHEV batterycharging/discharging decisions* $\hat{U} := (\hat{u}_0, \hat{u}_1, \cdots, \hat{u}_N)$ *of the dynamic programming equations provide the optimal solution for the original optimization problem* $\mathbf{J}_0(x; U)$.

Proof. See Appendix D. □

4.2.2 Optimality of (s,S,s',S')-type Feedback Policy

Lemma 4.2.1 has proved the existence of optimal battery charging/discharging policy. However, the computational complexity for the optimal policy is prohibitive

even for a small N [93]. Therefore, we further investigate the dynamic programming equations as follows:

$$\begin{aligned} v_k(x_k) &= \inf_{u_k}\Big\{c_k(u_k,x_k)+v_{k+1}(x_k+u_k)\Big\} \\ &\overset{(a)}{=} \inf_{u_k}\Big\{(K+\frac{r_k}{\eta}\cdot u_k)\Pi_{u_k>0}+(K+r_k\eta\cdot u_k)\Pi_{u_k<0}+v_{k+1}(y_k)\Big\} \\ &\overset{(b)}{=} \Big\{[-\frac{r_k}{\eta}\cdot x_k\Pi_{y_k>x_k}+h_k(x_k)]+[-r_k\eta\cdot x_k\Pi_{y_k<x_k}+h'_k(x_k)]\Big\}, \quad (4.12) \end{aligned}$$

where (a) is derived from the battery energy balance (4.3) and the objective function (4.5); (b) follows

$$\begin{aligned} h_k(x_k) &= \inf_{y_k\geq x_k}\big\{K\cdot\Pi_{y_k>x_k}+\frac{r_k}{\eta}\cdot y_k+v_{k+1}(y_k)\big\} \\ &= \inf_{y_k\geq x_k}\big\{K\cdot\Pi_{y_k>x_k}+p_k(y_k)\big\}. \quad (4.13) \\ h'_k(x_k) &= \inf_{y_k\leq x_k}\big\{K\cdot\Pi_{y_k<x_k}+r_k\eta\cdot y_k+v_{k+1}(y_k)\big\} \\ &= \inf_{y_k\leq x_k}\big\{K\cdot\Pi_{y_k<x_k}+q_k(y_k)\big\}. \quad (4.14) \end{aligned}$$

To simplify the above equations, we introduce

$$\begin{aligned} p_k(y_k) &= \frac{r_k}{\eta}\cdot y_k+v_{k+1}(y_k), \quad (4.15) \\ q_k(y_k) &= r_k\eta\cdot y_k+v_{k+1}(y_k), \quad (4.16) \end{aligned}$$

and further define

$$\begin{aligned} p^* &= \inf_{x_{min}\leq y_k\leq x_{max}}[p_k(y_k)], \quad (4.17) \\ q^* &= \inf_{x_{min}\leq y_k\leq x_{max}}[q_k(y_k)]. \quad (4.18) \end{aligned}$$

Then we define the thresholds s_k, S_k, s'_k, S'_k as

$$\begin{aligned} S_k &= min\,\{x\in[x_{min},x_{max}]|p_k(x)=p^*\}, \quad (4.19) \\ s_k &= min\,\{x\in[x_{min},x_{max}]|p_k(x)\leq K+p(S_k)\}, \quad (4.20) \\ S'_k &= max\,\{x\in[x_{min},x_{max}]|q_k(x)=q^*\}, \quad (4.21) \\ s'_k &= max\,\{x\in[x_{min},x_{max}]|q_k(x)\leq K+q(S'_k)\}. \quad (4.22) \end{aligned}$$

Given the introduction of the thresholds s_k, S_k, s'_k, S'_k, a state-independent four-threshold (s_k, S_k, s'_k, S'_k) feedback policy can be expressed as

$$u_k = \begin{cases} u_{max}, & if \quad x < s_k,\ x < S_k - u_{max} \\ S_k - x, & if \quad S_k - u_{max} \le x < s_k \\ 0, & if \quad s_k \le x \le s'_k \\ S'_k - x, & if \quad s'_k < x < S'_k + u_{max} \\ -u_{max}. & if \quad x > s'_k,\ x \ge S'_k + u_{max} \end{cases} \tag{4.23}$$

The optimality of the (s_k, S_k, s'_k, S'_k) feedback police is proved by the following theorem.

Theorem 6. *Given the thresholds* s, S, s', S'*, the proposed state-independent four-threshold (*s, S, s', S'*) feedback policy (4.23) is optimal for PHEV battery charging/discharging.*

Proof. See Appendix E. □

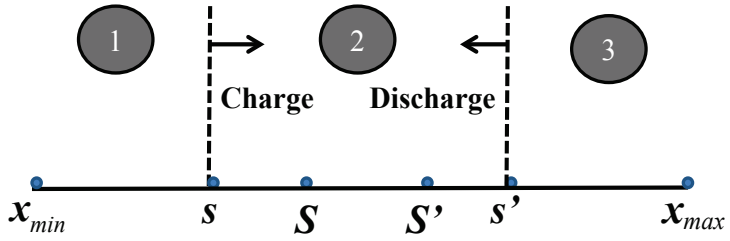

Figure 4.3. (*s, S, s', S'*) charging/discharging policy.

The principle of the proposed (*s, S, s', S'*) policy is that if the battery energy level is below s, the battery should be charged to the energy level S; if the battery level is above *s'*, the battery should be discharged to the energy level *S'*; otherwise, the battery is kept in the idle state. Just as shown in Figure 4.3, *region 1* and *region*

3 are the charging and discharging region, respectively; while *region 2* denotes the idle state.

To practically implement the (*s, S, s', S'*) policy, a "$N \to 0$" backward iteration algorithm is proposed in Algorithm 1.

Algorithm 2 "$N \to 0$" Backward Iteration Algorithm

1: Initialize $v_N(x_N)$ according to (4.10);
2: **for** k=N-1 to 0 **do**
3: Formulate the value function $v_k(x_k)$ from (4.12);
4: Calculate p^* and q^*;
5: Calculate S_k, s_k, S'_k and s'_k according to (4.19)-(4.22);
6: Update $v_{k-1}(x_{k-1})$ according to (4.12);
7: end **for**

4.2.3 Case Study

In this part, we aim to evaluate the validity of our proposed (*s, S, s', S'*) feedback policy. We base the PHEV battery model on a typical lithium-ion battery (Table 4.1). Two types of battery capacity, i.e., Volt (16 kW) and Nissan Leaf (24 kW) are considered. In terms of the battery charging/discharging strategy, two charging levels, i.e., 120V/16A (single phase) and 240V/32A (split phase), are defined by SAE J1772 [94], which is the North American standard for electrical connectors for electric vehicles. To maximize the life of the battery pack, in this work, we limit the state of charging up to 90% of the battery capacity (x_{max}) and never deplete the battery below 30% (x_{min}), respectively.

Parameters	Characteristics
Battery Type	Lithium-ion
Round Trip Efficiency (RTE)	85%
Battery Capacity-1	16 kW
Battery Capacity-2	24 kW
Battery Charging Type-1 (Single phase)	120V / 16A
Battery Charging Type-2 (Split phase)	240V / 32A

Table 4.1. Battery parameters

Base load profile (Figure 4.4) is the average residential load in the service area of Southern California Edison from 07/30/2012 (Monday) to 08/03/2012 (Friday) [95]. Since we mainly focus on the application of PHEV on local household load shaping at home, the time duration of interest is between 5 P.M. and 8 A.M. Besides, we adopt the TOU electricity price from Orange & Rockland (Figure 4.2). To be fair, we assume that there are 45% energy is left in the Type-1 PHEV battery and 60% energy left in the Type-2 PHEV battery, after round trip between home and work place[4].

Figure 4.5 illustrates the battery charging/discharging profile based on our proposed (*s, S, s', S'*) feedback policy. Clearly, we observe that the principle of our proposed charging strategy is for PHEV batteries to store grid electricity generated at off-peak hours (low electricity price) for household use during peak hours (high electricity price).

The performance of our proposed (*s, S, s', S'*) feedback policy on daily energy cost is shown in Figure 4.6. The positive value represents making profits while the negative value is the daily energy cost for charging the PHEV. We compare our

[4]According to the surveys, the average American drives less than 29 miles a day. Therefore, 45% of Type-1 battery capacity and 30% of Type-2 battery capacity could equally meet the daily driving demand at the daytime.

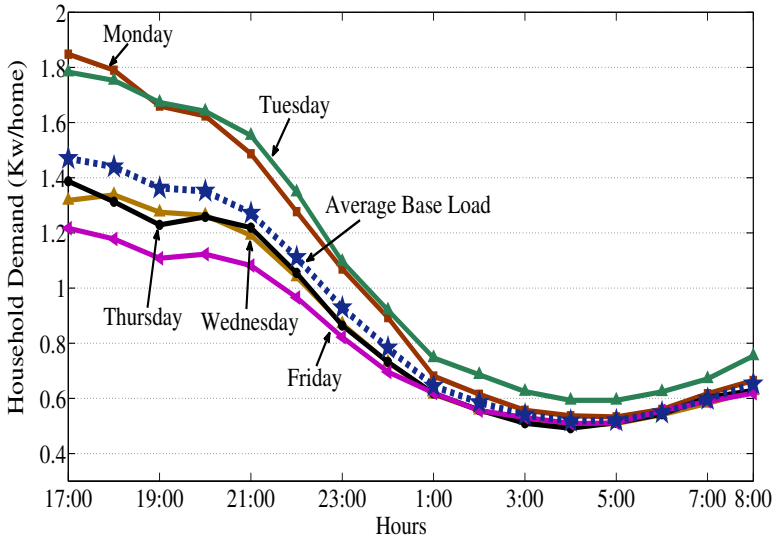

Figure 4.4. Base load profile is the average residential load in the service area of Southern California Edison from 07/30/2012 to 08/03/2012 [95]..

proposed energy management policy with two other charging strategies: a business-as-usual (BAU) scenario assuming full charging starting upon plugging in the PHEV and a "smart" charging scheme which represents charging the battery only at off-peak periods. Apparently, our proposed algorithm is optimal in daily energy cost performance. It is observed that, on the one hand, fast charging/discharging (split phase) will always outperform the slow charging/discharging scenario (single phase). This is due to the fact that with fast discharging rate, the PHEV could gain more profits by means of selling more energy during the peak load hours via V2G. On the other hand, battery capacity also plays a significant role in daily energy cost performance. It is intuitive that large battery capacity could store more power to serve the household demand (or selling the energy back to the market) at peak load hours.

Figure 4.7 demonstrates the impact of different PHEV charging schemes on base load profile. We take Type-1 PHEV battery and slow charging level as an example.

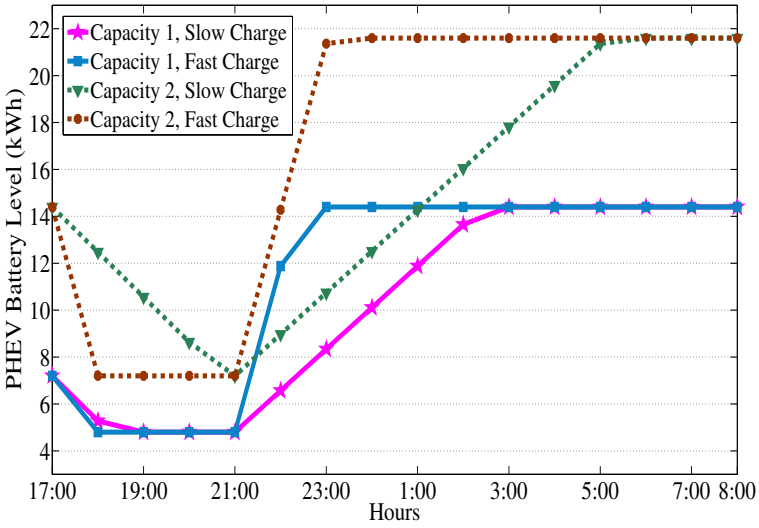

Figure 4.5. PHEV battery charging/discharging profile.

Clearly, due to the PHEV charging, BAU and "smart" charging strategies will either amplify the base load or keep the overall load high during the peak load hours (17:00-21:00); while our proposed algorithm could significantly reduce the overall load during the peak load hours via V2G. It is worth mentioning that, even though our proposed (*s, S, s', S'*) policy reduces the overall load at peak hours (17:00-21:00), the new peak load at off-peak hours (after 21:00) will still extend considerable pressures on smart grid. Hence, another key question is how to efficiently manage the PHEV charging strategy aiming to minimize the peak load and flatten the overall load profile.

4.3 Energy Management via Flattening the Overall Load

In this section, we turn our attention to another goal on PHEV energy management: shaving the peak load and flattening the overall load profile.

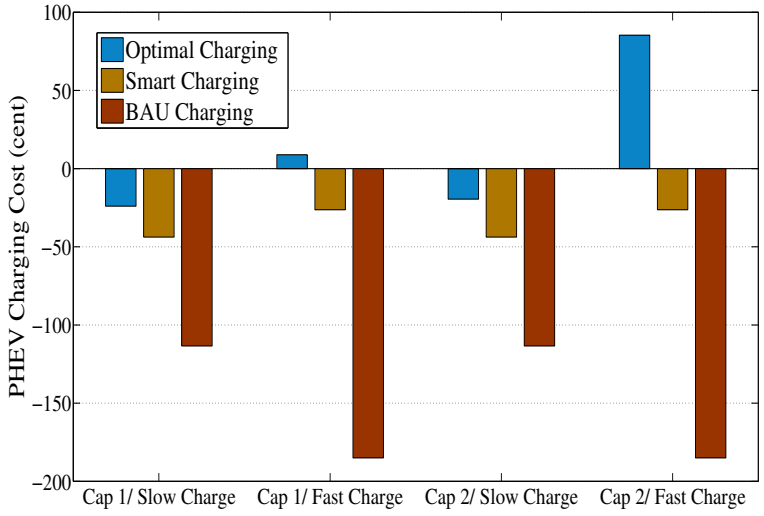

Figure 4.6. PHEV charging cost comparison.

From the distribution system operator point of view, our approach is to shape the PHEV charging profile with the purpose of flattening the overall load, i.e., base load ξ_k plus PHEV load u_k. The optimization problem is formulated as

$$\begin{aligned} \min_{u_0,\cdots,u_N} \quad & \sum_{k=0}^{N} V\big(\xi_k + u_k\big) \\ s.t. \quad & 0 \le u_k \le u_{max}, \qquad k = 0, \cdots, N \\ & \sum_{k=0}^{N} u_k = P \end{aligned} \tag{4.24}$$

where u_k is the charging variable to optimize, the map $V(\cdot) : \mathbf{R} \to \mathbf{R}$ is strictly convex and P is the total charging task as

$$P = \frac{x_{max} - x_0}{\eta}. \tag{4.25}$$

In this study, we choose l_2 norm of the overall load profile $V(x) = x^2$. Later we will prove that the optimality of a charging profile $\boldsymbol{u} := (u_0, \cdots, u_N)$ is independent

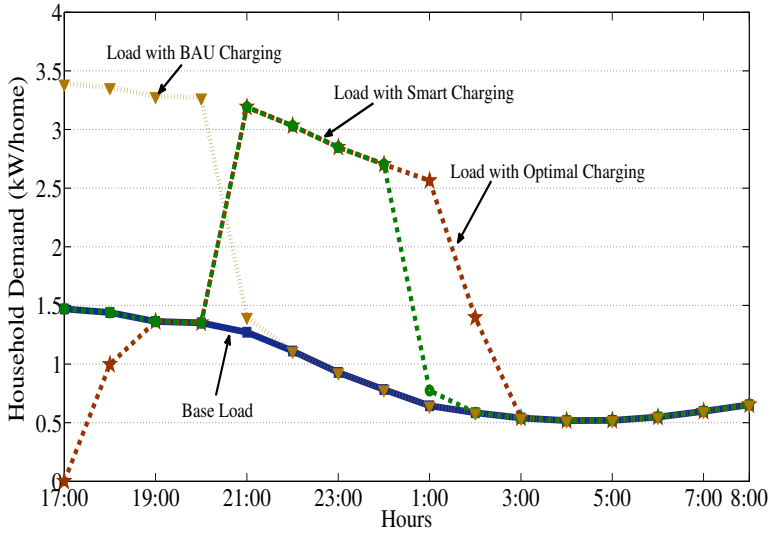

Figure 4.7. Impact of PHEV charging on base load profile.

of the choice of the map $V(\cdot)$ as long as $V(\cdot)$ is strictly convex. The optimization problem is thus transformed into

$$\begin{aligned} \min_{u_0,\cdots,u_N} \quad & \sum_{k=0}^{N} \big(\xi_k + u_k\big)^2 \\ s.t. \quad & 0 \le u_k \le u_{max}, \qquad k = 0, \cdots, N \\ & \sum_{k=0}^{N} u_k = P. \end{aligned} \tag{4.26}$$

The related Lagrangian function G is given as

$$G \;=\; \sum_{k=0}^{N} \big(\xi_k + u_k\big)^2 - \sum_{k=0}^{N} \lambda_k u_k + \sum_{k=0}^{N} \mu_k \big(u_k - u_{max}\big) + \nu\big(\sum_{k=0}^{N} u_k - P\big). \tag{4.27}$$

Traditionally, numerical optimization methods, such as subgradient and interior point algorithms can be employed to solve the above optimization problem. However, these traditional methods require iterative calculations and can only numerically achieve the optimal solution (i.e., no closed-form solution is achieved). Therefore, in

this chapter, to derive the closed-form solutions, we develop the following Karush-Kuhn-Tucker (KKT) conditions [61]:

$$\begin{aligned}
\frac{\partial G}{\partial u_k} = 2\big(\xi_k + u_k\big) - \lambda_k + \mu_k + \nu &= 0 \\
\sum_{k=0}^{N} u_k - P &= 0 \\
u_k - u_{max} &\leq 0 \\
u_k &\geq 0 \\
\lambda_k &\geq 0 \\
\mu_k &\geq 0 \\
\lambda_k \cdot u_k &= 0 \\
\mu_k \cdot \big(u_k - u_{max}\big) &= 0
\end{aligned}$$

Solving the KKT conditions, we obtain a reminiscent "water-filling" solution in wireless communications,

$$u_k^* = min\Big\{\big(-\frac{\nu}{2} - \xi_k\big)^+, u_{max}\Big\}, \tag{4.28}$$

where x^+ equals to 0 when x is less than zero, and otherwise equals to x. Due to the space limitation, we omit the derivation of the "water-filling" solution, which can be derived from transforming $\lambda_k \cdot u_k = 0$ and $\mu_k \cdot \big(u_k - u_{max}\big) = 0$.

Actually, "water-filling" is our intuitive solution to optimally flatten the overall load file, which is now theoretically verified. Besides, from $\sum_{k=0}^{N} u_k = P$, the unknown variable ν can be obtained from

$$\sum_{k=0}^{N} min\Big\{\big(-\frac{\nu}{2} - \xi_k\big)^+, u_{max}\Big\} = P. \tag{4.29}$$

The left-hand side (LHS) is a piecewise-linear increasing function of $-\frac{\nu}{2}$, with break-points at ξ_k. So the equation has a unique solution which is readily determined.

So far, we have derived a reminiscent of the "water-filling" solution as the optimal PHEV charging strategy. Next, we will prove that the optimality of "water-filling" strategy does not depend on the choice of $V(\cdot)$.

Theorem 7. *If the map $V(\cdot)$ is strictly convex, the optimal charging profile with respect to (4.24) is not relevant to the choice of $V(\cdot)$.*

Proof. Let $\boldsymbol{u'} := (u'_0, u'_1, \cdots, u'_N)$ denote the set of optimal charging decision with regard to $\hat{V}(x) = x^2$. Further, we denote $\boldsymbol{u}^{opt} := (u_0^{opt}, u_1^{opt}, \cdots, u_N^{opt})$ the arbitrary charging profile with a different choice of $V(\cdot)$, as we assume that the optimal charging profile is not unique.

According to the first order optimality condition,

$$f'(x)^T \cdot \big(y - x\big) \geq 0 \quad \textit{for all } y \in \mathbf{X}. \tag{4.30}$$

Since both $\boldsymbol{u'}$ and $\boldsymbol{u}^{opt}$ are optimal, we obtain

$$< V'\big(\xi_k + u'_k\big), \big(u_k^{opt} - u'_k\big) > \ \geq \ 0 \tag{4.31}$$

$$< V'\big(\xi_k + u_k^{opt}\big), \big(u'_k - u_k^{opt}\big) > \ \geq \ 0 \tag{4.32}$$

where $< x, y >= \sum_{k=0}^{N} x_k y_k$.

Summing up (4.31) and (4.32), it is derived that

$$< V'\big(\xi_k + u_k^{opt}\big) - V'\big(\xi_k + u'_k\big), \big(u'_k - u_k^{opt}\big) > \ \geq 0.$$

However, according to the strict convexity of $V(\cdot)$, it follows that $V'(\cdot)$ is strictly increasing as

$$< V'\big(\xi_k + u_k^{opt}\big) - V'\big(\xi_k + u'_k\big), \big(u'_k - u_k^{opt}\big) > \ \leq 0.$$

To obtain the equality, we have $u'_k = u_k^{opt}$, and thus $\boldsymbol{u'} = \boldsymbol{u}^{opt}$. It is concluded that optimal charging profile is not relevant to the choice of $V(\cdot)$ and thus "water-

filling" solution is always optimal in PHEV battery charging. The proof is complete.[5]

□

Hours	**17:00**	**18:00**	**19:00**	**20:00**	**21:00**	**22:00**
Load (kWh)	1.4703	1.4396	1.3732	1.3732	1.3732	1.3732
Hours	**23:00**	**24:00**	**1:00**	**2:00**	**3:00**	**4:00**
Load (kWh)	1.3732	1.3732	1.3732	1.3732	1.3732	1.3732
Hours	**5:00**	**6:00**	**7:00**	**8:00**		
Load (kWh)	1.3732	1.3732	1.3732	1.3732		

Table 4.2. Overall load profile with "water-filling" charging strategy

Finally, we provide the following simulation to evaluate the performance of our proposed charging algorithm. We use the same simulation setup as Section III and similarly, we take Type-1 PHEV battery and slow charging level as an example for analysis. The overall load profile with "water-filling" charging strategy is illustrated in Table 4.2.

Clearly as shown in Table 4.2, the height of the water surface $-\frac{\nu}{2}$ in our case study is 1.3732, which means if the base load ξ_k is higher than 1.3732 kWh, the PHEV will choose not to charge; otherwise, the PHEV battery will be charged to the surface level.

From Figure 4.8, it can be appreciated that, compared with other charging schemes, "water-filling" charging strategy could remove the peak load and flatten the overall load profile. Furthermore, we conclude that the principle of "water-filling" charging strategy is not only the charging time but also the charging rate determine the load profile shaping. To sum up, "water-filling" charging strategy, which dis-

[5]A similar proof method is adopted in [77].

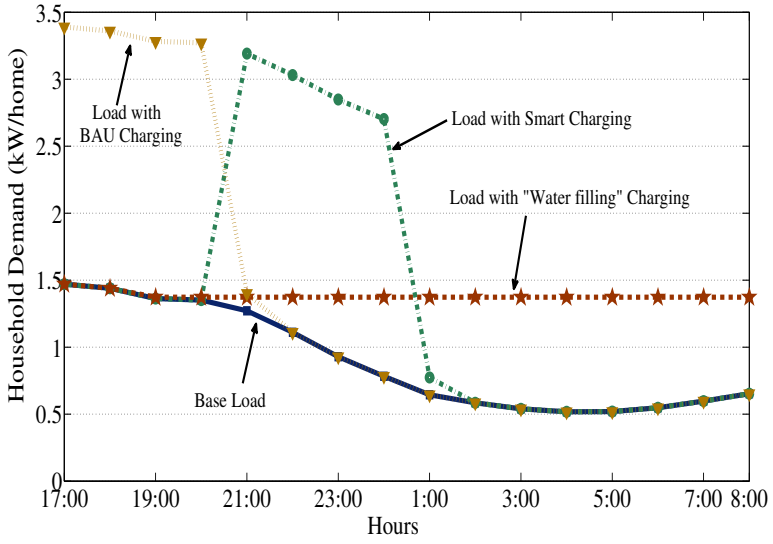

Figure 4.8. Optimal "water-filling" charging strategy.

tributes the whole charging task over the entire time-span, is optimal in flattening the overall load profile.

4.4 Conclusions

In this chapter, we explored the optimal energy management strategies for PHEVs via bidirectional V2G. We first follow a cost-conscious approach. Aiming to minimize the daily energy cost, we formulated the energy management problem through dynamic programming. To avoid the computational complexity in solving dynamic programming, we proved that a state-independent four-threshold (*s, S, s', S'*) charging/discharging policy is optimal based on stochastic inventory theory. A "$N \to 0$" backward iteration algorithm was then proposed to practically implement the (*s, S, s', S'*) feedback policy. Further, we focus on shaving the peak load and flattening the overall load profile. We proposed an optimal PHEV charging scheme and derived a reminiscent "water-filling" solution. The performance of our proposed

algorithms are demonstrated by numerous illustrative simulations based upon the real data.

Chapter 5

Conclusions

This chapter concludes the whole dissertation. It begins with a summary of the dissertation results and contributions, follows with a discussion of future research directions in hybrid wireless networks and cooperative-diversity networks.

5.1 Summary

This dissertation has focused on the capacity and optimization of hybrid and smart grid wireless networks. The contributions of this dissertation are:

- *On the Throughput Capacity and Performance Analysis of Hybrid Wireless Networks over Fading Channels*: the theoretical per-node data transmission limits for hybrid wireless networks over fading channels is studied. To overcome fading impairments, we introduce an optimal multiple access technique allowing opportunistic sources to transmit concurrently with the scheduled source. We first define the outage throughput capacity as the performance criteria for slow fading scenario. We prove that under intra-cell mode, the per-node outage throughput capacity over Nakagami-m fading is $O\big(\log[(\epsilon\frac{1}{m})^{\frac{b}{n}}\frac{n}{b}]\,W_1\big)$; while under infrastructure mode, the related outage throughput capacity is $\Theta\big(\frac{b}{n}\log(\epsilon\frac{1}{m}\frac{n}{b})\,W_2\big)$, which are published in [111] [119]. Further we specified the ergodic throughput capacity as the performance measurement for fast fading situation. We show that under intra-cell transmission mode, the ergodic throughput capacity is $O\big(\frac{n}{b}W_1\big)$ at low SINR and $O\big(\log(\frac{n}{b})W_1\big)$ at high SINR; while, under infrastructure transmission mode, the ergodic throughput capacity is derived as $\Theta\big(W_2\big)$

at low SINR and $\Theta\big(\frac{b}{n}\log(\frac{1}{m}\cdot\frac{n}{b})\,W_2\big)$ at high SINR, respectively [117]. Finally presented is the QoS performance analysis in terms of the per-node AEP for hybrid wireless network [116]. It is concluded that, with opportunistic sources, the intra-cell mode effectively combats fading as wireless nodes increases; however, the infrastructure mode is bottlenecked by the downlink transmission since base station is the only transmitter in the cell during the downlink phase. Our study on the throughput capacity of hybrid wireless networks over fading channels is summarized in [110].

- *Analysis and Improvement of the Voltage Regulation in Microgrid Based on Sensor Selection*: the voltage regulation issue in microgrid is investigated, and the WSANs is applied to accurately monitor the real-time voltage level and coordinate DERs with the traditional voltage regulators. To achieve proper voltage regulation, several sensor selection schemes are proposed to improve the voltage measurement accuracy and power efficiency. An opportunistic sensor selection scheme under equal power allocation is first proposed to improve the voltage estimation performance. The asymptotic behaviors with the power constraint and the voltage sensor number approaching infinity are investigated. We have further addressed sensor selection scheme under optimal power allocation and derived a "water-filling" solution for this scenario. Besides, we illustrate the improvements on power efficiency employing the proposed sensor selection strategies, as elaborated in [120] [123]. Finally, aiming to maximize the transmission rate between the voltage sensors and the control center, we heuristically proposed the joint power and spectrum allocation strategy based on voltage sensor selection [115]. Numerical simulation results have demonstrated that our pro-

posed sensor selection algorithms can efficiently regulate the voltage level and stabilize the power supply [121].

- *Energy Management Strategy for Plug-in Hybrid Electric Vehicles Via Bidirectional Vehicle-to-Grid*: the optimal energy management strategies for PHEVs via bidirectional V2G is explored. We first follow a cost-conscious approach. Aiming to minimize the daily energy cost, we formulated the energy management problem through dynamic programming. To avoid the computational complexity in solving dynamic programming, we proved that a state-independent four-threshold (*s, S, s', S'*) charging/discharging policy is optimal based on stochastic inventory theory. A "$N \to 0$" backward iteration algorithm was then proposed to practically implement the (*s, S, s', S'*) feedback policy [118]. Further, we focus on shaving the peak load and flattening the overall load profile. We proposed an optimal PHEV charging scheme and derived a reminiscent of "water-filling" solution [122]. The performance of our proposed algorithms are demonstrated by numerous illustrative simulations based upon the real data.

5.2 Future Directions

5.2.1 Throughput Capacity of Hybrid Wireless Networks with Hexagon Cell Structure and Poisson Point Process (PPP) Distributed Base Station

In our previous research, we assume the square cell structure and uniformly distributed base stations, as shown in Figure 2.1.

Square cell structure can facilitate the theoretical analysis, especially simplifying the application of the frequency reuse strategy. However, from a more practical point of view, the hexagon cell structure should be adopted, as shown in Figure 5.1.

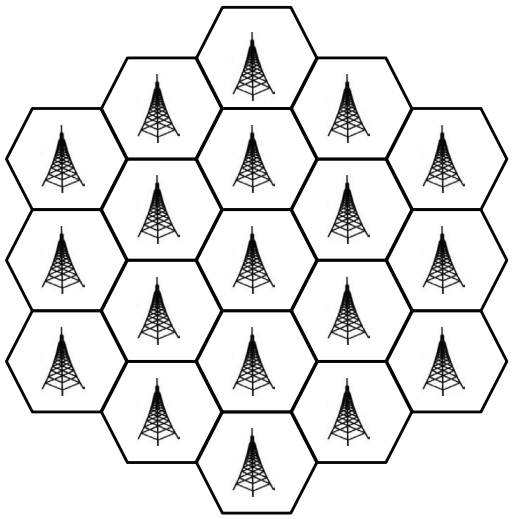

Figure 5.1. Hexagon cell structure.

With hexagon cell structure, we need to re-analyze the inter-cell interferences with the updated frequency reuse factor.

Further, we will introduce an additional source of randomness: the positions of the base stations. Instead of assuming they are placed deterministically on a regular grid, we model their location as a homogeneous Poisson Point Process (PPP) of density λ, as illustrated in Figure 5.2. Such an approach for BS modeling has been considered in [108] [109] but the key metrics of coverage (SINR distribution) and transmission rate have not been determined. With PPP distributed base stations, we assume each node is associated with the closest base station; namely the users in the Voronoi cell of a base station are associated with it, resulting in coverage areas that comprise a Voronoi tessellation on the plane.

Therefore, one task of our future work is to analyze the throughput performance of hybrid wireless network with hexagon cell structure and PPP distributed base stations.

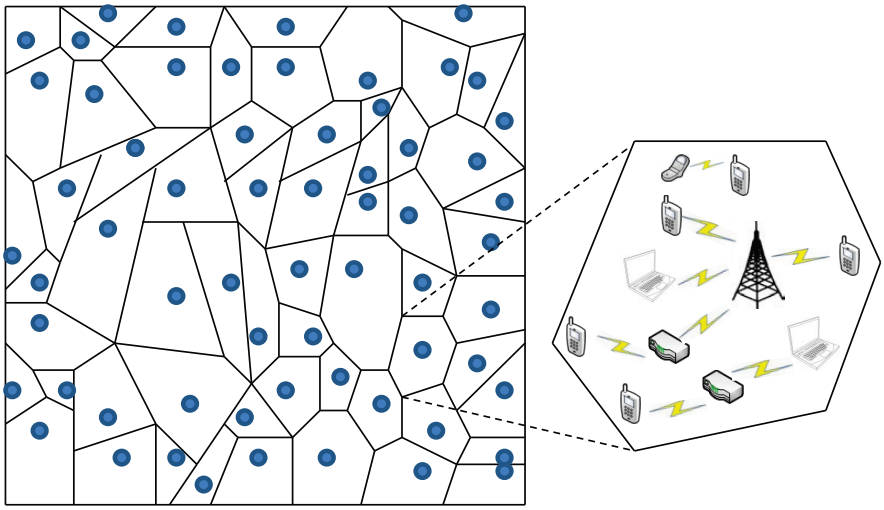

Figure 5.2. Poisson distributed base stations, with each nodes associated with the nearest base stations. The cell boundaries are shown and form a Voronoi tessellation.

5.2.2 Throughput Capacity of Cooperative-diversity Networks over Fading Channels

Diversity techniques are known as effective means to combat the wireless channel fading. Recently, cooperative-diversity networks have attracted wide attention, since the cooperation among the terminals has the potential to provide an increased throughput capacity in comparison with the systems without terminal cooperation. More specifically, the source (S) transmits the signal to the destination (D) not only through the direct link but also through indirect links using cooperative relays (R), as illustrated in Figure 5.3. Therefore, the quality of the end-to-end transmission is guaranteed even if the direct link from the source to destination is in deep fade. Relays can also provide transmit power saving due to the path-loss effect and spatial diversity.

In the open literature, several works investigating cooperative-diversity communications are available [97]-[103]. In [97], J. Laneman *et al.* developed various cooperative diversity protocols for a pair of terminals based on relays amplifying their received signals or fully decoding and repeating information, which are referred

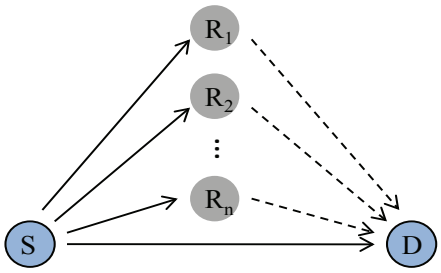

Figure 5.3. A illustration of the cooperative-diversity network with n relays.

to as *amplify-and-forward* (AF) and *decode-and-forward* (DF), respectively. These diversity algorithms were further employed to combat multiple-path fading in larger networks [98]. In [99], an exact closed-form expression is derived for the ergodic capacity of dual-hop AF cooperative networks. Further, the capacity bounds and the ergodic capacity for wireless single-relay channels employing DF or compress-and-forward (CF) relaying protocols are obtained for the Rayleigh fading scenario, assuming the transmitter channel side information (CSI) is available [100]. In [102], the authors analyzed both outage capacity and ergodic capacity of the cooperative diversity systems under independent non-identically distributed (i.n.d.) Rayleigh fading channels, and derived an approximated closed-form analytical expressions for the outage capacity. Further, the authors of [103] show that a cooperative-diversity system employing DF relaying protocol offers higher ergodic capacities than the systems with AF relaying strategy. *However, to the best of the authors' knowledge, it is still a significant open question on the throughput capacity performance of cooperative-diversity networks over general fading channels.*

As shown in Figure 5.4, we consider a multiple-relay assisted cooperative diversity system, where the source S communicates with the destination D with the help of N potential relay nodes, denoted by $r_1, r_2, \cdots, r_N$. We assume that the relays operate in half-duplex mode. Note that the medium access control (MAC) employs a time

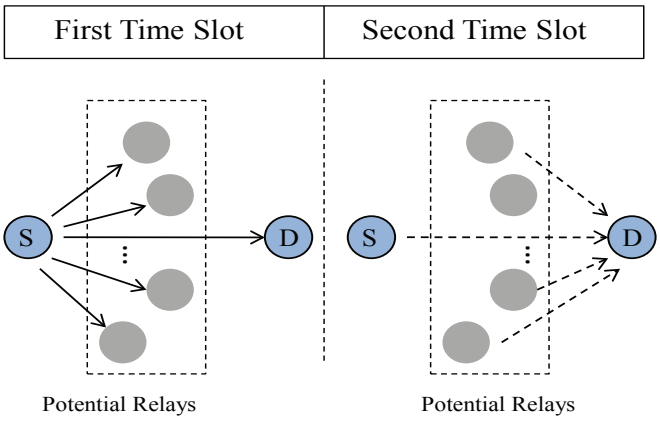

Figure 5.4. Cooperative-diversity network model: half duplex cooperation.

division multiple access (TDMA) scheme to allocate orthogonal time slots of length $\frac{1}{N+1}$ of the total transmission time to the source and each relay for their transmission. In addition, we assume that the channel state information (CSI) is only available at the receiver and not known by all the transmitters. We take decode-and-forward (DF) relaying protocol into consideration and the whole transmission is accomplished in two phases. In phase I, the source broadcasts its signal to the set of N-relay nodes ($S \rightarrow R$) and the destination node ($S \rightarrow D$). In phase II, only the relay that can fully decode the signal received from the source will re-encode and forward the signal to the destination ($R \rightarrow D$). Here, we define the decoding set (Θ) as the set of relays with the ability of fully decoding the source signal correctly. The relay is said to belong to the decoding set provided that the channel between the source and relay node is sufficiently good to allow for successful relay decoding. Finally, at the destination, the received signal from the source and the all participating relays are combined with the maximal ratio combing (MRC) technique.

We denote the complex channel gain between the source and the destination, between the source and i^{th} relay, and between the i^{th} relay and the destination as h_{sd},

h_{si} and h_{id}, respectively. We assume that all the links are subject to Nakagami-m fading, and all the channel gains are mutually independent. We also assume, without loss of generality, that AWGN terms of all the links have zero mean and equal variance N_0. From the information theory point of view, the mutual information between the source and the i^{th} cooperative relay nodes, $i = 1, \cdots, \mathrm{N}$, is given by [19]

$$I_i = \frac{1}{N+1} \log_2(1 + \mathrm{SNR}|h_{si}|^2) \tag{5.1}$$

where SNR denotes the transmitted signal-to-noise ratio (SNR) and N is the total number of the potential relays.

As is known, the probability density function (pdf) of a Nakagami-m random variable $|h_{si}|$ (magnitude) is

$$f(h) = \frac{2}{\Gamma(m_i)} \left(\frac{m_i}{\Omega}\right)^{m_i} h^{2m_i-1} \exp\left(\frac{-m_i h^2}{\Omega}\right), \quad h \geq 0 \tag{5.2}$$

where $m_i = \frac{E^2[h^2]}{Var[h^2]}$ is the shape parameter of the i^{th} link, $\Omega = E[h^2]$ stands for the controlling spread and $\Gamma(\cdot)$ is the Gamma function defined by

$$\Gamma(m_i) = \int_0^\infty t^{m_i-1} e^{-t} dt. \tag{5.3}$$

Therefore, we conclude that $|h_{si}|^2$ is Gamma (Erlang)[1]-distributed $|h_{si}|^2 \sim \Gamma(m_i, \frac{1}{m_i})$, since the pdf of $|h_{si}|^2$ is

$$f(x) = \frac{{m_i}^{m_i}}{\Gamma(m_i)} x^{m_i-1} e^{-m_i x}, \quad x \geq 0. \tag{5.4}$$

Capacity analysis is of significant importance in the design of wireless systems since it determines the maximum achievable transmission rates. As the performance

[1]In this study, we assume that m is an integer for analysis clarity. The Erlang distribution is a special case of the Gamma distribution of integer value of m.

criterion for the long-term average achievable rate over all states of the time-varying fading channels, the end-to-end ergodic capacity can be expressed as [2]

$$C_i = \frac{1}{N+1}\mathbf{E}\big[\log_2(1+\mathrm{SNR}|h_{si}|^2)\big] \tag{5.5}$$

where $\mathbf{E}(\cdot)$ is the expected value.

As we have discussed, in terms of the decode-and-forward relaying protocol, the availability of a relay node to assist the communication between the source and the destination, depends on the channel quality between the source and the relay. That is, only if the mutual information of a source-relay link is greater than the target rate, R, the relay node belongs to the cooperative set Θ, $i \in \Theta$. We denote n as the number of relay terminals within the cooperative set Θ, i.e., n is the cardinality of the cooperative set Θ.

The *conditional* mutual information of the DF relay communication system is given by

$$I|\Theta = \frac{1}{N+1}\left[\log_2\left(1+\mathrm{SNR}\big(|h_{sd}|^2+\sum_{i\in\Theta}|h_{id}|^2\big)\right)\right]. \tag{5.6}$$

Employing *the law of total probability*, the ergodic capacity of the DF relay communication system, C_{ergo}, can be written as

$$C_{ergo} = \sum_{\Theta}\mathbf{E}\big(I|\Theta\big)Pr\big(\Theta\big) \tag{5.7}$$

where $Pr\big(\Theta\big)$ is the probability that n relays of the whole N relays can decode the packet from the source successfully, which is expressed as

$$Pr\big(\Theta\big) = \prod_{i\in\Theta}\Big(Pr\big(I_i \geq R\big)\Big)\prod_{i\notin\Theta}\Big(Pr\big(I_i < R\big)\Big) \tag{5.8}$$

[2]Unless otherwise indicated, logarithms in this chapter are taken to base 2.

Taking into account the Nakagami-m fading channel property, we obtain the successfully decoding probability as follows

$$\begin{aligned} Pr\big(I_i \geq R\big) &= Pr\left(|h_{si}|^2 > \frac{2^{(N+1)R}-1}{\text{SNR}}\right) \\ &= \int_T^{\infty} \frac{{m_i}^{m_i}}{\Gamma(m_i)} x^{m_i-1} e^{-m_i x} dx \\ &\overset{\text{(a)}}{=} \frac{\Gamma(m_i, m_i T)}{\Gamma(m_i)} \\ &\overset{\text{(b)}}{=} {m_i}^{m_i} e^{-m_i T} \sum_{k=0}^{m_i-1} \frac{T^k}{k! \cdot {m_i}^{m_i-k}} \end{aligned} \tag{5.9}$$

where m_i is the fading shape parameter, $T = \frac{2^{(N+1)R}-1}{\text{SNR}}$, (a) follows the definition of incomplete gamma function, and (b) follows that for integer n, $\Gamma(n,x) = (n-1)! \cdot e^{-x} \sum_{i=0}^{n-1} \frac{x^i}{i!}$ and $\Gamma(n) = (n-1)!$.

Similarly, we derive the following non-decoding probability:

$$\begin{aligned} Pr\big(I_i < R\big) &= Pr\left(|h_{si}|^2 < \frac{2^{(N+1)R}-1}{\text{SNR}}\right) \\ &\overset{\text{(a)}}{=} \frac{\gamma(m_i, m_i T)}{\Gamma(m_i)} \\ &\overset{\text{(b)}}{=} 1 - {m_i}^{m_i} e^{-m_i T} \sum_{k=0}^{m_i-1} \frac{T^k}{k! \cdot {m_i}^{m_i-k}} \end{aligned} \tag{5.10}$$

where (a) follows the definition of incomplete gamma function, and (b) follows $\gamma(n,x) = (n-1)!\big[1 - e^{-x} \sum_{i=0}^{n-1} \frac{x^i}{i!}\big]$.

Now, substituting (5.9) and (5.10) into (5.8), we can obtain the probability of cooperative relay set $Pr\big(\Theta\big)$.

In order to calculate the conditional ergodic capacity in (5.7), $\mathbf{E}\big(I|\Theta\big)$, we denote

$$\begin{aligned} Y &= |h_{sd}|^2 + \sum_{i \in \Theta} |h_{id}|^2 \\ &= \chi_0 + \chi_1 + \cdots + \chi_n \end{aligned} \tag{5.11}$$

with $\chi_0 = |h_{sd}|^2$ and $\chi_i = |h_{id}|^2$, $i = 1, \cdots, n$. To proceed further, we need to consider both independent identically distributed (i.i.d.) fading channels and independent non-identically distributed (i.n.d.) fading channels.

Therefore, the authors propose to investigate the throughput capacity performance of cooperative-diversity networks over fading channels. Our goal is to derive an exact closed-form analytical expression of the throughput capacity over both i.i.d. and i.n.d. fading channels. Besides, we aim to derive the tight bounds for the capacity at the regime of low signal-to-noise (SNR) and high SNR, respectively.

Appendix A

The Proof of Theorem 1

In wireless network $\boldsymbol{M}$ there exist m nodes. Dynamically, at time instants $k = 1, 2, \cdots, n$, each node i from source set $\boldsymbol{S}$ transmits a signal X_k^i to the node j in destination set $\boldsymbol{D}$ at rate R^{ij}. We assume all the messages W^{ij} being sent from node i to node j are independent and uniformly distributed over their respective ranges $\{1, 2, \cdots, 2^{nR^{ij}}\}$.

First, we give the standard definitions of a feasible information rates $\{R^{ij}\}$.

Definition 3. A $(R_{ij}, i, j \in \boldsymbol{M}; n)$ code with error probability $P_e^{(n)(ij)}$ consists of the following: [1]

• Encoders: The input symbol X_k^i at node i depends on $W^i := \{W^{ij}, j \in \boldsymbol{M}, j \neq i\}$, as well as the past values of the received symbol $\boldsymbol{Y}_{k-1}^i$ at node i, where $\boldsymbol{Y}_k^i := (Y_1^i, \cdots, Y_k^i)$. Thus, we allow a coding function $f_{i,k}$ such that for all $i \in \boldsymbol{S}, k \geq 1$, $X_k^i = f_{i,k}(\boldsymbol{Y}_{k-1}^i, W^i)$.

• Decoders: The decoder j maps the received symbols in each block $\boldsymbol{Y}_k^j := \{Y_1^j, \cdots, Y_k^j\}$ and his own transmitted information $W^j := \{W^{ji}, i \in M, i \neq j\}$, to form estimates of the messages, $W^{ij}(\boldsymbol{Y}_k^j, W^j), i = 1, 2, \cdots, m$.

• Average probability of error:

$$P_e^{(n)(ij)} = Pr\Big\{(\hat{W}^{ij}, i, j \in M) \neq (W^{ij}, i, j \in M)\Big\}. \tag{A.1}$$

Definition 4. A set of rates $\{R^{ij}\}$ is said to be *achievable* with total power constraint P_{total}, if there exists encoders and decoders satisfying $\frac{1}{n}\sum_{k=1}^{n}\sum_{i=1}^{m}(X_k^i)^2 \leq P_{total}$, such that $P_e^{(n)(ij)} \to 0$ as $n \to 0$ for all $i, j \in \boldsymbol{M}$.

After giving the standard definitions of $\{R^{ij}\}$, we introduce the following notations:

[1] The similar definitions are adopted in [16].

$$
\begin{aligned}
V_k^j &= U_k^j + Z_k^j \\
&= \sum_{i \in \boldsymbol{S}} \alpha_{ij} X_k^i + Z_k^j, \quad j \in \boldsymbol{D} && \text{(A.2)} \\
Y_k^j &= V_k^j + \sum_{i \in \boldsymbol{D}, i \neq j} \beta_{ij} X_k^i \\
&= V_k^j + \sum_{i \in \boldsymbol{D}, i \neq j} \beta_{ij} f_{i,k}(\boldsymbol{Y}_{k-1}^i, W^i), \quad j \in \boldsymbol{D} && \text{(A.3)} \\
W^{SD} &= \left\{ W^{ij}, i \in \boldsymbol{S}, j \in \boldsymbol{D} \right\}, && \text{(A.4)} \\
W^D &= \left\{ W^{ij}, i \in \boldsymbol{D}, j \neq i \right\}. && \text{(A.5)}
\end{aligned}
$$

Here, α_{ij}, β_{ij} characterize both the large-scale attenuation and the small-scale fading of the related channel, and Z_k^j with variance σ_z^2 represent the Gaussian noise introduced at destination j. Denote $V_k^D := \{V_k^j, j \in D\}$, $\boldsymbol{V}_n^D := \{V_k^D, k = 1, 2, \cdots, n\}$, and similarly for *X, Y, Z*. Since $\boldsymbol{Y}_n^D$ is a deterministic function of $(\boldsymbol{V}_n^D, W^D)$ (A.3), $W^{SD} \to \{\boldsymbol{V}_n^D, W^D\} \to \{\boldsymbol{Y}_n^D, W^D\}$ forms a Markov chain [3].

Now from *Fano's Lemma* and the property of a *Markov* chain, we have

$$
H(W^{SD} | \boldsymbol{V}_n^D, W^D) \leq H(W^{SD} | \boldsymbol{Y}_n^D, W^D) = n\varepsilon_n,
$$

where $\varepsilon_n \to 0$ as $n \to \infty$.

From the perspective of information theory, we have

$$
\begin{aligned}
nR^{SD} &= n \sum_{i\in S, j\in D} R^{ij} \\
&= \sum_{i\in S, j\in D} H(W^{ij}) \\
&= H(W^{SD}) \\
&= H(W^{SD}|W^D) \\
&= I(W^{SD}, Y_1^D, \cdots, Y_n^D|W^D) \\
&\quad + H(W^{SD}|Y_1^D, \cdots, Y_n^D, W^D) \\
&\leq I(W^{SD}, Y_1^D, \cdots, Y_n^D|W^D) + n\varepsilon_n \\
&= \sum_{k=1}^{n} I(W^{SD}, Y_k^D|Y_1^D, \cdots, Y_{k-1}^D, W^D) + n\varepsilon_n \\
&= \sum_{k=1}^{n} \big[H(Y_k^D|Y_1^D, \cdots, Y_{k-1}^D, W^D) \\
&\quad - H(Y_k^D|Y_1^D, \cdots, Y_{k-1}^D, W^D, W^{SD})\big] + n\varepsilon_n \\
&= \sum_{k=1}^{n} \big[H(Y_k^D|Y_1^D, \cdots, Y_{k-1}^D, W^D, X_k^D) \\
&\quad - H(Y_k^D|Y_1^D, \cdots, Y_{k-1}^D, W^D, W^{SD}, X_k^S, X_k^D)\big] \\
&\quad + n\varepsilon_n \\
&= \sum_{k=1}^{n} \big[H(Y_k^D|X_k^D) - H(Y_k^D|X_k^S, X_k^D)\big] + n\varepsilon_n \\
&= n \cdot \frac{1}{n} \sum_{k=1}^{n} \big[H(Y_Q^D|X_Q^D, Q=k) \\
&\quad - H(Y_Q^D|X_Q^S, X_Q^D, Q=k)\big] + n\varepsilon_n \\
&= n\big[H(Y_Q^D|X_Q^D) - H(Y_Q^D|X_Q^S, X_Q^D)\big] + n\varepsilon_n \qquad \text{(A.6)}
\end{aligned}
$$

With further transformation, we obtain

$$\begin{aligned} R^{SD} &= H(Y_k^D|X_k^D) - H(Y_k^D|X_k^S, X_k^D) + \varepsilon_n \\ &= \sum_{j\in D} \big[H(V_k^j) - H(Z_j)\big] + \varepsilon_n \\ &= \sum_{j\in D} \big[\frac{1}{2}\log \pi e(E|U_k^j|^2 + \sigma_z^2) - \frac{1}{2}\log \pi e\sigma_z^2\big] + \varepsilon_n \\ &= \sum_{j\in D} \big[\frac{1}{2}\log(1 + \frac{E|U_k^j|^2}{\sigma_z^2})\big] + \varepsilon_n \\ &= \sum_{j\in D} \big[\frac{1}{2}\log(1 + \frac{E|\sum_{i\in \boldsymbol{S}} \alpha_{ij} X_k^i|^2}{\sigma_z^2})\big] + \varepsilon_n \end{aligned} \tag{A.7}$$

From the information theory point of view, Theorem 1 defined the upper bound of information rate if any casual transmission strategy is allowed. The proof is complete.

Appendix B

Lemma 2.3.1.1

Lemma 2.3.1.1. If χ_i for $i = 1, 2, ..., n$ are independent identically Gamma-distributed $\Gamma(k_i, \lambda)$, then

$$\sum_{i=1}^{n} \chi_i \sim \Gamma\Big(\sum_{i=1}^{n} k_i, \lambda \Big). \tag{B.1}$$

Proof. The moment generating function (MGF) $M_x(t)$ associated with the fading PDF $f(x)$ is

$$M_x(t) = E[e^{tx}] = \int_0^\infty e^{tx} f(x) dx; \tag{B.2}$$

then for $Y = \sum_{i=1}^{n} X_i$, the MGF is

$$\begin{aligned} M_y(t) &= E[e^{ty}] \\ &= E[e^{t(x_1 + x_2 + ... x_n)}] \\ &= E[e^{tx_1}] E[e^{tx_2}] \cdots E[e^{tx_n}] \\ &= \prod_{i=1}^{n} M_{x_i}(t) \end{aligned}$$

In terms of the Gamma distribution $\Gamma(k_i, \theta)$, $M_x(t) = \frac{1}{(1-\theta t)^{k_i}}$; the MGF of the sum of X_i is thus

$$M_y(t) = \frac{1}{(1 - \theta t)^{\sum_{i=1}^{n} k_i}}, \tag{B.3}$$

which is the MGF of a Gamma random variable with $k' = \sum_{i=1}^{n} k_i$, $\theta' = \theta$. Therefore, $\sum_{i=1}^{N} X_i \sim \Gamma\big(\sum_{i=1}^{N} k_i, \theta \big)$. □

Appendix C

Optimal Sensor Selection Scheme under Optimal Power Allocation

In this appendix, we derive the optimal sensor selection scheme under optimal power allocation.

Note that, if $\lambda = 0$, the first KKT condition implies that $\mu_i < 0$ for all sensor i. This conclusion contradicts with the fifth KKT condition. Therefore, we must have $\lambda > 0$, which means $\sum_{i=1}^{m} a_i(\sigma_\theta^2 + \sigma_i^2) - P_{tot} = 0$.

Transforming the first KKT condition, we obtain

$$a_i = \frac{\xi_i}{\sigma_i^2 g_i}\left(\sqrt{\frac{g_i}{\lambda(\sigma_\theta^2 + \sigma_i^2) - \mu_i}} - \xi_i\right). \tag{C.1}$$

For those active voltage sensors, a_i should satisfy $a_i > 0$. Further, the third KKT condition tells us that if $a_i > 0$, then $\mu_i = 0$ holds. Hence, the proof of (3.17) is complete.

To determine λ, let us assume that the sensors are ordered such that $\eta_1 \geq \eta_2 \ldots \geq \eta_m$. Clearly, this ranking favors the voltage sensors with better channel conditions and higher observation quality.

Combining the first and second KKT conditions, we could get

$$\sqrt{\lambda} = \frac{\sum_{i=1}^{K'} \sqrt{\frac{\xi_i^2(\sigma_\theta^2+\sigma_i^2)}{g_i\sigma_i^4}}}{P_{tot} + \sum_{i=1}^{K'} \frac{\xi_i^2(\sigma_\theta^2+\sigma_i^2)}{g_i\sigma_i^2}}. \tag{C.2}$$

The active voltage sensor number K' (which has been shown to be unique [64]) can be solved if we substitute λ back to (3.17).

Appendix D

Derivation of Lemma 4.2.1

Let $U := (u_0, u_1, \cdots, u_N)$ be any admissible decision. From dynamic programming equations (4.11), since U is admissible but not necessarily optimal, we obtain

$$\begin{aligned} v_k(x_k) &\leq c_k(u_k, x_k) + v_{k+1}(x_k + u_k) \\ &\overset{\text{(a)}}{\leq} c_k(u_k, x_k) + v_{k+1}(x_{k+1}), \end{aligned}$$

where (a) follows $x_{k+1} = x_k + u_k$. Summing from 0 to N-1, we get

$$v_0(x) \leq \boldsymbol{J}_0(x; U). \tag{D.1}$$

Now consider the optimal battery charging/discharging decision $\hat{U} := (\hat{u}_0, \hat{u}_1, \cdots, \hat{u}_N)$. From the definition of $\hat{u}_k(x)$ that attains the infimum in (4.11), we have

$$\begin{aligned} v_k(\hat{x}_k) &= c_k(\hat{u}_k, x_k) + v_{k+1}(x_k + \hat{u}_k) \\ &= c_k(\hat{u}_k, x_k) + v_{k+1}(\hat{x}_{k+1}). \end{aligned}$$

Similarly, adding up for k from 0 to N-1, we reach

$$v_0(x) = \boldsymbol{J}_0(x; \hat{U}). \tag{D.2}$$

Together with (D.1) and (D.2), we conclude that the PHEV battery charging/discharging decision $\hat{U} := (\hat{u}_0, \hat{u}_1, \cdots, \hat{u}_N)$ of the dynamic programming is also optimal for $\boldsymbol{J}_0(x; U)$. The proof is thus complete.

Appendix E

Derivation of Theorem 6

First of all, let us introduce the definition of K-convex:

Definition 5. A function g: $\mathbf{R} \to \mathbf{R}$ is said to be *K-convex*, $K \geq 0$, if it satisfies the property

$$K + g(y + a) \geq g(y) + a\frac{g(y) - g(y - b)}{b}, \quad for\ all\ a \geq 0, b > 0. \tag{E.1}$$

Actually, to demonstrate the optimality of (*s, S, s', S'*) feedback policy we only need to prove

$$h_k(x) = \begin{cases} K + p_k(S), & if \quad x < s \\ p_k(x). & if \quad s \leq x \leq x_{max} \end{cases} \tag{E.2}$$

$$h'_k(x) = \begin{cases} K + q_k(S'), & if \quad x > s' \\ q_k(x). & if \quad x_{min} \leq x \leq s' \end{cases} \tag{E.3}$$

The proof of $h_k(x)$ (E.2) is similar to that of Theorem C.2.3 in [96]. Therefore, due to the space limitation, in this work we only provide the derivation of $h'_k(x)$.

Before proceedings, we need to prove the K-convexity of $h'_k(x)$. This could be done by induction. First, $v_N(x)$ is convex by definition (4.10) and thus K-convex for any $K \geq 0$ [93]. Suppose for a given $k \leq (N-1)$, $v_{k+1}(x)$ is K-convex. According to [93], restriction of any K-convex function on any convex set is K-convex. Therefore, $h'_k(x)$ is K-convex. Clearly, $v_k(x)$ is also K-convex, which completes the induction argument. Hereafter, we remove the subscript k for the general case analysis.

Now, our main focus is to prove

$$q(x) \leq q(y) + K, \quad \forall\ x, y \quad with \quad x_{min} \leq x \leq y \leq s'. \tag{E.4}$$

Clearly, the inequality (E.4) holds for $x = y$, $x = S'$, and $x = s'$, since $q(s') \leq q(S') + K \leq q(y) + K$. Therefore, we primarily examine the following two cases: (1) $x_{min} \leq y < x \leq S'$ and (2) $x_{min} \leq y < x$, $S' \leq x < s'$.

• Case 1 ($x_{min} \leq y < x \leq S'$). According to the K-convexity of $q(x)$, we have

$$K + q(y) \geq q(x) + \frac{y - x}{x - z}[q(x) - q(z)]. \tag{E.5}$$

Let $z = S'$, we could derive $q(x) < K + q(y)$ with $q(x) \geq q(S')$.

• Case 2 ($x_{min} \leq y < x$, $S' \leq x < s'$). With the definition of s', if $s' < x_{max}$ we obtain $q(s') = K + q(S')$.

Further, with the convexity of $q(x)$, it is concluded that

$$\begin{aligned} K + q(S') &\geq q(x) + \frac{S' - x}{x - s'}[q(x) - q(s')] \\ &\geq q(x) + \frac{S' - x}{x - s'}[q(x) - q(S') - K]. \end{aligned} \tag{E.6}$$

Transforming (E.6) leads to

$$\left(1 + \frac{S' - x}{x - s'}\right)[K + q(S')] \geq \left(1 + \frac{S' - x}{x - s'}\right)q(x). \tag{E.7}$$

Dividing both side of (E.7) by $\left(1 + \frac{S'-x}{x-s'}\right)$, we reach

$$q(x) \leq K + q(S') \leq K + q(y). \tag{E.8}$$

We finished the proof of (E.3). Together with function *h(x)* (E.2), we could readily prove the optimality of the (*s, S, s', S'*) feedback policy. We complete the proof.

References

[1] O. Dousse, P. Thiran and M. Hasler, "Connectivity in ad-hoc and hybrid networks", *Infocom 2002*, vol.2, pp. 1079-1088, Nov. 2002.

[2] P. Gupta and P.R. Kumar, "The capacity of wireless networks", *IEEE Transactions on Information Theory*, vol.46, no.2, pp. 388-404, Mar. 2000.

[3] L. Xie and P.R. Kumar, "A network information theory for wireless communication: scaling laws and optimal operation", *IEEE Transactions on Information Theory*, vol. 50, no. 5, pp. 748-767, May 2004.

[4] M. Franceschetti, O. Dousse, D. Tse and P. Thiran , "Closing the gap in the capacity of wireless networks via percolation theory", *IEEE Transactions on Information Theory*, vol. 53, no. 3, pp. 1009-1018, Mar. 2007.

[5] M. Grossglauser and D. Tse, "Mobility increases the capacity of ad-hoc wireless networks", *IEEE/ACM Transactions on Networking*, vol.10, no.4, pp. 477-486, Aug. 2002.

[6] B. Liu, Z. Liu, and D. Towsley, "On the capacity of hybrid wireless networks", *Infocom 2003*, vol. 2, pp. 1543-1552, Apr. 2003.

[7] B. Liu, P. Thiran and D. Towsley, "Capacity of wireless ad hoc network with infrastructure", *Proceeding of ACM MobiHoc*, Montreal, Canada, Sep. 2007.

[8] U.C. Kozat and L. Tassiulas, "Throughput capacity of random ad hoc Networks with infrastructure support", *ACM Mobicom 2003*, pp. 55-65, 2003.

[9] A. Agarwal and P. Kumar, "Capacity bounds for ad hoc and hybrid wireless networks", *ACM SIGCOMM Computer Communication Review*, vol. 34, no. 3, pp. 71-81, Jul. 2004.

[10] A. Zemlianov and G. Veciana, "Capacity of ad hoc wireless Networks with infrastructure support", *IEEE Journal on Selected Areas in Communications*, vol. 23, no. 3, pp. 657-667, Mar. 2005.

[11] D. Kirachaiwanich and Q. Liang, "Capacity of wireless hybrid networks with successive interference cancellation", *Globecom 2010*, pp. 1-5, Dec. 2010.

[12] P. Zhou, X. Wang and R. Rao, "Asymptotic capacity of infrastructure wireless mesh networks", *IEEE Transactions on Mobile Computing*, vol. 7, no. 8, pp. 1011-1024, Aug. 2008.

[13] G. Zhang, Y. Xu, X. Wang and M. Guizani, "Capacity of hybrid wireless networks with directional antenna and delay constraint", *IEEE Transactions on Communications*, vol. 58, no. 7, pp. 2097-2106, Jul. 2010.

[14] L.K. Law, K. Pelechrinis, S.V. Krishnamurthy, and M. Faloutsos, "Downlink capacity of hybrid cellular ad hoc networks", *IEEE/ACM Transactions on Networking*, vol.18, no.1, pp. 243-256, Feb. 2010.

[15] L. Kazovsky, S. Wong , T. Ayhan, K.M. Albeyoglu, M.R.N. Ribeiro and A. Shastri, "Hybrid optical-wireless access networks", *Proceedings of the IEEE*, vol.100, no.5, pp. 1197-1225, May 2012.

[16] F. Xue, L. Xie and P.R. Kumar, "The transport capacity of wireless networks over fading channels", *IEEE Transactions on Information Theory*, vol. 51, no. 3, pp. 834-847, Mar. 2005.

[17] G. Farhadi and N. C. Beaulieu, "On the ergodic capacity of wireless relaying systems over Rayleigh fading channels", *IEEE Transactions on Wireless Communications*, vol. 7, no. 11, pp. 4462-4467, Nov. 2008.

[18] M. K. Simon and M. Alouini, *Digital Communication over Fading Channels, 2nd Edition*, Wiley, 2004.

[19] T. Cover and J. Thomas, *Elements of Information Theory, 2nd Edition*, Wiley, 2006.

[20] D. Tse and P. Viswanath, *Fundamentals of Wireless Communication*, Cambridge University Press, 2005.

[21] A. Ozgur, O. Leveque and D. Tse, "Hierarchical cooperation achieves linear capacity scaling in ad hoc networks", *Infocom 2007*, pp. 382-390, May 2007.

[22] J. Du E. Kranakis and A. Nayak, "Cooperative neighbor discovery protocol for a wireless network using two antenna patterns," *ICDCSW 2012*, pp. 178-186, Macau, Jun. 2012.

[23] H. Sadjadpour, Z. Wang and J. Garcia-Luna-Aceves, "The capacity of wireless ad hoc networks with multi-packet reception", *IEEE Transactions on Communications*, vol. 58, no. 2, pp. 600-610, Feb. 2010.

[24] S. Weber, X. Yang, J. G. Andrews and G. Veciana, "Transmission capacity of wireless ad hoc networks with successive interference cancellation", *IEEE Transactions on Information Theory*, vol. 53, no. 8, pp. 2799-2814, Aug. 2007.

[25] T. Le and Y. Liu, "On the capacity of hybrid wireless networks with opportunistic routing", *EURASIP Journal onWireless Communications and Networking*, vol. 2010, no. 3, Apr. 2010 .

[26] J. Blomer and N. Jindal, "Transmission capacity of wireless ad hoc networks: successive interference cancellation vs. joint detection", *IEEE International Conference on Communications 2009*, pp. 1-5, Dresden, Germany, Jun. 2009.

[27] P. Sharma, "Selection of diversity and modulation parameters for Nakagami fading channels to jointly satisfy outage and bit error requirements", *IEEE Transactions on Wireless Communications*, vol. 5, no. 6, pp. 1279-1283, Jun. 2006.

[28] X. Dong, X, Li and D. Wu, "Analysis of packet error probability in delay constrained communication over fading channels", *IEEE CCNC 2009*, pp. 1-5, Las Vegas, NV, Jan. 2009.

[29] J. G. Proaksi and M. Salehi, *Digtial Communication, 5th edition*, McGraw-Hill, 2008.

[30] T. S. Rappaport, *Wireless Communications: Principles and Practice, 2nd Edition*, Prentice Hall, 2002.

[31] S. Bu, F. Yu, Y. Cai and X. Liu, "When the smart grid meets energy-efficient communications: green wireless cellular networks powered by the smart grid", *IEEE Transactions on Wireless Communications*, vol. 11, no. 8, pp. 3014-3024, Aug. 2012.

[32] M. Qiu, W. Gao, M. Chen, J. Niu and L. Zhang, "Energy efficient security algorithm for power grid wide are monitoring System", *IEEE Transactions on Smart Grid*, vol. 2, no. 4, pp. 715-723, Dec. 2011.

[33] F. Bouhafs, M. Mackay, and M. Merabti, "Links to the future: communication requirements and challenges in the smart grid", *IEEE Power and Energy Magazine*, vol. 10, no. 9, pp. 24-32, Jan. 2012.

[34] H. Farag, E. Saadany, and R. Seethapathy, "A two ways communication-based distributed control for voltage regulation in smart distribution feeders", *IEEE Transactions on Smart Grid*, vol. 3, no. 1, pp. 271-481, Mar. 2012.

[35] F. Viawan and D. Karlsson, "Voltage and reactive power control in systems with synchronous machine-based distributed generation", *IEEE Transactions on Power Delivery*, vol. 23, no. 2, pp. 1079-1087, Apr. 2008.

[36] R. Mao and H. Li, "An efficient multiple access scheme for voltage control in smart grid using WiMAX", *ICC 2012*, Ottawa, ON, pp. 3367-3371, Jun. 2012.

[37] V. Gupta, "On an estimation oriented routing protocol", *American Control Conference (ACC) 2010*,Baltimore, MD, pp. 580-585, Jun. 2010.

[38] H. Li, L. Lai and H. Poor, "Multicast routing for decentralized control of cyber physical systems with an application in smart grid", *IEEE Journal on Selected Areas in Communications*, vol. 30, no. 6, pp. 1097-1107, Jul. 2012.

[39] R. Mao and H. Li, "Nobody but you: MAC scheduling for voltage regulation in smart grid", *IEEE SmartGridComm 2012*.

[40] H. Li, "Virtual queue based distributed data traffic scheduling for cyber physical systems with application in smart grid", *ICDCSW 2012*, Macau, pp. 309-314, Jun. 2012.

[41] H. Li, F. Li, Y. Xu, D. Rizy and J. Kueck, "Adaptive voltage control with distributed energy resources: algorithm, theoretical analysis, simulation, and field test verification", *IEEE Transactions on Power Systems*, vol. 25, no. 3, pp. 1638-1647, Aug. 2010.

[42] X. Wang and P. Yi, "Security framework for wireless communications in smart distribution grid", *IEEE Transactions on Smart Grid*, vol. 2, no. 4, pp. 809-818, Dec. 2011.

[43] A. Zaballos, A. Vallejo, and J. Selga, "Heterogeneous communication architecture for the smart grid", *IEEE Network*, vol. 25, no. 5, pp. 30-37, Sep. 2011.

[44] K. Hongrae and T.M. Jahns, "Current control for AC motor drives using a single DC-link current sensor and measurement voltage vectors", *IEEE Transactions on Industry Applications*, vol. 42, no. 6, pp. 1539-1547, Nov. 2006.

[45] H. Rowaihy, S. Eswaran, M. Johnson, D. Verma, A. Bar-Noy, T. Brown and T.L. Poota, "A survey of sensor selection schemes in wireless sensor networks".

[46] K. Kincaid and S. Padula, "D-optimal designs for sensor and actuator locations", *Comp. and Oper. Res.*, vol. 29, no. 6, pp. 701-713, 2002.

[47] T. Wimalajeewa,and S.K. Jayaweera, "Distributed node selection for sequential estimation over noisy communication channels", *IEEE Transactions on Wireless Communications*, vol. 9, no. 7, pp. 2290-2301, Jul. 2010.

[48] H. Wang, K. Yao, G. Pottie, and D. Estrin, "Entropy-based sensor selection heuristic for target localization", *Proc. 3rd Int. Symp. Inf. Processing in Sensor Networks*, Berkeley, CA, pp. 36-45, 2004.

[49] F. Bian, D. Kempe and R. Govindan, "Utility-based sensor selection", *in Proceedings of the IEEE Conference on Information Processing in Sensor Network (IPSN 2006)*, Apr. 2006.

[50] S. Joshi and S. Boyd, "Sensor selection via convex optimization", *IEEE Transactions on Signal Processing*, vol. 57, no. 2, pp. 451-462, Feb. 2009.

[51] J. Ai and A. Abouzeid, "Coverage by directional sensors in randomly deployed wireless sensor networks", *Journal of Combinatorial Optimization*, Feb. 2006.

[52] K. Shih, Y. Chen, C. CHiang and B. Liu, "A distributed active sensor selection scheme for wireless sensor networks", *in Proceedings of the IEEE Symposium on Computers and Communications*, Jun. 2006.

[53] M. Gastpar, and M. Vetterli, "Source-channel communication in sensor networks", *Springer Lecture Notes in Computer Science*, vol. 2634, pp. 162-177, Apr. 2003.

[54] M. Gastpar, "Uncoded transmission is exactly optimal for a simple gaussian "sensor" network", *IEEE Transactions on Information Theory*, vol. 54, no. 11, pp. 5247-5251, Nov. 2008.

[55] J. Xiao, S. Cui, Z. Luo, and A. Goldsmith, "Linear coherent decentralized estimation", *IEEE Transactions on Signal Processing*, vol. 56, no. 2, pp. 757-770, Feb. 2008.

[56] S. Cui, J. Xiao, A. Goldsmith, Z. Luo, and H. Poor, "Estimation diversity and energy efficiency in distributed sensing", *IEEE Transactions on Signal Processing*, vol. 55, no. 9, pp. 4683-4695, Sept. 2007.

[57] A. Leong and S. Dey, "On scaling laws of diversity schemes in decentralized estimation", *IEEE Transactions on Information Theory*, vol. 57, no. 7, pp. 4740-4759, Jul. 2011.

[58] J. Matamoros and C. Haro, "Opportunistic power allocation and sensor selection schemes for wireless sensor networks", *IEEE Transactions on Wireless Communications*, vol. 9, no. 2, pp. 534-539, Feb. 2010.

[59] U. Rashid, H. Tuan, P. Apkarian and H. Kha, "Globally optimized power allocation in multiple sensor fusion for linear and nonlinear networks", *IEEE Transactions on Signal Processing*, vol. 60, no. 2, pp. 903-915, Feb. 2012.

[60] S. M. Kay, *Fundermentals of Statistical Signal Processing: Estimation Theory,* Cambridge University Press, 1993.

[61] S. Boyd and L. Vandenberghe, *Convex Optimization*, Cambridge University Press, 2003.

[62] J. G. Proaksi, *Digtial Communication, 4th ed*, New York: McGrawHill, 2001.

[63] Andrea Goldsmith, *Wireless Communications*, Cambridge University Press, 2005.

[64] J.J. Xiao, S. Cui, Z.Q. Luo and A.J. Goldsmith, "Power scheduling of universal decentralized estimation in sensor networks," *IEEE Transactions on Signal Processing*, vol.54, no.2, pp. 413-422, Feb. 2006.

[65] Q. Chen, F. Sun, and J. Zhu, *Modern Electric Vehicle Technology*. Beijing, China: Beijing Institute of Technology Press, 2004.

[66] E. Sortomme and M.A. El-Sharkawi, "Optimal charging strategies for unidirectional vehicle-to-grid", *IEEE Transactions on Smart Grid*, vol. 2, no. 1, pp. 131-138, Mar. 2011

[67] Z. J. Ma, D. Callaway, and I. Hiskens, "Decentralized charging control for large populations of plug-in electric vehicles: Application of the Nash certainty equivalence principlee," *in Proc. IEEE Int. Conf. Control Appl.*, Sep. 2010, pp. 191-195.

[68] C. Roe, F. Evangelos, J. Meisel, S. Meliopoulos and T.Overbye, "Power system level impacts of PHEVs," *Proc. 42nd Hawaii Int. Conf. Syst. Sci.*, pp. 1-10, 2009.

[69] K. Clement, E. Haesen and J. Driesen, "Coordinated charging of multiple plug-in hybrid electric vehicles in residential distribution grids," *Power Systems Conference and Exposition*, pp. 1-7, Mar. 2009.

[70] W. Kempton and J. Tomic, "Vehicle-to-grid power fundamentals: Calculating capacity and net revenue," *J. Power Sources*, vol. 144, no. 1, pp. 268-279, Jun. 2005.

[71] W. Kempton and J. Tomic, "Vehicle-to-grid power implementation: From stabilizing the grid to supporting large-scale renewable energy," *J. Power Sources*, vol. 144, no. 1, pp. 280-294, Jun. 1, 2005.

[72] S. D. Jenkins, J. R. Rossmaier, andM. Ferdowsi, Utilization and effect of plug-in hybrid electric vehicles in the United States power grid, *in Proc. IEEE Veh. Power Propulsion Conf.*, Harbin, China, pp. 1-5, Sep. 2008,

[73] J. Tomic and W. Kempton, "Using fleets of electric-drive vehicles for grid support," *J. Power Sources*, vol. 168, no. 2, pp. 459-468, Jun. 2007.

[74] T. Markel, M. Kuss, and P. Denholm, "Communication and control of electric drive vehicles supporting renewables," *in Proc. 2009 IEEE Veh. Power Propulsion Conf.*, pp. 27-34, Sept. 2009.

[75] H. Liang, B. Choi, W. Zhuang and X. Shen, "Towards optimal energy store-carry-and-deliver for PHEVs via V2G system," *Infocom 2012*, pp. 1674-1682, Mar. 2012.

[76] P. Richardson, D. Flynn and A. Keane, "Local versus centralized charging strategies for electric vehicles in low voltage distribution systems," *IEEE Transactions on Smart Grid*, vol. 3, no. 2, pp. 1020-1028, Jun. 2012.

[77] L. Gan, U. Topcu and S. Low, "Optimal decentralized protocol for electric vehicle charging," *2011 50th IEEE Conference on Decision and Control and European Control Conference*, pp. 5798-5804, Dec. 2011.

[78] P.A. Cassani and S.S Williamson, "Feasibility analysis of a novel cell equalizer topology for plug-in hybrid electric vehicle energy-storage systems," *IEEE Transactions on Vehicular Technology*, vol. 58, no. 8, pp. 3938-3946, Oct. 2009.

[79] K. Qian, C. Zhou, M. Allan, and Y. Yuan, "Modeling of load demand due to EV battery charging in distribution systems," *IEEE Trans. Power Syst.*, pp. 1-9, Aug. 2010.

[80] K. Clement-Nyns, E. Haesen, and J. Driesen, "The impact of charging plug-in hybrid electric vehicles on a residential distribution grid," *IEEE Trans. Power Syst.*, vol. 25, no. 1, pp. 371-380, Feb. 2010.

[81] P. Samadi, A. Mohsenian-Rad, R. Schober, V. Wong, and J. Jatskevich, "Optimal real-time pricing algorithm based on utility maximization for smart grid," *in Proc. 1st IEEE SMARTGRIDCOMM,* Gaithersburg, Maryland, USA, pp. 415-420, Oct. 2010,

[82] N. Gatsis and G. B. Giannakis, "Residential load control: Distributed scheduling and convergence with lost ami messages," *IEEE Trans. Smart Grid*, vol. 3, no. 2, pp. 770-786, 2012.

[83] Z. Ma, D. Callaway and I. Hiskens, "Decentralized charging control of large populations of plug-in electric vehicles," *IEEE Trans. on Control Systems Technology*, vol. 21, no. 1, pp. 67-78, Jan. 2013.

[84] A. Mohsenian-Rad, V. Wong, J. Jatskevich, R. Schober, and A. Leon-Garcia, "Autonomous demand-side management based on game-theoretic energy consumption scheduling for the future smart grid," *IEEE Trans. Smart Grid*, vol. 1, no. 3, pp. 320-331, 2010.

[85] K. Turitsyn, N. Sinitsyn, S. Backhaus, and M. Chertkov, "Robust broadcast-communication control of electric vehicle charging," *in Proc. 1st IEEE SMART-GRIDCOMM*, pp. 203-207, Gaithersburg, Maryland, USA, 2010.

[86] M. Erol-Kantarci, J. H. Sarker, and H. T. Mouftah, Analysis of plug in hybrid electrical vehicle admission control in the smart grid, *in Proc. IEEE CAMAD*, pp. 72C76, Kyoto, Japan, Jun. 2011.

[87] K. Mets, R. D'hulst and C. Develder, "Comparison of intelligent charging algorithms for electric vehicles to reduce peak load and demand variability in a distribution grid," *Journal of Communications and Networks*, vol. 14, no. 6, pp. 672-681, Dec. 2012.

[88] M. Anderman, "Brief assessment of improvements in EV battery technology since the BTAP June 2000 report", Rep. No. 02-611, California Air Resources Board, Sacramento, CA, 2003.

[89] D. Linden and T. B. Reddy, *Handbook of Batteries*, McGraw Hill Handbooks, 2002.

[90] R. Urgaonkar, B. Urgaonkar, M. J. Neely, and A. Sivasubramaniam, "Optimal power cost management using stored energy in data centers", *Proc. ACM SIGMETRICS*, Jun. 2011.

[91] S. B. Peterson, J. F. Whitacre, and J. Apt, "The economics of using plug-in hybrid electric vehicle battery packs for grid storage", *J. Power Sources*, vol. 195, no. 8, pp. 2377-2384, Apr. 2010.

[92] Orange & Rockland Co. http://www.oru.com/index.html.

[93] D. P. Bertsekas, *Dynamic Programming and Optimal Control*, vols. 1 and 2. Athena Scientific, 2007.

[94] Society of Automotive Engineers, *SAE Surface Vehicle Recommended Practice J1772, SAE Electric Vehicle Conductive Charge Coupler.*

[95] South California Edison Company website, available at http://www.sce.com/005_regul_info/eca/DOMSM12.DLP.

[96] D. Beyer, F. Cheng, S. Sethi, and M. Taksar, *Markovian Demand Inventory Models,* New York: Springer, 2010.

[97] J. N. Laneman, D. N. C. Tse, and G. W. Wornell, "Cooperative diversity in wireless networks: Efficient protocols and outage behavior", *IEEE Transactions on Information Theory*, vol.50, no.12, pp. 3062-3080, Dec. 2004.

[98] J. N. Laneman and G. W. Wornell, "Distributed space-time-coded protocols for exploiting cooperative diversity in wireless networks", *IEEE Transactions on Information Theory*, vol.49, no.10, pp. 2415-2425, Oct. 2003.

[99] L. Fan, X. Lei and W. Li, "Exact closed-form expression for ergodic capacity of amplify-and-forward relaying in channel-noise-assisted cooperative networks with relay selection", *IEEE Communications Letters*, vol.15, no.3, pp. 332-333, Mar. 2011.

[100] A. Hst-Madsen, and J. Zhang, "Capacity bounds and power allocation for wireless relay channels", *IEEE Transactions on Information Theory*, vol. 51, no. 6, pp. 2020-2040, Jun. 2005.

[101] C. Chen and L. Wang, "A unified capacity analysis for wireless systems with joint multiuser scheduling and antenna diversity in Nakagami fading channels", *IEEE Transactions on Communications*, vol. 54, no. 3, pp. 469-478, Mar. 2006.

[102] S. Chen, W. B. Wang and X. Zhang, "Ergodic and outage capacity analysis of cooperative diversity systems under Rayleigh fading channels", *ICC workshop 2009*, pp. 1-5, June 2009.

[103] G. Farhadi and N. C. Beaulieu, "Ergodic capacity analysis of wireless relaying systems in Rayleigh fading", *ICC 2008*, pp. 3730-3735, May 2008.

[104] K. Letaief and W. Zhang, "Cooperative communications for cognitive radio network", *in Proc. of the IEEE*, vol. 97, no. 5, pp. 878-893, May 2009.

[105] T. Fujii and Y. Suzuki, "Ad-hoc cognitive radio-development to frequency sharing system by using multi-hop network", *in Proc. IEEE DySPAN 2005*, pp. 589-592, Maryland, MD, Nov. 2005.

[106] K. Lee and A. Yener, "Outage performance of cognitive wireless relay networks," *IEEE GLOBECOM 2006*, pp. 1-5, San Francisco, CA, Nov. 2006.

[107] K. Hamdi and K. B. Letaief, "Cooperative communications for cognitive radio networks", *in Proc. PGNet 2007*, Liverpool, UK, Jun. 2007.

[108] F. Baccelli, M. Klein, M. Lebourges, and S. Zuyev, "Stochastic geometry and architecture of communication networks," *J. Telecommun. Syst.*, vol. 7, no. 1, pp. 209227, 1997.

[109] J. G. Andrews, F. Baccelli and R. Ganti, "A tractable approach to coverage and rate in cellular networks", *IEEE Transactions on Communications*, vol. 59, no. 11, pp. 3122-3134, Nov. 2011.

[110] X. Wang and Q. Liang, "On the Throughput Capacity and Performance Analysis of Hybrid Wireless Networks over Fading Channels," *IEEE Transactions on Wireless Communications*, vol. 12, no. 6, pp. 2930-2940, Jun. 2013.

[111] X. Wang and Q. Liang, "On the outage throughput capacity of hybrid wireless networks over fading channels," *Globecom 2012*, pp. 2173-2178, Anaheim, CA, Dec. 2012.

[112] X. Wang, L. Zhang, A. Deokar and Q. Liang, "Enhanced Security and Reliability with MIMO Communications for Smart Grid", *Security and Communication Networks*, Wiley, Sec. 585, Jul. 2012.

[113] X. Wang, Q. Liang, J. Mu, W. Wang and B. Zhang, "Physical Layer Security in Wireless Smart Grid", *Security and Communication Networks*, Wiley, Sec. 751, Mar. 2013.

[114] X. Wang and Q. Liang, "On the Ergodic Capacity of Cooperative-Diversity Networks with Decode-and-Forward Relaying over Nakagami-m Fading Channels", *IEEE GLOBECOM 2013*, Atalanta, GA.

[115] X. Wang and Q. Liang, "Joint Power and Spectrum Allocation for Relay Stations in Mobile Relay Networks", *International Conference on Communications Signal Processing and Systems 2013*, Tianjin, China.

[116] X. Wang and Q. Liang, "Scaling Laws for Hybrid Wireless Networks over Fading Channels: Outage Throughput Capacity and Performance Analysis", *IEEE ICC 2013*, pp. 5573-5577, Budapest, Hungary.

[117] X. Wang and Q. Liang, "On the Ergodic Throughput Capacity of Hybrid Wireless Networks over Fast Fading Channels", *IEEE ICC 2013*, pp. 3333-3337, Budapest, Hungary.

[118] X. Wang and Q. Liang, "Energy Management for Plug-in Hybrid Electric Vehicles via Vehicle-to-Grid", *IEEE ICC 2013*, pp. 4197-4201, Budapest, Hungary.

[119] X. Wang and Q. Liang, "Throughput Performance Analysis for Hybrid Wireless Networks over Fading Channels", *ICCCN 2013*, Nassau, Bahamas.

[120] X. Wang and Q. Liang, "Sensor Selection Schemes in Smart Grid", *IEEE ISGT 2012*.

[121] X. Wang and Q. Liang, "Stabilizing the Power Supply in Microgrid Using Sensor Selection", *IEEE GLOBECOM 2012*, pp. 3513-3518, Anaheim, CA.

[122] X. Wang and Q. Liang, "Bidirectional Energy Management for Plug-in Hybrid Electric Vehicles via Vehicle-to-Grid", *International Conference on Communications Signal Processing and Systems 2012*, Beijing, China.

[123] Z. Li, X. Wang and Q. Liang, " Chapter 4: Physical Layer Communications in Wireless Sensor Networks", *The Art of Wireless Sensor Networks*, Springer, Jan. 2014.

Biographical Statement

Xin Wang is currently working towards the Ph.D. degree in Electrical Engineering with the Department of Electrical Engineering, University of Texas, Arlington. He received the B.S. degree from Shanghai Maritime University, Shanghai, China, in 2007 and M.S. degree from Tongji University, Shanghai, China, in 2010, both in Electrical Engineering. His research interests include wireless communications, hybrid wireless networks, wireless sensor networks and smart grid.